Spring 2013

Structural and magnetic properties of Ni and Cr substituted $La_{0.7}Sr_{0.3}MnO_3$

Thomas Franklin Creel Jr.

Department: Physics

STRUCTURAL AND MAGNETIC PROPERTIES

OF Ni AND Cr SUBSTITUTED

$La_{0.7}Sr_{0.3}MnO_3$

by

THOMAS FRANKLIN CREEL JR.

A DISSERTATION

Presented to the Faculty of the Graduate School of the

MISSOURI UNIVERSITY OF SCIENCE & TECHNOLOGY

In Partial Fulfillment of the Requirements for the Degree

DOCTOR OF PHILOSOPHY

in

PHYSICS

2013

Approved by:

Dr. William J. James, Co-Advisor
Dr. Oran A. Pringle, Co-Advisor
Dr. William B. Yelon
Dr. Paul E. Parris
Dr. Thomas Vojta

PUBLICATION DISSERTATION OPTION

Section 2, pages 30-42, section 3, pages 43-53, section 4, pages 54-79, and section 5 pages 80-102 of this dissertation are published and submitted papers prepared in the style utilized by the *Materials Research Society Meetings* and *Journal of Applied Physics*.

ABSTRACT

The $La_{1-x}Sr_xMn_{1-y}B_yO_3$ perovskite systems where *B* represents a 3d transition metal such as Cr, Fe, Co, Ni, Cu, and Zn, are of significant interest due to their large magnetoresistance, and electronic transport properties that change significantly, depending on values of x and which transition metal used. Their applications in technology include cathodes for solid oxide fuel cells, resistance random access memory and catalysis. At certain doping concentrations on the B-site, metal-to-semiconductor or metal-to-insulator transitions coupled with colossal magnetoresistance occur, decreasing the resistivity (up to six orders of magnitude) upon the application of an external magnetic field. The Curie and Neel transition temperatures, T_C and T_N respectively, can be modified depending on the amount of transition metal substitution. In the parent system, $La_{1-x}Sr_xMn^{3+}_{1-x}Mn^{4+}_xO_3$, at x=0.4, the maximum transition temperature T_C^{Max} is reached in the La-based manganites.

To better understand the structural and magnetic properties of the 3d transition metal substituted perovskite $La_{0.7}Sr_{0.3}Mn^{3+}_{0.7-x}Mn^{4+}_{0.3}B^{3+}_xO_3$, we studied the effects of replacing B with Cr and Ni atoms using x-ray and neutron diffraction and magnetic measurements. Of these two 3d transition metals, Cr has the least occupied outer valence shells, (Ar) $3d^54s^1$ and has the same t_{2g} electronic configuration as Mn^{4+}, while Ni has the most filled outer valence shells, (Ar) $3d^84s^2$. The configurations of these outer valence electrons play a substantial role in the resultant magnetic interactions as witnessed by the unexpected magnetic ordering differences observed in the Cr and Ni-substituted systems. An extensive literature search indicated no previous neutron diffraction studies had been carried out for these two systems

ACKNOWLEDGMENTS

I would like to express my deep gratitude and thanks to Dr. William J. James, Dr. William B. Yelon, and Dr. Oran A. Pringle, for all their support and encouragement over the last years. It is only through their combined thorough understanding of Solid State Physics, Chemical Physics, neutron diffraction and material science, that I have been able to obtain this degree. I express a special thank you to Dr. William B. Yelon who has provided invaluable support in my understanding neutron diffraction and assistance in obtaining neutron data and magnetic measurements in support of my research. His guidance and contributions to my understanding of neutron diffraction has made a profound impact on me.

I give special thanks to the Director of the Materials Research Center (MRC), Dr. Matt O'Keefe for use of the center to prepare material samples; Dr. S.K. Malik and Professor Sylvio Quesado of the Departamento de Física Teórica Experimental, Brazil for providing magnetic measurements; Dr. Jinbo Yang who provided me with a greater understanding of the fabrication of perovskites; Mr. Thomas W. Heitmann and Mr. Mehmet Kahveci for all their support in making the neutron measurements; Mr. Eric Bohannan and Mr. Brian J. Porter for their support in making x-ray and x-ray spectroscopy measurements; and Mr. Ronald E. Haas for his mechanical support in fabricating equipment to press and grind the materials I am reporting on.

Finally, I sincerely give thanks to my wife and son for their support and patience during these past years that I have spent working on this research. Particularly, I express my utmost thanks to my wife, Martha Creel, for her patience and unconditional love and support throughout the years.

TABLE OF CONTENTS

Page

LIST OF ILLUSTRATIONS

Page

LIST OF TABLES

Page

1. INTRODUCTION AND BACKGROUND

1.1 SHORT HISTORY OF PEROVSKITES

Gustav Rose discovered $CaTiO_3$ in the Ural Mountains in 1839 and named it Perovskite after the eminent Russian mineralogist, Count Lev Alexevich Von Perovski. Over the years, the term perovskite has now become associated with an atomic structure designated as ABX_3 with A and B representing cations and X as anions. In naturally occurring perovskites, ABX_3 is referred to as ABO_3 where O represents an oxygen atom.

Manganese-based compounds of the $AMnO_3$ structure are generally referred to as manganites and ideally crystallize in the cubic perovskite structure. The broad features of these mixed-valence manganese-based perovskites were described for polycrystalline samples of $La_{1-x}Ca_xMnO_3$ by Jonker and Van Santen [1], Van Santen and Jonker [2] and Jonker [3] in the early 1950's where they found T_C to be a maximum ~370K in $La_{0.7}Sr_{0.3}MnO_3$. In 1951, Zener, [4] attributed the mechanism for observed conductivity to an e_g electron hopping between Mn^{3+} and Mn^{4+} (Mn^{3+}-O-Mn^{4+}), and coined it "double exchange." In 1953 Wollan and Koehler [5] performed the first extensive neutron diffraction study on $La_{1-x}Ca_xMnO_3$ where they found coexistence of ferromagnetic and antiferromagnetic couplings, evidence of ionic ordering, and Mn^{3+}-O-Mn^{3+} interactions to be anisotropic, being ferromagnetic in the (001) planes and antiferromagnetic along the c-axis. In 1954 Volger [6] was the first to describe magnetoresistance and other transport properties where he showed that the magnetoresistance of $La_{0.8}Sr_{0.2}MnO_3$ is negative with a peak near the Curie temperature. More detailed theoretical studies were performed by Anderson and Hasegawa [7] and de Gennes [8]. In 1960 De Gennes [8] worked to

refine the theory of doubleexchange in canted magnetic perovskites. In 1961, Goodenough, Wold, Arnott and Menyuk [9] studied $La(Mn_{1-x}\text{-}M_x)O_{3+\Delta}$ (M= Ni, Co and Ga), and characterized the magnetic couplings and ordering between the $Mn^{3+/4+}$ and Ni, Co and Ga. They presented rules for 180˚ superexchange interactions and found ferromagnetic and antiferromagnetic Mn^{3+}-O-Mn^{3+} interactions and evidence of ionic ordering. In 1969 and 1970, Searle and Wang [10], Morrish et al. [11] and Leung et al. [12] studied single crystals of $La_{1-x}Pb_xMnO_3$ with $0.2 < x < 0.44$. They found metallic conductivity below the Curie point (T_C) and a large negative magnetoresistance of about 20% at 1T in the vicinity of T_C. Searle and Wang [10] determined the $MR(\%) = \frac{\Delta R}{R(0)} = \frac{\rho_0 - \rho_h}{\rho_0} x100$ where ρ_0 and ρ_h are the resistivities in the absence and presence of a magnetic field respectively. Magnetization values suggested that a fully spin-polarized d-band is involved in the ferromagnetic ordering process. In 1970, Goodenough and Longho [13] published a significant compilation of data for compounds with the perovskite-structure in a Landoldt-Börnstein volume, and in 1972, Kubo and Ohata [14] provided a quantum mechanical interpretation of the DE mechanism. Interest in the perovskites waned until the mid-1990's and the discovery of colossal magnetoresistance, magnetoresistance as large as 127,000% near 77K, by Jin et al. in 1994 [15]. In 1995, Millis et al. [16] provided theoretical evidence that the double exchange model could not fully explain the MR behavior and proposed Jahn-Teller phonons and polarons.

In summary, manganite ground states are primarily determined by five contributions: (1) the kinetic energy of the e_g-electrons, (2) the Hund coupling energy between the e_g-electron spin and the localized t_{2g}electron spins, (3) the antiferromagnetic coupling between the nearest-neighbor t_{2g}-electron spins, (4) the electron-phonon

coupling between the e_g-electron spin and the local Jahn-Teller distortion, and (5) the Coulomb interaction among the e_g-electrons.

1.2 MANGANITE PEROVSKITE PROPERTIES

Almost all the degrees of freedom known in solid state physics such as itinerant charges, localized spins, electronic orbitals and lattice vibrations are at work in these perovskite systems. In a sense, manganites are ideal compounds for magnetic sensor devices, since the two possible primary ground states are metal and insulating. In general, the magnetoresistance effects peak at the carrier density separating the metallic phase from the insulating phase. These manganites show insulating states which can be paramagnetic, ferromagnetic, as well as antiferromagnetic. Of particular interest in these manganites is that the transition from ferromagnetism to paramagnetism is accompanied by a significant increase in conductivity. Electronic phases in these perovskites include ferromagnetic, antiferromagnetic, antiferromagnetic-layered, ferromagnetic-layered, superconducting, semi-conducting, insulating, paramagnetic, ferrimagnetic, orbital-ordered and charge-ordered, depending upon transition metal oxide dopant, values of x, y, and temperature. In fact, typically the most relevant energy scale in these manganites is the temperature at which the magnetic ordering is observed.

Substitution of divalent cations for trivalent cations on the A-site predominately alters the number of electrons in the 3d band (Mn^{3+} versus Mn^{4+}) whereas substituting various 3d transition elements for Mn^{3+} on the B-site predominately alters the interatomic distances and bond angles. For instance, the electrical conductivity of $LaMnO_3$ can be increased by substituting Sr^{2+} for La^{3+}, creating Mn^{4+} and a hole in the e_g

($3d_{x^2-y^2}, 3d_{3z^2-r^2}$) band, promoting itinerant electrons that enable conductivity. It is well known that the magnetic properties of these mixed-valence manganites are strongly dependent on the Mn^{4+} content. When the A-site is occupied by a trivalent atom such as La^{3+}, the Mn is typically in the Mn^{3+} state, as in $LaMnO_3$. However, ionic composition depends on the firing temperature and preparation process. For instance Wollan and Koehler [5] found 2% to 35% Mn^{4+} was found in $LaMnO_3$ when fired in nitrogen at 1400˚C and oxygen at 1100˚C respectively. These oxides become ferromagnetic at a critical value of Mn^{4+} and transition from an insulator to a metal around the ferromagnetic T_C. In the metallic phase, the double exchange favors itinerant electron behavior, promoting conductivity. However, this mechanism is opposed by the Jahn-Teller distortion due to the presence of Mn^{3+}. These manganites can exhibit unusually high resistivities, even in the metallic regime, and do not always obey the criteria for metallicity. These manganites also show charge-ordering, especially when the size of the A-site cations is small and the quantity of B-site Mn and transition metal dopant are equal. Charge ordering, if it occurs, is in the insulating phase, and the dominant exchange coupling thus is superexchange [17].

While many of these effects were known much earlier, appreciation for, and interest in, the degree of sensitivity of these manganites to magnetic fields has increased in recent years due to works such as Jin et al., 1994 [15]. For instance, magnetic fields have been shown to suppress charge ordering in these manganites [18].

Interests in these manganites include applications in technology and basic research aimed at understanding the origin of the large magnetoresistance. Giant magnetoresistance multilayer metallic films are an example of recent technological

applications. They have a relatively large sensitivity to magnetic fields known as the spin-valve effect between spin-polarized metals that is reversible. This effect has enabled new advances in the magnetic storage industry in the form of magnetoresistive read heads.

1.3 CRYSTAL STRUCTURE

The ideal perovskite structure is cubic (Figure 1-1) with the BO_6 octahedra sharing their corners and the A cations occupying the 12-fold cavities created by the 8 BO_6 octahedra, or oxygen octahedra. In $La_{0.7}Sr_{0.3}MnO_3$, the electronic configurations of Mn^{3+} and Mn^{4+} are $3d^4$ and $3d^3$ respectively. Due to cation size mismatch on the A-site and the Jahn-Teller effect on the MnO_6 octahedra, they have a slightly distorted cubic structure with the A cations having a 12-fold coordination with the O anions. The perovskite structure is known to be very flexible and the A and B ions can include various ions such as La^{3+}, Sr^{2+}, Ba^{2+}, Ca^{2+} on the A-site and $Mn^{3+/4+}$, Ni^{3+}, Cr^{3+}, Fe^{3+}, Co^{3+}, Zn^{3+} to name a few on the B-site, leading to a large number of known compounds with perovskite structures. The valence and quantity of the B-site ions are highly influenced by the ionic radius and quantity of the A-site dopant. The perovskites studied in this dissertation have a rhombohedral structure (Figure 1-2), that is only slightly distorted from cubic (typically on the order of a few degrees from cubic).

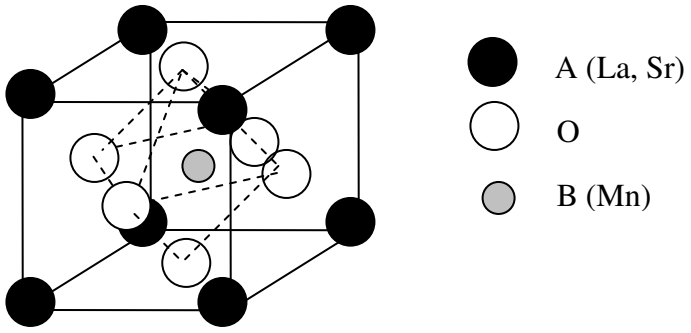

Figure 1-1 The ideal, cubic structure of an ABO_3-type manganese perovskite with the A-site typically filled by a La^{3+}, Ca^{2+} or Sr^{2+} (large cation ions) and the B-site filled by Mn^{3+}, Mn^{4+}, Cr^{3+}, Ni^{3+} or other small cation while the oxygen ions form an octahedron around the B-site cation.

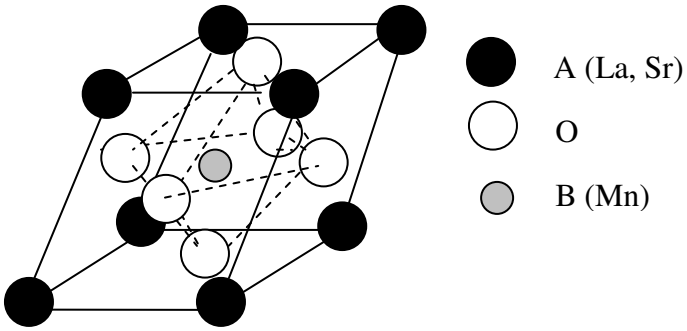

Figure 1-2 The rhombohedral (space group $R\bar{3}c$) structure of a $La_{0.7}Sr_{0.3}MnO_3$ perovskite.

1.4 OCTAHEDRAL FIELD SPLITTING

When a transition-metal ion is surrounded by 6 oxygen (negative) ions in an octahedral configuration such as the case of the perovskites, the five-fold degenerate 3d-orbitals are split into two different energy groups, an upper doublet, e_g^2, and a lower triplet, t_g^2 Dunitz and Orgel 1957 [19]. This splitting is due to the influence of the cubic crystal field (Figure 1-1), or more simply, the electrostatic repulsion between the *d* electrons and the surrounding negative ions causes a splitting of the energy levels. The e_g^2 orbitals ($d_{x^2-y^2}$, d_{z^2}) align directly with the negative oxygen ions and are destabilized

while the t_g^2orbitals (d_{xy}, d_{xz} and d_{yz}) point in directions where the field is least (between the ions) and are therefore stable. As successive electrons are added into the d shell, they occupy the lowest available orbitals compatible with the total spin associated with the metal ion. In Mn^{3+}, there are three t_g^2 orbitals in the high spin state (S = 2) and the remaining electron is excited into the e_g^2 orbital whose spin is parallel to the spins of t_g^2 -electrons of neighboring Mn-atoms due to strong Hund's rule coupling. However, in Mn^{4+}, there are only three electrons in the 3*d*-shell, and all three t_g^2 orbitals are filled with a single electron each, providing a total spin *S* =3/2.

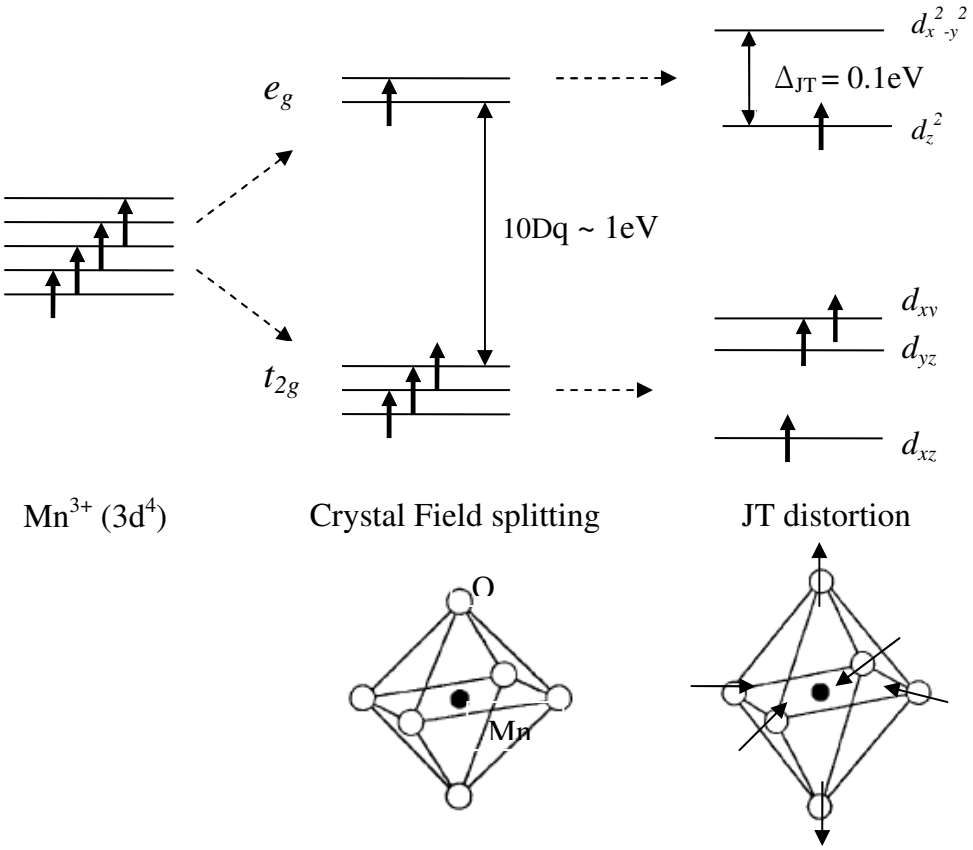

Figure 1-3 Crystal field splitting of the d-level electrons and the additional splitting due to the Jahn Teller distortion.

1.5 JAHN TELLER DISTORTIONS

The Jahn–Teller (JT) effect, named after Hermann Arthur Jahn and Edward Teller [20, 21], provides that orbital nonlinear spatially degenerate molecules cannot be stable, or, that any nonlinear molecule with a spatially degenerate electronic ground state will undergo a geometrical distortion that removes the degeneracy, lowering the overall energy of the molecule. Stability exists when the configuration in which the electronic state is degenerate is linear (all nuclei lie on a straight line), or the system contains an odd number of electrons and the degeneracy is the twofold Kramer's degeneracy [22], which cannot be removed by any changes in the electrostatic field. Thus, Jahn and Teller have shown that in addition to the splitting of the 3*d*-orbitals under the influence of the cubic crystal field, there is another splitting of the e_g^2 orbital of a non-linear, orbitally degenerate atom, such as Mn^{3+} in the MnO_6 octahedra, that is due to energy-lowering distortions. A distortion of the oxygen octahedron lowers the symmetry of the cubic crystal field, and lowers the energy of the atom. This distortion proceeds until the extra stability gained by the distortion is just balanced by the energy required to stretch and compress the bonds. The magnitude of the Jahn-Teller distortions depend on the bonding or antibonding power of the degenerate electrons and, will vary between the different transition-metal ions according to their electronic configurations. There are several types of Jahn-Teller distortions, including, cooperative static, dynamic, and local distortions. The cooperative static Jahn-Teller distortions are ones in which the distortion remains fixed and does not move, as when lattice structures are predominantly comprised of Mn^{3+}. In the perovskites, the Mn^{3+} ion is generally referred to as a Jahn-Teller ion where the splitting of Mn^{3+} electrons in the e_g^2 orbital causes an elongation of the [MnO_6]

octahedron that leads to an energy gain that is an order of magnitude lower ($\Delta_{JT} \approx 0.1$ eV) than the energy difference between the e_g^2 and t_g^2levels. When a Mn^{3+} ion replaces a Mn^{3+} ion in the lattice, there is one additional electron introduced locally into the e_g^2-orbit of one lattice site, resulting in a local Jahn-Teller distortion. A polaron is formed when the e_g^2 electron hops from one Mn-site to the neighboring one such that the Mn^{3+} and Mn^{4+} ions switch places. The effect of these distortions is to lower the symmetry of the cubic crystal field, thereby elongating or shortening the bonds and lowering the overall energy. A dynamic Jahn-Teller distortion occurs when the distortion changes within the lattice over time. The lattice distortions can be characterized by the Goldschmidt tolerance factor

$$\tau = \frac{\langle R_A \rangle + R_O}{\sqrt{2}(\langle R_B \rangle + R_O)}$$

where R_A, R_B and R_O, are the average ionic radius of the A-site, B-site and oxygen ion respectively.[12] For $\tau<0.96$, the structure tends to be orthorhombic while for $0.96<\tau<1.0$, the structure tends to be rhombohedral. If $\tau=1.0$, the structure is cubic. However, it is also well known that not all the bonds in the perovskites are ionic so the tolerance factor is used as a general guide, not a rule.

Magnetic polarons are magnetically ordered clusters formed when an electron enters into a conduction band accompanied by a localized deformation, an electron with induced lattice polarization. The reduction in energy by moving in a spatially localized level with the local deformation provides the mechanism allowing exchange between bound carriers and localized spins [23, 24, 25, 26]. Polarons have more mobility than ionic defects.

1.6 B-SITE SPIN CONFIGURATION AND HUNDS RULE

The order in which electron sub-shells tend to be filled also determines the spin configuration of these free atoms and ions in their ground states. This filling can be determined by applying Hund's rule: every orbital in a subshell is singly occupied with one electron before any one orbital is doubly occupied, and all electrons in singly occupied orbitals have the same spin. The origin of this rule lies in the mutual repulsion of electrons. It is due to this repulsion, that the farther apart the electrons are, the lower the energy of the atom is. Electrons in the same subshell with the same spin must have different m_i values and accordingly, are described by wave functions whose spatial distributions are different. Electrons with parallel spins are therefore more separated in space than they would be if they were paired off. This arrangement, having less energy, is the more stable one. In other words, spin and angular momentum can be couched using Hund's rule as follows:

(1) The total spin angular momentum, S= $\sum_i m_{S_i}$ such that no two electrons in an atom can occupy the same quantum state (each electron must have a different set of quantum numbers n, l, m_l,and m_s).

(2) Total orbital angular momentum $\boldsymbol{L} = \sum_i m_{l_i}$ consistent with rule (1).

(3) Total angular momentum $\boldsymbol{J} = |L - S|$ for a shell less than half full and $L + S$ for a shell more than half full.

The above rules allow us to specify the spin configuration and spin only magnetic moment of the B-site metal ions. The degeneracy of the 3*d*-orbital in the 3*d*-transition

metal ions is lifted due to the crystal field generated by the surrounding ions. Once the degeneracy is lifted, the resulting orbital angular momentum $\boldsymbol{L}$ equals zero. Once the orbital angular momentum is quenched, the magnetic moments of 3*d* transition metals will stem predominately from the total spin angular momentum $\boldsymbol{S}$.

1.7 ELECTRONIC EXCHANGE AND ORDERING MECHANISMS

The electronic exchange mechanisms in the manganese-based perovskites responsible for the magnetic, electronic and transport properties have predominately been attributed to double exchange [4] and ferromagnetic and antiferromagnetic superexchange [27]. In 1955, Goodenough and Loeb[28] proposed another exchange mechanism, semi-covalent exchange, where they argued that in the transition metals, the (n)d and (n+1)s orbitals differ very little in energy, allowing for the easy formation of covalent bonds, that by nature, involve orbital overlap. However, this exchange mechanism has largely not been adopted. To a lesser degree, physical and electronic interactions and ordering phenomena also shape the magnetic, electronic and transport properties, including charge ordering, orbital ordering, electron-phonon interactions and Jahn-Teller [21] distortions. The Mn atom has an $[Ar]3d^5 4s^2$ electron configuration. Therefore, the Mn^{4+} ion consists of three electrons, $[Ar]3d^3$, with parallel spins in the degenerate t_{2g} states (Figure 1-3) of (3_{dxy}, 3_{dyz}, 3_{dzx}) and empty e_g orbitals, while the Mn^{3+} ion has an additional electron in one of the higher-energy degenerate e_g states (Figure 1-3) of ($3d_{x^2-y^2}, 3d_{3z^2-r^2}$) that causes it to have a strong electron-phonon coupling as a Jahn-Teller ion. Therefore, lattice distortions necessarily play an important role in determining the ground states and physical properties of the manganites [21].

1.8 DOUBLE EXCHANGE INTERACTION

The double exchange mechanism Zener [4], favors a ferromagnetic exchange of electrons between Mn^{3+} and Mn^{4+} using the oxygen ion as an intermediary, due to a strong Hund's rule coupling (Figure 1-4). This rule only allows parallel spins of the charge carriers to the local spin of neighboring atoms. Therefore, the charge carrier hops to a neighboring site without changing its spin. Zener described the double exchange mechanism as a double charge transfer via a Mn^{3+} (t^3e^1) - O^{2-} ($2p_\sigma^2$) - Mn^{4+} (t^3e^0) bond whereby the e^1 electron from Mn^{3+} displaces the like-spin O-$2p_\sigma$ electron to the empty e^0 orbital on the Mn^{4+} ion. This mechanism is usually written as Mn^{3+}-O-Mn^{4+} double exchange. Anderson and Hasagawa [7] in 1955 further described the double exchange as the effective hopping of an electron between Mn neighbors, involving the oxygen *2p*-orbital and the Mn *3d*-orbitals (t_{pd}). Theoreticians like Millis et al., 1995 [16] pointed out that the theoretical framework used within the double exchange mechanism does not hold up when examined quantitatively. Instead, it is also necessary to consider the physics of a strong electron-phonon interaction arising from the Jahn-Teller splitting of the outer Mn d-level electrons. Kubo and Ohata [14] later provided a full quantum mechanical interpretation for the double exchange mechanism.

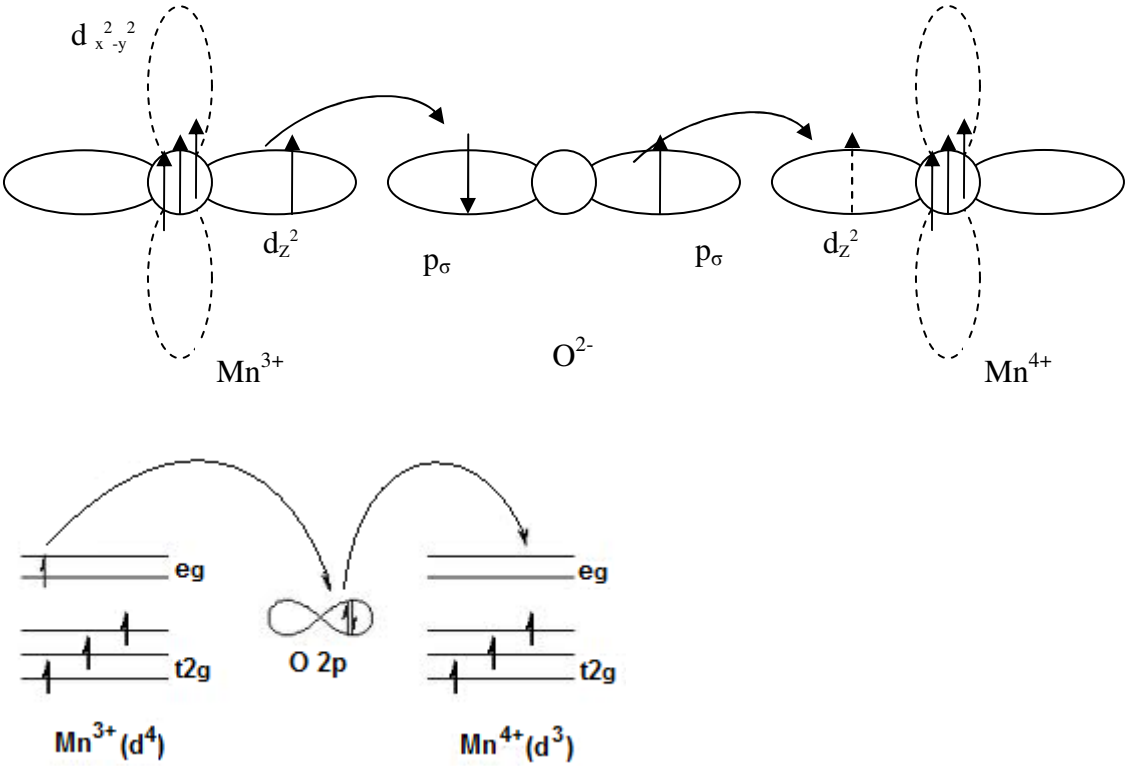

Figure 1-4 Double exchange interaction between Mn^{3+} and Mn^{4+}. As the arriving and departing electrons via the O-($2p_\sigma^2$) orbital must have the same spin orientation, ferromagnetic coupling occurs between Mn^{3+} and Mn^{4+} (small circle for the t_{2g} orbitals, lobes for the e_g orbitals, and arrows indicating electron spin direction. Empty e_g orbitals are indicated by dotted lines).

1.9 SUPEREXCHANGE INTERACTION

Kramers [27] first suggested that it is possible to have an exchange spin-coupling between magnetic atoms via an intermediary, non-magnetic atom, giving rise to what is known as superexchange. In the perovskite system, the intermediary is the oxygen ion that lies between the two Mn ions. Therefore, superexchange is an indirect spin-spin exchange process in poor conductors where the distance between the magnetic ions is large, prohibiting a direct exchange. The dipole-dipole exchange interaction is weaker than the superexchange interaction and the superexchange mechanism is the primary mechanism for the magnetism. The spin coupling takes place between two like-charged

Mn-ions, for instance, two Mn^{3+} or two Mn^{4+} ions, via the O^{2-} ion lying in between without any charge transfer (Figure 1-5).

The orbitals in a pure ionic bond do not overlap. In reality there is some weak covalent bonding between the Mn and the O-atoms. Since this covalent bonding is weak, the perturbation of the electron movement is weak, causing the electrons to remain localized and resulting in a spin structure with an antiferromagnetic ordering of the 3*d* spins (Figure 1-5). However, this coupling can also be ferromagnetic. For realization of ferromagnetic coupling, the Goodenough-Kanamori [44, 45] rules must be implemented: (1) Strong antiferromagnetic exchange occurs when two like-cations with occupied d-orbitals at neighboring sites overlap with the anion (oxygen) 2p-orbitals, (2) The exchange can be moderately ferromagnetic when one cation has occupied t_{2g} orbitals and half-filled e_g orbitals, while the other has occupied t_{2g} orbitals but empty e_g orbitals that overlap. However this exchange is much weaker than in the antiferromagnetic case.

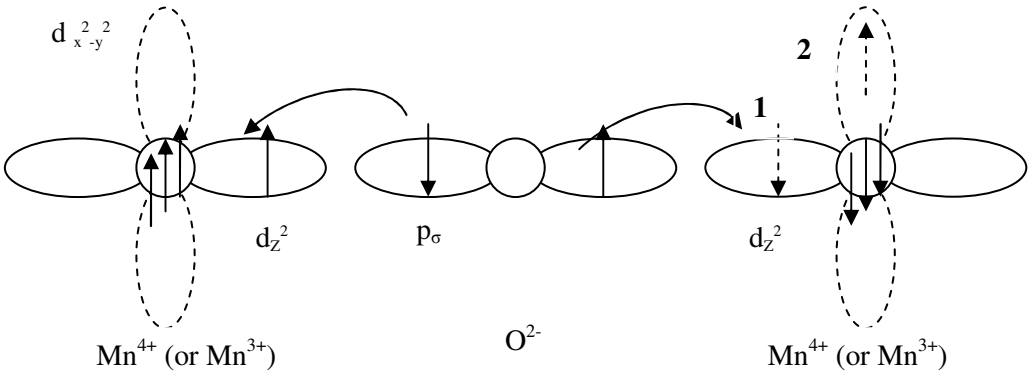

Figure 1-5 Antiferromagnetic superexchange interaction between two Mn^{3+}(or Mn^{4+}) ions with occupied overlapping orbitals with the O *2p*-orbitals (small circle for the t_{2g} orbitals, lobes for the e_g orbitals, and arrows indicating electron spin direction. Empty e_g orbitals are indicated by dotted lines).

1.10 CHARGE ORDERING

Upon doping, the manganite's exhibit charge-ordering that is particularly pronounced when the ratios of Mn^{3+} to Mn^{4+} are rational fractions. A charge-ordered condition exists when the interatomic long-range Coulomb interaction between the charge carriers overcomes the kinetic energy of these same carriers. The condition can be a first or second-order condition and is most common in strongly correlated electron systems such as exist in the transition metal oxides. The condition exists when mobile d-electrons are localized on certain sites, forming a regular ordered superlattice for specific occupancies of the d-band electrons, provided that the interelectronic Coulomb interaction is comparable with the conduction-electron bandwidth [29, 30, 31, 32]. For instance, a charge ordered insulating state can occur when electrons become localized within an antiferromagnetic insulating phase of a perovskite. The manganites show charge-ordering mostly when the temperature is low and the value of the mixed cations is a rational fraction (e.g. the ratio of Mn^{3+} to Mn^{4+} is $\frac{1}{8}, \frac{1}{4}, \frac{1}{2}, or\ \frac{3}{4}$. Small displacements of the oxygen atoms accommodate the ordered cation lattice. The extra fourth *d* electrons can then localize on alternate manganese sites in a plane, favoring insulating behavior.

1.11 SYNTHESIS

Many perovskites are typically synthesized by solid state reactions that yield polycrystalline samples. The precursors are usually simple binary oxides or pure elements. Precursors are typically dried ahead of time in a warming oven or kept under vacuum in a dry environment, measured stoichiometrically, mixed and ground thoroughly

and pressed into pellets. Once pressed into pellets, they are fired at temperatures sufficient for calcination (decomposition of any carbonates used in the precursors) for up to 48 hours. Once cooled, the pellets are ground and mixed again, pressed into pellets and calcined for up to 48 additional hours. This process is typically repeated several times to insure homogeneity of the polycrystalline samples. The process is repeated one final time at a temperature sufficient to produce the desired solid-state reaction of the precursor elements to form the perovskite structure but at temperatures that do not produce a "melting" of the precursors. These temperatures are usually relatively high and vary depending on the precursors and their respective melting temperatures but generally should not exceed the lowest precursor melting temperature (e.g. the perovskites studied in this thesis were fired at 1350C). The desired effect is to achieve approximately a 90% or better solid-state reaction of all combined elements to produce the polycrystalline samples.

1.12 NEUTRON DIFFRACTION

Neutron diffraction is the only direct method whereby the magnetic structures of materials can be determined. The neutron magnetic moment is about $1.9\mu_N$ (nuclear magnetons) or about 10^{-3} μ_B (Bohr magneton = 9.273×10^{-21} erg). Neutrons behave as particles when they are created, as waves when they scatter, and as particles when they are detected.

The neutron has a spin of one-half. If the target atom or ion has a net spin, the interaction of the spin of the neutron with the spin of the nucleus of the target atom determines the scattering property of the neutron with the target atom. This spin-spin

interaction leads both to coherent and incoherent scattering. The coherent scattering produces diffraction effects while the incoherent scattering, is observed as general background noise. In non-magnetic materials, the neutron scatters predominately off the nucleus, but does also interact with the electric charges in the nucleus. However these latter interactions are extremely small being a factor of about 10^4 less than the nuclear scattering and are not further discussed in this dissertation. The size of the nucleus is very small compared to the size of the electron cloud and to the wavelength of neutrons. Thus, in nonmagnetic materials, the amplitude of neutrons scattered off the nucleus will not depend on the scattering angle, thus providing a nearly straight line "form factor". The same is not true for neutrons scattering off magnetic materials because it is the unpaired electrons in the unfilled electron shells that provide the magnetic moment that interacts with the neutron magnetic moment.

Neutrons penetrate deep into the material. However, the penetrating ability of neutrons is countered by the fact that they are weakly scattered once they do penetrate. Neutron scattering can be elastic or inelastic with the total energy and momentum conserved during the process. In the case of inelastic scattering, some of the energy from the neutron is absorbed by the nucleus of the target atom.

Thermal neutrons from reactors are expensive and scarce but their scattering is a valuable tool for investigating many important features of matter. Some of the most compelling advantages for using neutrons include:

Neutrons are a bulk probe, only weakly absorbed except for B, Cd, Sm, Eu and Gd.

The wavelength of thermal neutrons is of the order of typical interatomic distances in solids and liquids. Therefore, diffraction effects are realized and information on the structure of the materials can be obtained.

Neutrons are scattered by atomic nuclei (except for magnetic scattering) by very short range (~fm) forces, so the neutron form factor is nearly a straight line as opposed to x-rays scattering from the extra-nuclear electrons, which is proportional to the atomic number *Z*.

The neutron has a magnetic moment allowing it to be scattered by unpaired electrons via magnetic dipole interactions in magnetic atoms. This elastic scattering provides information about the magnetic moment and magnetic ordering of magnetic atoms.

Neutron cross sections are isotope–dependent in a more or less random manner, allowing neutron scattering to not be dominated by the heavy atoms, as are x-rays.

Thermal neutron energies are of the same order as that of many elementary excitations in condensed matter, causing significant changes in neutron energy and wavelengths when the neutron is inelastically scattered by the creation or annihilation of an excitation.

The measurement of the scattered neutron requires the observation of the neutron interacting with another particle. Therefore, neutron detection requires "detectors" to be made of materials such as boron, helium-3 or lithium that absorb neutrons strongly in order to produce ionizing radiation for measurement. All neutron-diffraction data were collected at the MURR facility (Appendix B) using a position sensitive detector diffractometer with a neutron wavelength of $\lambda = 1.479$Å. MURR houses a tank-type

nuclear research reactor, servicing the University of Missouri's Nuclear Science and Engineering Institute (NSEI) in Columbia (see Appendix B).

1.13 RIETVELD METHOD

Hugo Rietveld joined the group at the Reactor centrum Nederland (now Netherlands Energy Research Foundation ECN) in 1964 where the emphasis was on building a neutron powder diffractometer to study powder samples as no large, single crystals could be grown of the materials of interest at the time. He presented a new method for analysis of data from powder samples at the Seventh Congress of the IUCR in Moscow in 1966. However, little reaction was received until the full implementation of the method was published in 1969 and was not generally accepted until 1977. It was his unselfish sharing of his methods that has enabled the great advances in the ability to extract detailed crystal structural information from powder diffraction data. Instead of using the integrated intensities, the Rietveld method uses the individual intensities at each step, y_i, of a step-scanned pattern as data. For constant wavelength data, these steps are usually steps in scattering angle, and the intensity y_i at each step *i* in the pattern is usually measured by a diffractometer. The least-squares method is used to obtain the best fit between the entire observed powder diffraction pattern taken as a whole and the entire calculated pattern based on simultaneously refined models of the crystal structures. The powder diffraction pattern of any polycrystalline material may be thought of as a collection of individual reflection profiles. Each of these profiles has a profile function, a peak height, a peak position, a breadth, and an integrated area which is proportional to the

Bragg intensity, I_K (K stands for the Miller indices, h, k, l). This intensity is proportional to the square of the absolute value of the structure factor, $|F_K^2|$:

$$F_K = \sum_j N_j b_j \exp[i2\pi(hx_j + ky_j + lz_j)]\exp[-W_j]$$

where:

N_j is the occupancy of the jth atom.

b_j is the scattering length of the jth atom.

h, k, l are the Miller indices.

x_j, y_j, and z_j are the position parameters of the jth atom in the unit cell.

W_j is the Debye-Waller factor, $W_j = 8\pi^2 \overline{u_s^2} \sin^2\theta / \lambda^2$.

$\overline{u_s^2}$ is the root-mean-square thermal displacement of the j_{th} atom parallel to the diffraction vector.

The goal of the method is to find the best fit between the observed intensity and calculated intensity. The refinements have been proven to be robust and it has been found that the Rietveld method can do multiphase refinements accurately, including magnetic phases. Parameters refined in multiphase analyses may be treated dependently or independently as separate phases

The Rietveld method minimizes the residual, S_y:

$$S_y = \sum_i \omega_i (y_i - y_{ci})^2$$

where $\omega_i = 1/y_i$

y_i=observed intensity at the ith step

y_{ci}=calculated intensity at the ith step

and the sum is over all data points.

For more information on the Rietveld method, see [34].

1.14 NEUTRON DIFFRACTION STUDY OF $LAMNO_3$

In LaMnO3, the four *3d* electrons on the Mn^{3+} B-site share both the lower t_{2g} band and the higher e_g band ($3d^4$:$t_{2g}^3 e_g^1$). Due to the strong Hund coupling, all the spins are parallel on a given Mn site. The highly correlated electrons in the e_g band create the large correlation gap above the Fermi energy. A neutron diffraction study of the $LaMnO_3$ parent compound was reported by Carvajal et al in 1998 [35]. It was known by that time that this system is an antiferromagnetic insulator where orbital ordering is established via the cooperative Jahn-Teller effect breaking the degeneracy of the electronic configuration of Mn^{3+} ($t_{2g}^3 e_g^1$). They used two powder diffractometers at the Orphe´ Reactor at Laboratoire Le´on Brillouin in their study. They used the G4.2 diffractometer to study the crystal structure behavior as a function of temperature and the diffractometer 3T2 for

refining the crystal structure. They used the FullProf program and Rietveld method to analyze the experimental data. Their powder samples of $LaMnO_3$ were prepared by crushing single-crystal ingots grown by the floating zone method [36].

Caravajal et al [35] observed two transitions upon heating, one at T_1=750 K and the second at T_2=1010 K (Figure 1-6). Their neutron diffraction (Table 6.1) indicates that below T_1 the unit cell is orthorhombic, while between T_1 and T_2 the reflections can be indexed either assuming a double cubic perovskite cell or an orthorhombic cell. Above T_2, the

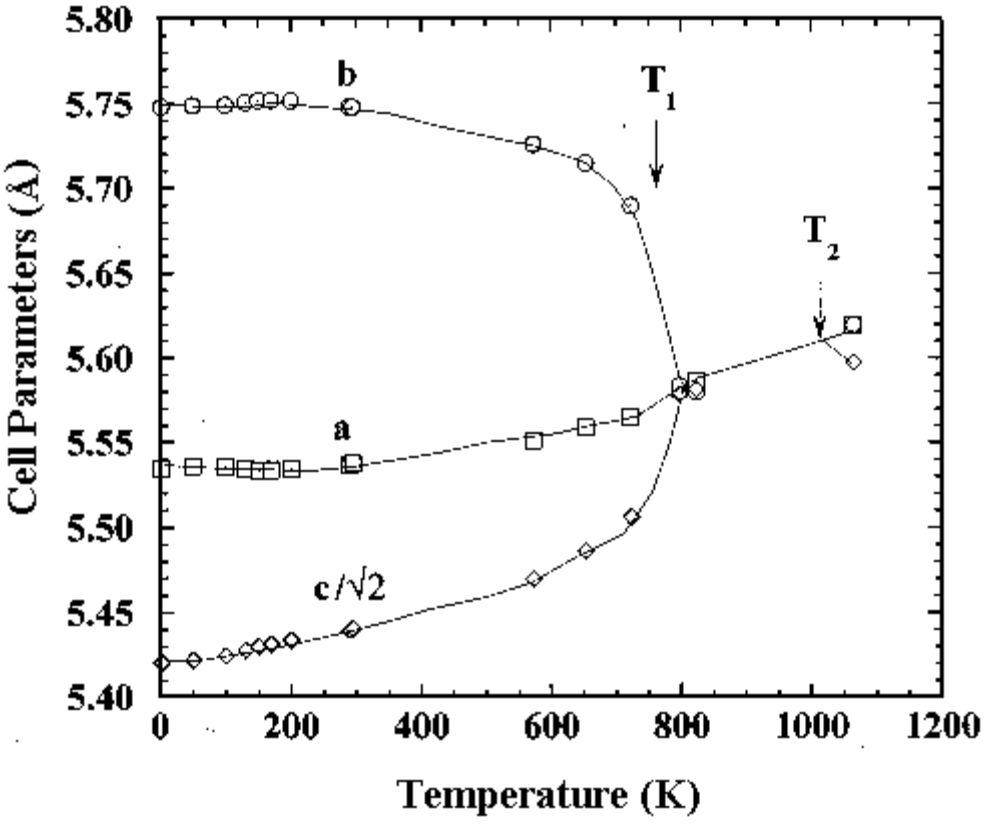

Figure 1-6 Cell parameters of $LaMnO_3$ as a function of temperature from Carajaval et al [35].

reflections are indexed using an $R\bar{3}c$ rhombohedral cell. They noted that in comparison to other studies at the time, a small amount of Mn^{4+} in the $LaMnO_3$ system appeared to increase the *c* axis while diminishing the orthorhombic strain. They suggested the T_1 transition, while occurring with no change to the average crystallographic symmetry, could be attributed to the suppression of the cooperative Jahn-Teller effect (T_1=T_{JT}). Finally, they observed that at temperatures higher than T_{JT}, the orbital ordering disappears, witnessed by a diminishing distortion in the MnO_6 octahedra in transitioning from the O' phase to the *O* phase.

Table 1-1 Structural data for $LaMnO_3$ (Pbmn) at three temperatures [35].

	300K	573K	798K
a (Å)	5.5367 (1)	5.5520 (2)	5.5817 (3)
b (Å)	5.7473 (1)	5.7269 (2)	5.5834 (2)
c (Å)	7.6929 (2)	7.7365 (2)	7.8896 (4)

1.15 SUBSTITUTION OF La BY Sr

Sr doping introduces holes in the e_g band near the Fermi energy, producing mobile holes and conduction by conversion of Mn^{3+} to Mn^{4+}. Asamitsu et al [37] provided evidence that the crystal structure of $La_{1-x}Sr_xMnO_3$ can, for a limited range of x, be switched-reversibly or irreversibly, depending on the temperature, by applying an external magnetic field. The magnetic and transport properties of these manganites have been described with double exchange, super exchange, semicovalent exchange, Jahn-

Teller distortions, and electron-phonon couplings. However, Millis et al [16] provided theoretical evidence that double exchange between Mn^{3+}-O-Mn^{4+} could not account for discrepancies between calculated and observed resistivities. Urushibara et al [38] studied melt-grown $La_{1-x}Sr_xMnO_3$ crystals ($x \leq 0.6$) using x-ray diffraction, magnetic and electrical measurements. They found the lattice parameters a and b decrease while c increases with increasing Sr content within the orthorhombic phase ($x<0.175$). All the lattice parameters decreased with increasing Sr content in the rhombohedral phase ($x>0.175$) (Figure 1-7). Their magnetic phase diagram for $La_{1-x}Sr_xMnO_3$ is provided in Figure 1-8. They also produced an electronic phase diagram vs Sr content (Figure 6.3) where they noted the T_C is max for x~0.4 (Figure 1-9).

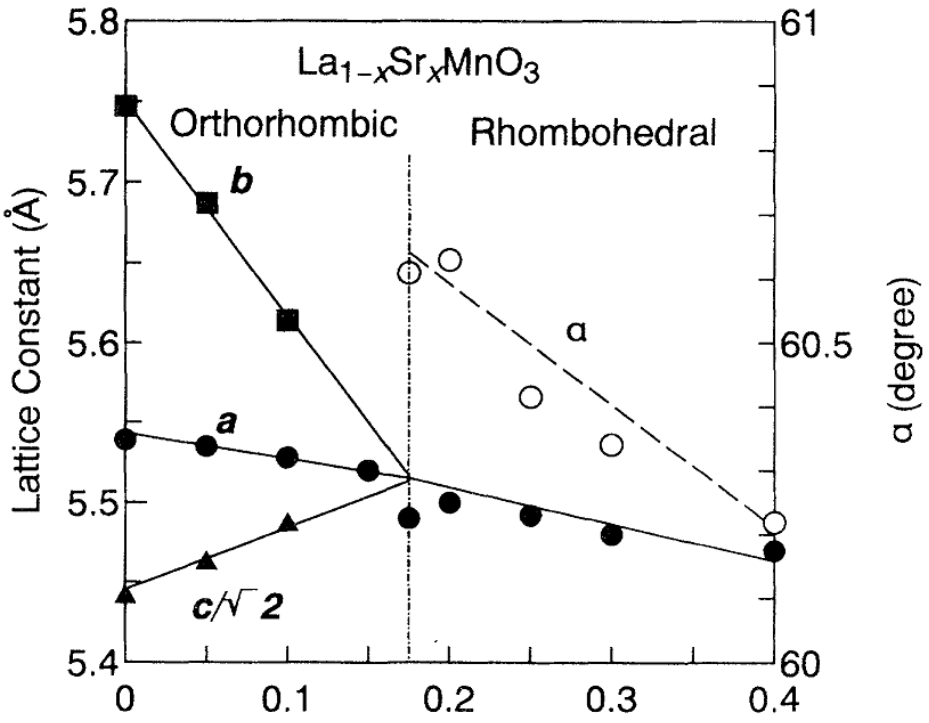

Figure 1-7 Lattice parameters for $La_{1-x}Sr_xMnO_3$ at room temperature from Urushibara et al [38].

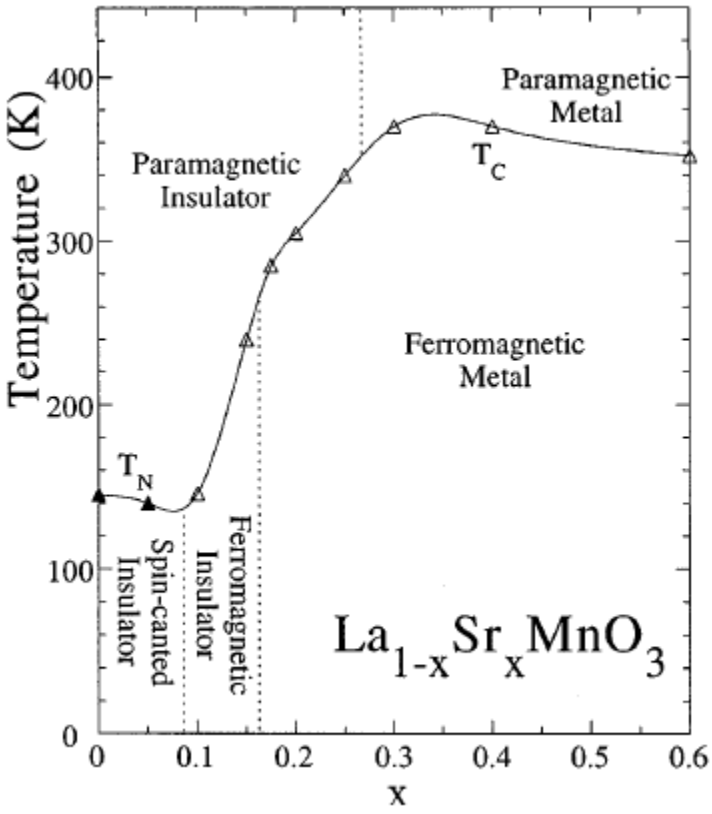

Figure 1-8 Magnetic phase diagram for $La_{1-x}Sr_xMnO_3$ from Urushibara et al [38]. Open circles and filled triangles are the Neel temperature (T_N) and the T_C temperatures respectively. The abbreviations mean paramagnetic insulator (PI), paramagnetic metal (PM), spin-canted insulator (CNI), ferromagnetic insulator (FI), and ferromagnetic metal (FM).

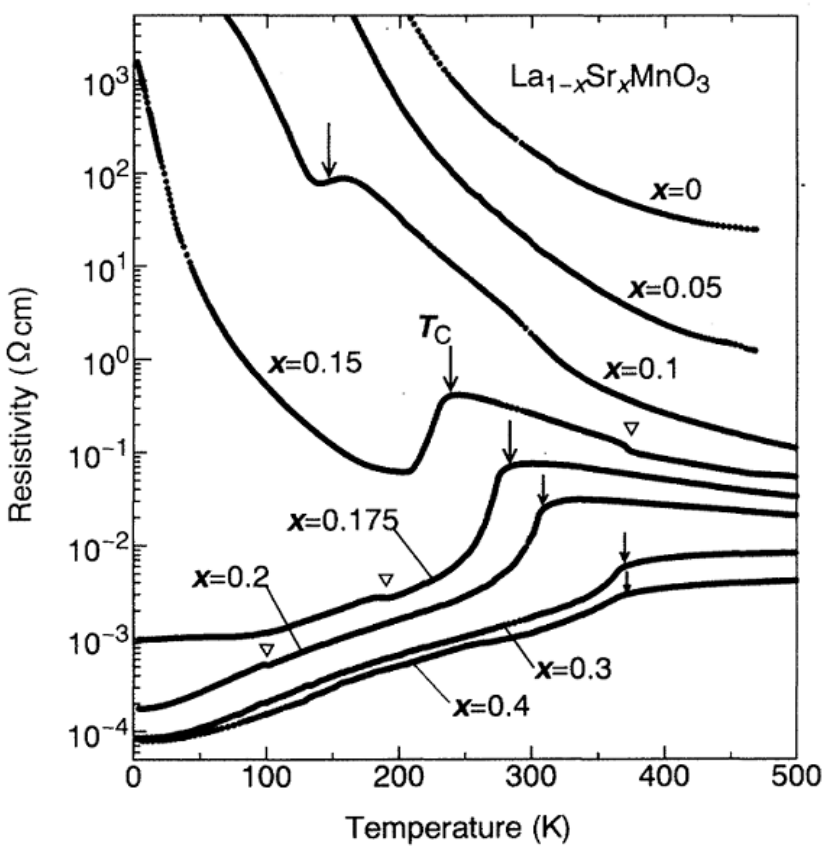

Figure 1-9 Temperature dependence of resistivity for $La_{1-x}Sr_xMnO_3$ from Urishabara et al. [38]

Martin and Shirane [39] studied the magnetic and nuclear structure of a single crystal of $La_{0.7}Sr_{0.3}MnO_3$ using neutron diffraction. They found the magnetic moment per Mn site to be $\mu \sim 3.6\mu_B$. The structure was nearly cubic with a=3.87+/-0.003 Å at room temperature, and the rhombohedral distortion in α was 90.46+/-0.03°. The magnetic interactions were well explained by the double exchange hopping mechanism [40, 41, 42, 43].

1.16 REFERENCES

1. G. Jonker and J. Van Santen, Physica, 16, 337
2. J.H. Van Santen and G.H. Jonker, Physica, 16, 7-8, 599 (1950)
3. G. Jonker, Physica, 20, 1118 (1954)
4. Zener, C., Phys. Rev., vol. 82, 403-405 (1951)
5. Wollan, E. O., Koehler, W. C., Phys. Rev., 100, 545-563, (1955)
6. J. Volger, Physica, 20, 49 (1954)
7. P. Anderson, and H. Hasegawa, Phys. Rev., 100, 675 (1955)
8. P. de Gennes, Phys. Rev., 118, 141 (1960)
9. J. B. Goodenough, A. Wold, R. Arnott, N. Menyuk, Phys Rev. 124, 373 (1961)
10. C. Searle, and S. Wang, Can. J. Phys., 47, 2703 (1969)
11. A. Morrish, B. Evans, J. Eaton and L. Leung, Can. J. Phys., 47, 2691 (1969)
12. L. Leung, A. Morrish and C. Searle, Can. J. Phys., 47, 2697 (1969)
13. J. B. Goodenough, J. M. Longo “Landolt Bornstein numerical data and functional relationships in science and technology”)Ed. K. H. Hellwege, A. M. Hellwege) Springer Verlag. Berlin Heidelberg (1970) Group III Vol. 4a. Cap. 3.
14. K. Kubo, N. Ohata, J. Phys. Soc. Jpn., 33, 21 (1972)
15. S. Jin, M. McCormack, T. Tiefel, R. Ramesh, J. Appl. Phys., 76, 6929, (1994)
16. A. J. Millis, P. B. Littlewood, and B. I. Shraiman, Phys. Rev. Lett., 74, 25, 5144 (1995)
17. C. N. R. Rao, A. Arulraj, A. K. Cheetham, B. Raveau, J. Phys.: Condens. Matter 12, R83 (2000).

18. Y. Tomioka, A. Asamitsu, H. Kuwahara, and Y. Moritomo, Phys. Rev. B 53, R1689 (1996)

19. J. D. Dunitz and L. E. Orgel, J. Phys. Chem Solids, 3, 20 (1957)

20. H. A. Jahn, Proc. Roy. Soc. A, 164, 117 (1938)

21. H. A. Jahn, and E. Teller, Proc. Roy. Soc. A, 161, 220 (1937)

22. H. A. Kramers, Proc. Acad. Sci. Amsterdam , 33, 959 (1930)

23. T. Kasuya, and A. Yanase, Rev. Mod. Phys., 40, 684 (1968)

24. T. Kasuya, A. Yanase, and T. Takeda, Solid St. Com., 8, 1543, (1970)

25. T. Kasuya, Solid St. Com., 8, 1635 (1970a)

26. T. Kasuya, Proceedings of the Tenth International Conference on the Physics of Semiconductors, 243 (1970)

27. H. A. Kramers, Physica 1, 182 (1934)

28. J.B. Goodenough and A. L. Loeb, Phys Rev., 98, 2, 391 (1955)

29. E. J. W. Verwey, P. W. Haaymann, and F. C. Romeijin, J. Chem. Phys., 15, 181 (1941)

30. C. H. Chen, S-W. Cheong, and A. S. Cooper, Phys. Rev. Lett., 71, 2461 (1993)

31. Y. Moritomo, Y. Tomioka, A. Asamitsu, and Y. Tokura, Phys. Rev. B, 51, 3297 (1995)

32. P. D. Battle, T. C. Gibb, and P. Lightfoot, J. Solid State Chem., 84, 271 (1990)

33. The Rietveld Method, edited by R. A. Young

34. H. M. Rietveld, “Profile refinement method for nuclear and magnetic structures.” J. Appl. Crystallogr. 2 65-71 (1969).

35. J. Rodriguez-Carvajal, M. Hennion, F. Moussa, and A. H. Moudden, Phys. Rev. B., **57**, 6, R3189, (1998)

36. A. Revcolevschi and R. Collongues, C.R. Séances Acad. Sci., Ser. A **266**, 1797 (1969); A. Revcolevschi, Rev. Int. Htes. Temps. 7, **73**)~1970).

37. A. Asamitsu, Y. Moritomo, Y. Tomioka, T. Arima and Y. Tokura, Nature, **373**, 407 (1995)

38. A. Urushibara, Y. Moritoma, T. Arima, A. Asamitsu, G. Kido, Y. Tokura: Phys. Rev. B, **51,** 14103 (1995)

39. Martin, M., Shirane, G., Endoh, Y., Hirota, K., Moritomo, Y., Tokura, Phys. Rev., 53 (21) 14285-14290 (1996)

40. C. Zener, Phys. Rev. **82**, 403 (1951).

41. P. W. Anderson and H. Hasegawa, Phys. Rev. **100**, 675 (1955).

42. P. G. deGennes, Phys. Rev. **100**, 564 (1955).

43. K. Kubo and N. Ohata, J. Phys. Soc. Jpn. **33**, 21 (1972).

44. J. B. Goodenough, Phys. Rev. 100, 564 (1955); J. Phys. Chem. Solids 6, 287 (1958); J. Phys. Radium 20, 155 (1959)

45. J Kanamori, J. hys. Chem. Solids 10, 87 (1959)

2. STRUCTURAL AND MAGNETIC PROPERTIES OF $La_{0.7}Sr_{0.3}Mn_{1-x}Cr_xO_3$ ($x \leq 0.5$)

Thomas F. Creel,[1] Jinbo B. Yang,[2] Mehmet Kahveci,[3] Jagat Lamsal,[3] Satish K. Malik,[4] S. Quezado,[4] O. A. Pringle,[1] William B. Yelon,[5] William J. James[5]

[1]*Department of Physics, Missouri University of Science and Technology, Rolla, MO, U.S.A.*

[2]*State Key Laboratory for Artificial Microstructure and Mesoscopic Physics and School of Physics, Peking University, Beijing*

[3] *Department of Physics, University of Missouri, Columbia, MO, U.S.A*

[4] *International Center for Condensed Matter Physics (ICCMP), University of Brasilia, Brasilia DF.*

[5]*Center for Materials Science Research, Missouri University of Science and Technology, Rolla, MO, U.S.A.*

2.1 ABSTRACT

Magnetic and structural properties of $La_{0.7}Sr_{0.3}Mn_{1-x}Cr_xO_3$ (x=0.05, 0.10, 0.20, 0.30, 0.40 and 0.50) have been studied using neutron and x-ray diffraction and magnetic measurements. All samples are found to be of single phase. At 12K, we find only ferromagnetic ordering for $x<0.30$ and coexisting ferromagnetic and antiferromagnetic domains for $x\geq0.30$. Our magnetic data indicate temperature dependent ferromagnetic to paramagnetic, and likely antiferromagnetic to paramagnetic transitions. We find no evidence of spin glass or cluster glass behavior, only long-range magnetic order with a transition to antiferromagnetic behavior beginning with x=0.30 and almost completely antiferromagnetic behavior at x=0.50.

2.2 INTRODUCTION

There has been significant interest in the magnetic and electronic transport properties of manganese-based perovskite materials since the discovery of colossal magnetoresistance and the interesting magnetotransport properties of metallic-doped manganites [1, 2, 3, 4]. Studies of the parent manganite $LaMnO_3$ indicate it to be a layered antiferromagnetic (AFM) charge transfer insulator [1, 2, 3, 4]. The Mn^{3+} and Mn^{4+} ions with electrons in orbitals t_{2g} e_{1g}, and t_{2g} e_{0g} respectively, are the primary mechanism for the double exchange interaction responsible for the layered magnetic interactions [5]. The three t_{2g} electrons have a core spin of S=3/2 while the additional electron in the Mn^{3+} higher-energy e_g state, causes the layered AFM behavior through intrinsic orbital interaction.

Substituting a divalent alkaline-earth metal ion, such as Sr^{2+}, on the A-site for the trivalent La^{3+} ions, creates holes and produces Mn^{4+} ions [2]. With Sr doping concentrations of about 30%, the $LaSrMnO_3$ is a FM metal for temperature $\leq$ 340K, has a Curie temperature (Tc) near 380K, and a magnetic moment per Mn atom of about 3.6 μ_β [6].

Substituting Cr on the B-site, results in an AFM moment from the Cr^{3+}-O-Cr^{3+} exchange mechanism similar to the Mn^{4+}-O-Mn^{4+} exchange mechanism in the non Cr-doped parent perovskites. Magnetic and magnetoresistance measurements indicate that T_C and the lattice parameter "a" decrease with increasing Cr doping and a temperature dependent ferromagnetic (FM) to paramagnetic (PM) transition occurs for all Cr concentrations. Also, for Cr > 20%, an AFM insulating behavior is observed at room

temperature and below [7]. Oxygen non-stoichiometry, electronic structure, X-ray absorption spectra and FM resonance analyses find significant amounts of Cr^{3+} in $La_{1-x}Sr_xMn_{1-y}Cr_yO_3$ but no significant amounts of other Cr ions [8, 9, 10]. Sun et al. have previously interpreted the separation between zero field-cooled and field-cooled magnetic measurements to indicate FM and AFM competition and cluster glass behavior [11, 12]. Other studies have interpreted the magnetic behavior in terms of double-exchange, Jahn-Teller distortions and polaron hopping [10, 13]. It has also been argued that double exchange alone cannot account for all the characteristics of these perovskites [13].

In this study we examine the structural and magnetic properties of $La_{0.7}Sr_{0.3}Mn_{1-x}Cr_xO_3$ perovskites (x=0.05, 0.10, 0.20, 0.30, 0.40 and 0.50) using X-ray diffraction at 300K, neutron diffraction at 12K and 300K, and magnetic measurements. To our knowledge, no neutron diffraction studies for these perovskite compositions have been performed.

2.3 EXPERIMENTAL

Polycrystalline samples of $La_{0.7}Sr_{0.3}Mn_{1-x}Cr_xO_3$ (x=0.05, 0.10, 0.20, 0.30, 0.40 and 0.50) were prepared using a conventional solid-state reaction method in air. Appropriate amounts of high purity La_2O_3, $SrCO_3$, MnO_2, and Cr_2O_3 powders were weighed and mixed according to the desired stoichiometry for each sample. The samples were ground using a high-energy ball mill for 5 hours, pressed into pellets at 2000 psi and then fired at 1350 for 24 hours in air with a rapid quench in air upon removal from the

oven. All processes were performed in air, giving an oxygen-rich environment. After 24 hours of cooling, the samples were re-ground, pressed and fired using the same process.

Neutron-diffraction data were collected at the University Of Missouri Research Reactor (MURR) facility using a position sensitive detector diffractometer with a neutron wavelength of λ = 1.479Å. X-ray data were collected with an XPERT PRO diffractometer using a Cu Kα wavelength of λ = 1.5481Å. Powder diffraction data were refined using the FullProf suite of programs [14]. Magnetic measurements were performed at the University of Brasilia, Brasilia DF, Brazil using a vibrating sample magnetometer and a Quantum Design physical property measurement system (PPMS) with the AC magnetization (ACMS) option.

2.4 RESULTS AND DISCUSSION

Refinements of X-ray diffraction data indicate all samples are single-phase and crystallize in a rhombohedral structure (space group $R\bar{3}c$). The neutron diffraction data were initially refined without including any magnetic phases. Temperature-dependent misfits in the refinements suggested the presence of magnetic scattering. A FM structure based on manganese magnetic moments aligned in the basal plane was then added in subsequent refinements. For x≥0.30, the presence of an additional temperature-dependent reflection not accounted for by the FM structure suggested the presence of AFM scattering. It was found that this peak could be fit with an A-type [2] layered AFM structure, using alternating FM moments on the manganese atoms parallel to the basal plane.

The AFM model alone was not sufficient to fit the x≥0.30 diffraction patterns. The only way to account for all of the magnetic reflections was to include both FM and AFM scattering in the refinements. The coexisting magnetic scattering in the 12K neutron diffraction data for x=0.4 is illustrated in Figure 2-1. The arrows indicate three reflections that contain magnetic intensity. The peak labeled AFM can be fit only by including the layered AFM structure, and the two peaks labeled "FM+Crystal" can be best fit only by including the FM structure. An attempt was made to match the AFM peak with possible impurity phases but none were found.

The results of our neutron diffraction refinements are presented in Table 2-1. The samples with x = 0.05, 0.10, and 0.20 are FM at both 12K and 300K. However, the magnetic scattering at 300K for x = 0.20 is extremely weak. AFM scattering is first observed for x = 0.30 at 12 K, and the AFM moment increases with increasing x. Ferromagnetic scattering is found in all samples at 12K. Manganese magnetic moments are plotted in Figure 2 and indicate a transition from FM to AFM behavior is taking place with likely complicated phase dynamics at x=0.40. Our refinements indicate a single crystal phase.

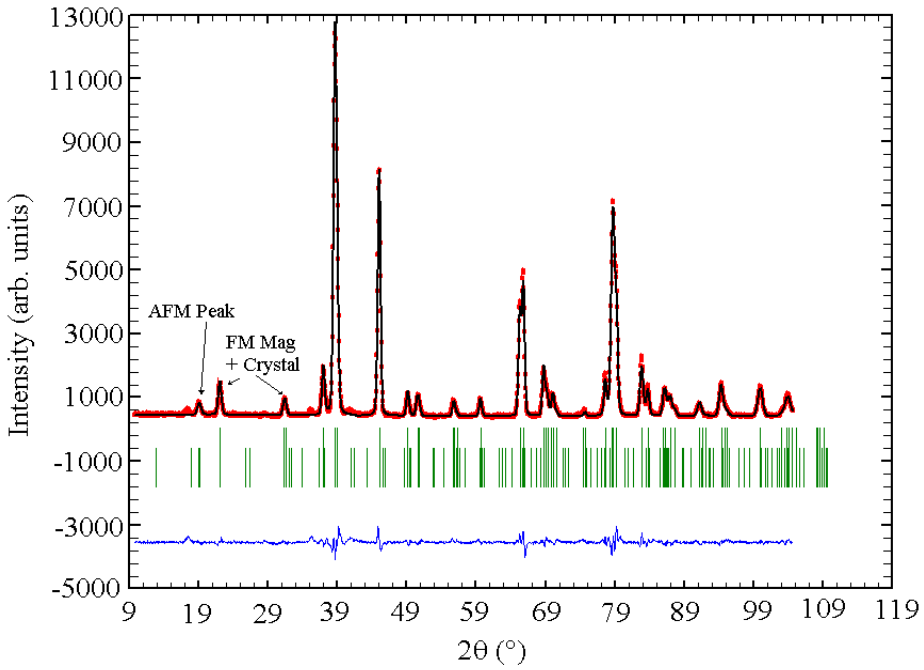

Figure 2-1 Neutron-diffraction pattern for $La_{0.7}Sr_{0.3}Mn_{0.6}Cr_{0.4}O_3$ at 12K with nuclear phase refined. Vertical bars are Bragg peak positions. Arrows point to the AFM peak and two peaks that have FM and nuclear contributions. The small peak just to the left of the AFM peak is due to a small impurity phase believed to be related to MnO.

Visible in Figure 2-2 is an unexpected maximum FM moment observed in the x=0.4 sample. This maximum may be due to an increase in the Mn3+-O-Mn3+ exchanges. Also of interest, is the AFM moment increases more rapidly than the FM moment decreases between x=0.30 to x=0.40.

Table 2-1 Refined parameters; magnetic moment (μ_B), $a_{(rhomb)}$, cell volume and χ^2 versus Cr content from neutron diffraction refinements. The magnetic moments are calculated on the Mn atom occupational sites and represent magnetic moments per Mn site within the cell structure.

CR Content		0.05	0.10	0.20	0.30	0.40	0.50
12K	$\mu_{FM, Mn}(\mu_\beta)$	3.09 (.04)	2.83 (.04)	2.22 (.04)	1.67 (.05)	1.86 (.06)	0.68 (.14)
	$\mu_{AFM, Mn}(\mu_\beta)$	*n/a*	*n/a*	*n/a*	0.45 (.05)	1.15 (.03)	1.47 (.02)
	a(rhomb)	5.491	5.4909	5.4873	5.4853	5.4789	5.4758
	Cell Volume	347.51	347.331	346.586	346.317	345.462	344.516
	χ^2	4.3	5.59	3.28	3.79	3.54	2.82
300K	$\mu_{FM, Mn}(\mu_\beta)$	2.13 (.04)	1.71 (.05)	0.40 (.13)	*n/a*	1.08 (.08)	*n/a*
	$\mu_{AFM, Mn}(\mu_\beta)$	*n/a*	*n/a*	*n/a*	*n/a*	0.22 (.10)	0.28 (.07)
	a(rhomb)	5.498	5.499	5.494	5.491	5.486	5.4849
	Cell Volume	349.485	349.353	348.366	347.943	347.104	346.871
	χ^2	3.52	5.05	4.83	3.62	3.25	2.37

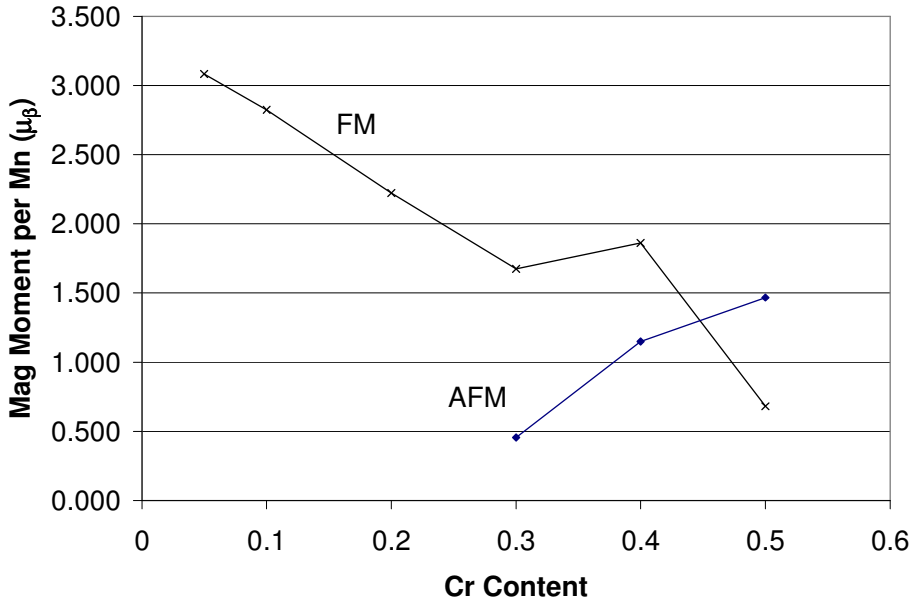

Figure 2-2 Refined Ferromagnetic and Antiferromagnetic moments on Mn occupation site versus Cr content at 12K. The magnetic moments are calculated on the Mn atom occupational sites and represent magnetic moments per Mn site within the cell structure.

Our refinements are consistent with a model comprised of separate FM and AFM ordered domains. Figure 2-3 is a plot of peak width as a function of scattering angle at 12K. The peak widths are significantly greater for the x=0.40 sample. An almost identical behavior is found for the room temperature peak widths. One possible interpretation of the peak broadening is the coexistence of magnetically ordered FM and

AFM domains as previously observed in bi-layered LaSrMnO-based manganites [15, 16]. Another possible explanation is the peak broadening could be indicating much smaller sizes of the FM and AFM domains.

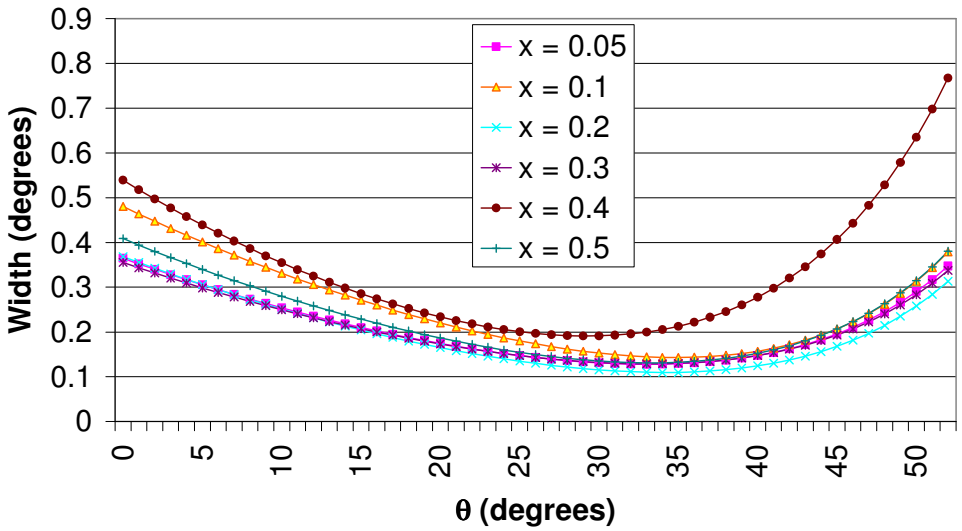

Figure 2-3 Peak width $(U*\tan^2(\theta)+V*\tan(\theta) + W)^{1/2}$ versus θ (half the scattering angle) for $La_{0.7}Sr_{0.3}Mn_{1-x}Cr_xO_3$.

The unit cell volume and a_{rhomb} decrease with increasing Cr content as shown in Figure 2-4, and follow the same trend as found by Kallel et al. [7]. However, our a_{rhomb} values are slightly higher and decrease more slowly with Cr content. This could be due to our sintering process being carried out at a lower temperature; Wollan et al. [2] find a direct link between firing temperature and quantity of Mn^{4+} ions. The unit cell volumes for 12K and 300K show similar behavior, except between x=0.4 to x=0.5, where a slight divergence is observed.

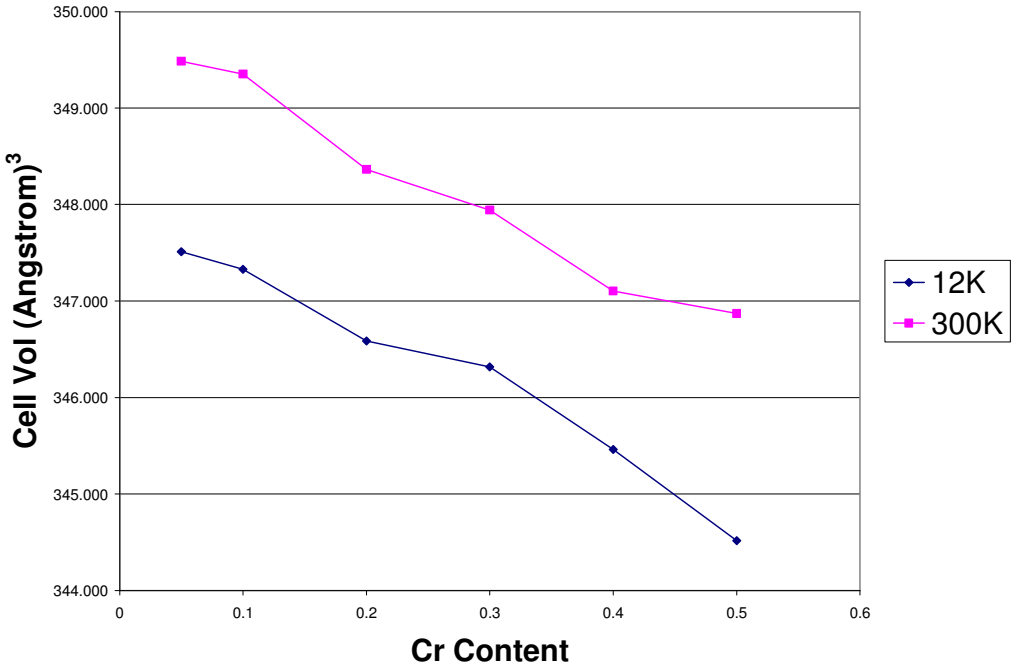

Figure 2-4 Crystal cell volume versus Chromium content for 12K and 300K. Cell volume decreases with increased Chromium content.

Our magnetic measurements show FM behavior at all temperatures for $x \leq 0.20$ and a reduction in Curie temperature with increasing Cr content for all samples (Figure 2-5). For $x \geq 0.3$, samples initially order in a FM configuration, but with decreasing temperature, a peak in the magnetization is observed, suggestive of a FM-AFM

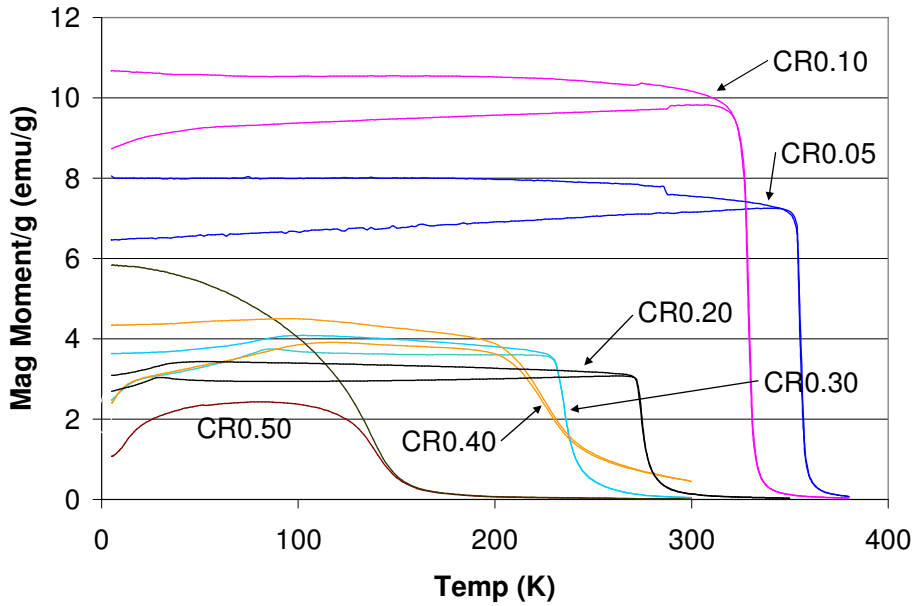

Figure 2-5 Magnetic moment (zero-field-cooled) versus temperature for $La_{0.7}Sr_{0.3}Mn_{1-x}Cr_xO_3$. T_C decreases as doping concentration of chromium is increased.

transition. This is seen in Figure 2-6, which also illustrates the onset temperature of the AFM transition that increases with increasing Cr content and narrows the existence range of the purely FM phase. When combined with the neutron data, indications are the pure

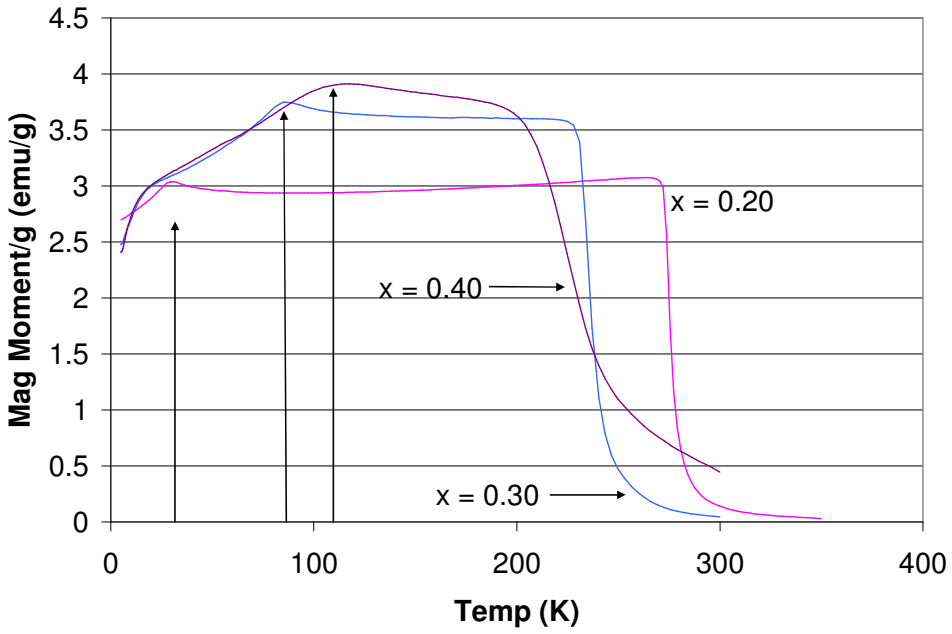

Figure 2-6 Zero-field-cooled magnetization versus temperature for $La_{0.7}Sr_{0.3}Mn_{1-x}Cr_xO_3$. The arrows point to onsets of AFM behavior.

FM phase only exists for x<0.30. For x = 0.50, magnetic measurements indicate the FM phase may exist only over a very narrow temperature range while the neutron data indicate the FM moment is less than 25% of the initial value of $3.04\mu_B$ for x=0.05.

2.5 SUMMARY

We have studied the structural and magnetic properties of $La_{0.7}Sr_{0.3}Mn_{1-x}Cr_xO_3$. All samples were of single phase with a rhombohedral structure (space group $R\bar{3}c$). We have presented evidence for coexisting FM and AFM domains and complex magnetic behavior. The unit cell volume and arhomb decrease with increasing Cr content. There was significant peak broadening for x=0.4, possibly indicating coexisting FM and AFM phases or smaller FM and AFM phases or both. While magnetization measurements may leave some ambiguity about the nature of the low temperature state, the neutron

diffraction data clearly show ferromagnetism and antiferromagnetism co-exist over a significant composition range. Since we find only a single crystallographic phase, it appears likely the two magnetic phases arise from introduction of charge separation in a chemically homogeneous matrix.

2.6 REFERENCES

1. Jonker, G. H. and Van Santen, J. H., Physica, vol. 16, pp. 337-349, 1950.
2. Wollan, E. O., Koehler, W. C., Phys. Rev., vol. 100, pp 545-563, 1955.
3. Goodenough J. B., Magnetism and the Chemical Bond. (Huntington: Krieger, 1976.
4. Tofield, B. C. and Scott, W. R., Journal of Solid State Chem., vol. 10, pp 183-194, 1974.
5. Zener, C., Phys. Rev., vol. 82, pp403-405, 1951.
6. Martin, M., Shirane, G., Endoh, Y., Hirota, K., Moritomo, Y., Tokura, Phys. Rev., vol. 53; no.21, pp. 14285-14290, 1996.
7. Kallel, N., Dhahri J,., Zemni, S., Oumezzine M., Ghedira, M., and Vincent, H., Phys. Status Solidi, vol. 184, no. 2, pp. 319-325, 2001
8. Oishi, M., Yashiro, K., Sato, K, Mizusaki, J.,and Kawada, T., Journal of Solid State Chem., vol. 181, pp 3177-3184, 2008.
9. Plint, S. M., Connor, P. A., Tao, S., Irvine, and J. T. S., Solid State Ionics, vol. 177, pp2005-2008, 2006.
10. Yanchevskii, O. Z. , Belous, A. G. , Tovstolytkin, A. I., V'yunov, O. I., and Durilin, D. A. , Inorganic Materials, vol. 42. no. 10. pp. 1121-1125, 2006.

11. Sun, Y., Tong, W., Xu, X, and Zhang, Y., Appl. Phys. Lett, vol. 78, no. 5, pp.643-645, 2001.

12. Li, W., Zhang, B., Lu, W., Sun, Y., and Zhang Y., J of Phys. And Chem. Of Solids, vol. 68 pp1749-1755, 2007.

13. Millis, A. J., Littlewood, P. B. , and Shraiman, B. I., Phys. Rev. Lett., vol. 74, no. 25, pp. 5144-5147, 1995.

14. J. Rodriguez-Carvajal, FULLPROF 2K, Version 3.00, Laboratoire Leon Brillouin-JRC, 2004

15. Kubota, M., Fujioka, H., Ohoyama, K., Hirota, K., Moritomo, Y., Yoshizawa, and H., Endoh, Y., J. Phys. Chem. Solids vol. 60, pp. 1161, 1999

16. Perring, T.G., Aeppli, G., Moritomo, Y., and Tokura, Y., Phys. Rev. Lett., vol. 78, no. 16, pp. 3197-3200, 1997.

3. STRUCTURAL AND MAGNETIC PROPERTIES OF $La_{0.7}Sr_{0.3}Mn_{1-x}Ni_xO_3$ (x=0.05, 0.1, 0.2, 0.3, 0.4)

Thomas F. Creel,[1] Jinbo B. Yang,[2] Mehmet Kahveci,[3] Jagat Lamsal,[3] Satish K. Malik,[4] S. Quezado,[4] B. W. Benapfl,[5] H. Blackstead,[5] O. A. Pringle,[1] William B. Yelon,[6] William J. James[6]

[1]Department of Physics, Missouri University of Science and Technology, Rolla, MO, U.S.A.

[2]State Key Laboratory for Artificial Microstructure and Mesoscopic Physics and School of Physics, Peking University, Beijing

[3] Department of Physics, University of Missouri, Columbia, MO, U.S.A

[4]Departamento de Física Teórica e Experimental, UFRN, 59072-970 NATAL- RN, Brazil

[5]Department of Physics, University of Notre Dame, IN, U.S.A.

[6]Center for Materials Science Research, Missouri University of Science and Technology, Rolla, MO, U.S.A.

3.1 ABSTRACT

We have studied the structural and magnetic properties of La0.7Sr0.3Mn1-xNixO3 (x=0.05, 0.10, 0.20, 0.30, and 0.40) perovskites using x-ray and neutron diffraction and magnetic measurements. To our knowledge, there exists no neutron diffraction data available for this group of perovskite compositions. Neutron (λ = 1.479Å) and x-ray (λ = 1.5481Å; Cu Kα) powder diffraction indicate that for x≥0.1 all samples are two-phase with a rhombohedral perovskite structure (space group$R\bar{3}c$) and a small amount of NiO (space group Fm3m). Neutron diffraction data for the perovskite phase at 12K and 300K show ferromagnetic ordering for x ≤ 0.2 and antiferromagnetic

ordering for x = 0.4. However, for x = 0.3, neutron diffraction data at 12K show coexisting ferromagnetic and antiferromagnetic ordering while at 300K no magnetic ordering is found. Magnetic measurements indicate that the Curie temperature decreases with increasing Ni content. The NiO phase for all samples was found to have antiferromagnetic ordering at 12K and 300K. The magnetic measurements are consistent with the neutron diffraction data and together indicate long-range magnetic ordering for samples at low temperature and transitions from ferromagnetic to paramagnetic to antiferromagnetic ordering for samples at room temperature.

3.2 INTRODUCTION

There continues to be significant interest in the magnetic and electronic transport properties of manganese-based perovskite materials. In the earliest studies, complex ferromagnetic (FM) and antiferromagnetic (AFM) phases were found to exist, and more recently, colossal magnetoresistance and interesting magnetotransport properties have been discovered [1, 2, 3]. These mixed-valence perovskites have a myriad of applications that include cathodes for solid oxide fuel cells, catalysis and giant magneto-resistance materials [4, 5, 6]. The magnetic and transport properties of these manganites have been described using the double exchange mechanism of Mn^{3+}-O-Mn^{4+}, distorted perovskite structures caused by different ion sizes and electron-phonon coupling due to the Jahn-Teller effect of the Mn^{3+} ion [7, 8, 9, 10]. The Mn^{3+} and Mn^{4+} ions with itinerant and localized electrons in orbitals t_{2g} e_{1g}, and t_{2g} e_{0g} respectively, are described by Zener as being the primary mechanism for the double exchange interaction responsible for the layered magnetic interactions [10].

Substituting a divalent alkaline-earth metal ion, such as Sr^{2+}, on the A-site for the trivalent La^{3+} ions, creates holes and produces Mn^{4+} ions [2]. With Sr doping concentrations of about 30%, the $LaSrMnO_3$ is a FM metal for temperatures ≤ 340K, with a Curie temperature near 380K, and a magnetic moment per Mn atom of about $3.6\mu_B$ [11]. This is in good agreement with calculated values assuming complete spin alignment of magnetic moments of Mn ions, $4\mu_B$ for Mn^{3+}, with an outer electron configuration d^4 ($t^3_{2g}e^1_g$) and $3\mu_B$ for Mn^{4+}, with an outer electron configuration d^3 ($t^3_{2g}e^0_g$)) which gives $3.7\mu_B$/formula unit [12].

Electron paramagnetic resonance, XPS and X-ray absorption spectra measurements on the Ni ions in several different perovskites indicate the Ni ion is in the Ni^{2+} state ($t^6_{2g}e^2_g$) [13, 14, 15, 16]. However, Goodenough et al. [17] find the Ni ions favor Ni^{3+} in the low spin state where the magnetic moment is only $1\mu_\beta$.

In this study we examine the structural and magnetic properties of $La_{0.7}Sr_{0.3}Mn_{1-x}Ni_xO_3$ perovskites (x=0.05, 0.10, 0.20, 0.30 and 0.40) using X-ray diffraction at 300K, neutron diffraction at 12K and 300K, and magnetic measurements.

3.3 EXPERIMENTAL

Polycrystalline samples of $La_{0.7}Sr_{0.3}Mn_{1-x}Ni_xO_3$ (x=0.05, 0.10, 0.20, 0.30 and 0.40) were prepared using a conventional solid-state reaction method in air. Appropriate amounts of high purity La_2O_3, $SrCO_3$, MnO_2, and Ni_2O_3 powders were weighed and mixed according to the desired stoichiometry for each sample. The samples were ground using a high energy ball mill for 5 hours, pressed into pellets at 10,000 psi and then fired at 1350˚ C for 24 hours in air with a rapid room-air quench upon removal from the oven.

All processes were performed in air, providing an oxygen-rich environment. After 24 hours of cooling, the samples were re-ground, pressed and fired using the same process.

Neutron-diffraction data were collected at the University of Missouri Research Reactor (MURR) facility using a position sensitive detector diffractometer with a neutron wavelength of λ = 1.479Å. X-ray data were collected with an XPERT PRO diffractometer using a Cu Kα wavelength of λ = 1.5481Å. Powder diffraction data were refined using the FullProf suite of programs [18]. Magnetic measurements were performed at the University of Brasilia, Brasilia DF, Brazil using a vibrating sample magnetometer and a Quantum Design physical property measurement system with the AC magnetization option.

3.4 RESULTS AND DISCUSSION

Neutron diffraction data indicate all samples crystallize in the rhombohedral structure (space group $R\bar{3}c$). All samples except for x=0.05 indicate a small amount of NiO (space group Fm3m) that increases with increasing Ni content. The neutron diffraction data were initially refined using the perovskite $R\bar{3}c$ structure. Temperature-dependent misfits in the refinements suggested the presence of magnetic scattering while additional misfits indicated a very small amount of impurity phase. The impurity phase was fit using the NiO AFM model developed by Shull et al. [19]. The AFM phase for the NiO was fit using FM ordered sheets of Ni atoms with moments aligned along the cubic axis and stacked antiferromagnetically to the (111) plane [19].

Neither the FM nor AFM model was sufficient to fit the x=0.30 diffraction patterns at 12k for the perovskite nuclear structure. The only way to account for all

magnetic reflections was to include both FM and AFM scattering in the refinements. The coexisting magnetic scattering in the 12K neutron diffraction data for x=0.3 is illustrated in Figure 3-1. In the main figure, all phases are refined while in the insets, the AFM and FM moments are not refined. The differences between refined and model solutions are indicated by the line at the bottom of the figure. The arrows indicate the reflections that contain magnetic intensity. The peak labeled AFM can be fit only by including the layered AFM structure, and the peak labeled "FM+Nuclear" can be best fit only by including the FM structure. It was found that the AFM peak could be fit with an A-type [3] layered AFM structure for the perovskite phase using FM moments on the manganese atoms parallel within the basal plane but antiparallel between planes. For x=0.4, we find AFM moments for the perovskite structure at 12K and 300K. We previously reported similar behavior in our studies on $La_{0.7}Sry0.3Mn_{1-x}Cr_xO_3$ [20]. Our refinements are consistent with a model comprised of separate FM and AFM ordered phases.

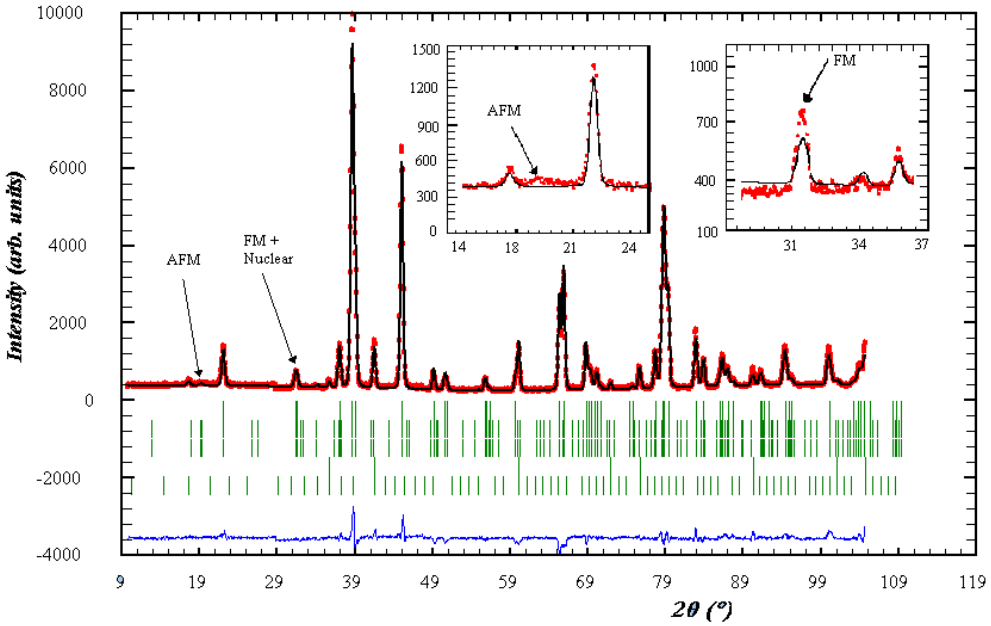

Figure 3-1 Neutron-diffraction refinement of $La_{0.7}Sr_{0.3}Mn_{0.7}Ni_{0.3}O_3$ sample. The reflection markers below the plot are, in order, nuclear perovskite structure, FM followed by AFM for the perovskite structure, Ni nuclear structure and AFM on the Ni structure. Arrows indicate the AFM and FM peaks. The insets show the regions around the small FM and AFM peaks.

The peak widths increase with increased Ni content at 12K and 300K. Similar behavior was found in our earlier work with $La_{0.7}Sr_{0.3}Mn_{1-x}Cr_xO_3$ [20]. Possible interpretations of the peak broadening include smaller grain sizes [21] but more likely is due to the coexistence of magnetically ordered FM and AFM domains as previously observed by Wollan et al. [2] using neutron diffraction studies of bi-layered $LaCaMnO_3$. Sun et al. [22] and Wang et al. [13] have previously interpreted the separation between zero field-cooled and field-cooled magnetic measurements in Cr and Ni-doped $La_{0.67}Sr_{0.33}MnO_3$ to indicate FM and AFM competition as cluster glass behavior. However, our neutron data confirm the presence of long range magnetic order as opposed to the short range order in cluster glass.

The results of our neutron diffraction refinements are presented in Table 3-1. The samples with x=0.05, 0.10, and 0.20 are FM at both 12K and 300K with the magnetic scattering at 300K for x=0.20 extremely weak. According to Kramer's super exchange rules [23, 24, 25], there are likely Ni^{3+}-O-Mn^{4+} super exchange interactions that increase with increased Ni content. XPS measurements are planned for future work. AFM scattering is first observed for x=0.30 at 12K but is not observable at 300K. However, AFM moments are observable for x=0.4 at 12K and 300K.

Table 3-1 Refined parameters: magnetic moment (μ_B), a, c, volume and χ^2 versus Ni content from neutron-diffraction refinements. The magnetic moments are calculated on the Mn atom occupational sites and represent magnetic moments per Mn site within the cell structure.

Ni Content		0.05	0.10	0.20	0.30	0.40
12K	$\mu_{FM, Mn}(\mu_B)$	3.34 (0.03)	3.14 (0.04)	2.96 (0.04)	1.97 (0.03)	*n/a*
	$\mu_{AFM, Mn}(\mu_B)$	*n/a*	*n/a*	*n/a*	0.53 (0.05)	1.13 (0.03)
	a	5.49	5.49	5.48	5.48	5.47
	c	13.31	13.30	13.29	13.29	13.29
	Cell Volume	347.96 (0.01)	347.37 (0.01)	345.88 (0.01)	344.81 (0.02)	342.75 (0.02)
	χ^2	3.37	3.38	2.26	3.54	3.37
300K	$\mu_{FM, Mn}(\mu_B)$	1.93 (0.03)	1.18 (0.04)	0.38 (.12)	*n/a*	*n/a*
	$\mu_{AFM, Mn}(\mu_B)$	*n/a*	*n/a*	*n/a*	*n/a*	0.62 (.06)
	a	5.50	5.50	5.49	5.48	5.47
	c	13.35	13.34	13.32	13.31	13.29
	Cell Volume	349.78 (0.02)	349.40 (.01)	347.74 (.02)	346.49 (.02)	344.69 (.03)
	χ^2	2.82	5.05	4.83	3.62	3.25

The unit cell volume and the lattice parameters decrease with increasing Ni content, and follow the same trend as found by Wang et al. [14] and Kuharuangrong et al. [21]. The Ni ion can exist in the Ni^{2+}, Ni^{3+} low spin, Ni^{3+} high spin, and Ni^{4+} states with radii of 0.69 Å, 0.56 Å, 0.60 Å, 0.48 Å. It is already well known that the Mn ions are likely to be in the Mn^{3+} low spin and Mn^{4+} states [2] with radii of 0.58 Å and 0.53 Å respectively. Our lattice parameters and magnetic refinements are consistent with the work of Goodenough et al. [17] and Sanchez et al. [26] where it is shown that the Ni ion prefers the Ni^{3+} low spin state in our doping ratios. It should be noted that our refined

stoichiometric values for the 30% doped sample indicates only 22% of the Ni goes into the perovskite structure, contributing to the lower than expected refined magnetic moment of 2.8μ_B/formula unit.

Magnetic measurements indicate that T_C decreases with increasing Ni doping and a temperature dependent FM to paramagnetic (PM) transition occurs for all Ni concentrations as observed in Figure 3-2 and confirmed by our colleagues at the University of Notre Dame. Our measured FM to PM transitions and magnetic moments are in good agreement with those of Hu et al. [27] and Wang et al. [13].

Our magnetic measurements also show FM behavior at all temperatures for $x \leq 0.20$ and a reduction in the Curie temperature with increasing Ni content for all samples. From x = 0.20 and 0.30, magnetic measurements show a large separation in the magnetization curves and for x=0.30 a long tail of magnetization that does not go to zero out to 300K. It is worth recalling, the neutron data for x=0.30 show coexisting FM and AFM structure for the perovskite phase. We believe the long tail is likely due to the NiO contaminant phase.

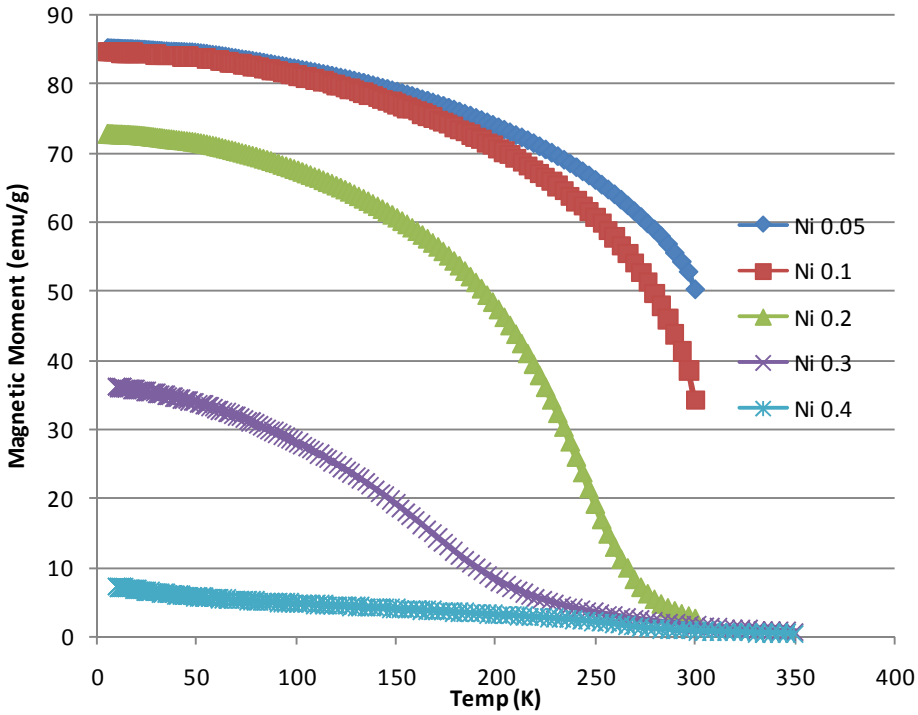

Figure 3-2 Magnetic moment versus temperature for all doping concentrations. The Curie temp (T_C) is observed to decrease with increasing Ni content.

3.5 CONCLUSIONS

We have studied the structural and magnetic properties of $La_{0.7}Sr_{0.3}Mn_{1-x}Ni_xO_3$. Neutron powder diffraction refinements indicate for x >0.05 all samples are two-phase with a rhombohedral perovskite structure (space group $R\bar{3}c$) and a small amount of NiO impurity phase (space group Fm3m) that increases with increasing Ni content. We have presented evidence for coexisting FM and AFM domains and complex magnetic behavior. The unit cell volume and lattice parameters decrease with increasing Ni content in agreement with earlier studies [6, 14, 21]. There is increasing peak broadening and a transition from FM to FM + AFM to AFM behavior with increasing Ni content. While magnetic measurements may leave some ambiguity about the nature of the low

temperature state, the neutron diffraction data clearly show that long range ferromagnetism and antiferromagnetism co-exist over a small composition range. Since we find only a single crystallographic phase, it appears likely that the two magnetic phases arise from introduction of charge separation in a chemically homogeneous matrix.

3.6 REFERENCES

1. Jonker, G. H. and Van Santen, J. H., Physica, vol. 16, 337-349, (1950).
2. Wollan, E. O., Koehler, W. C., Phys. Rev., vol. 100, 545-563, (1955)
3. Goodenough J. B., Magnetism and the Chemical Bond. (Huntington: Krieger, 1976.)
4. L. Brorovskikh, G. Mazo, E. Kemnitz, Solid State Sci, 5, 409-417 (2003)
5. R.J.H. Voorhoeve, D.W. Johnson, J.P. Remeika, P.K. Gallagher, Science 195, 827-833 (1977)
6. J.T. Vaughey, J.R. Mawdsley, T.R. Krause, Mater Res Bul, 42, 1963-1968 (2007)
7. Millis, A. J., Littlewood, P. B. , and Shraiman, B. I., Phys. Rev. Lett., v 74, (25) 5144 (1995)
8. A.J. Millis, Phys Rev. B 53, 8434 (1996)
9. W. Archiald, J.-S. Zhou, J.B. Goodenough, Phys. Rev. B 53, 14445 (1996)
10. Zener, C., Phys. Rev., vol. 82, 403-405 (1951)
11. Martin, M., Shirane, G., Endoh, Y., Hirota, K., Moritomo, Y., Tokura, Phys. Rev., 53 (21) 14285-14290 (1996)
12. T.-S. Zhao, W.X. Xianyu, B.H. Li, Z.N. Qian, J of Alloys and Comp., 459, 29-34 (2008)
13. M. Rubinstein, D.J. Gillespie, J.e. Snyder, T.M. Tritt, Phys. Rev. B 56, 5412 (1997)

14. Z. H. Wang, J.W. Cai, B.G. Shen, X. Chen, W.S. Zhan, J. Phys.:Condens. Matter 12, 601 (2000)

15. S. Pal, E. Sose, B.K. Chaudhuri, H.D. Yang, S. Neeleshwar, Y.Y. Chen, J. Magn. Magn. Mater, 293, 872 (2005)

16. O. Toulemonde, F. Suder, A. Barnabe, A. Maignan, C. Martin, B. Raveau, Eur. Phys. J. B, 4, 159 (1998)

17. Wold, R. J. Arnott, and J. B. Goodenough, J. Appl. Phys, 29, 387-389 (1958)

18. J. Rodriguez-Carvajal, FULLPROF 2K, Version 3.00, Laboratoire Leon Brillouin-JRC, 2004

19. C. G. Shull, W. A. Strauser, E. O Wollan, Phys. Rev., 83 (2) 333 (1951)

20. T . F. Creel, J.B. Yang, M. Kahveci, J. Lamsal, S. K. Malik, S. Quezado, O. A. Pringle, W. B. Yelon, W. J. James, Mag, IEEE Trans, 46 (12) 4113 (2010)

21. Sutin Kuharuangrong, Ceramics International , 30, 273 (2004)

22. Sun, Y., Tong, W., Xu, X, and Zhang, Y., Appl. Phys. Lett, 78 (5) 643-645 (2001)

23. L. Kanamori, J. Phys. Chem. Solids 10, 87 (1959)

24. J.B. Goodenough, A. Wold, R. Arnott, N. Menyuk, Phys. Rev. 124, 373 (1961)

25. H. A. Kramers, Physica 1, 182 (1934)

26. M.C. Sanchez, J. Garcia, J. Blasco, G. Subias, J. Perez-Cacho,Phys. Rev. B 65, 144409 (2002)

27. Jifan Hu, Chengjie Ji, Hongwei Qin, Juan Chen, Yanming Hao, Yangxian Li, J. of Mag. And Mag. Mat. 241, 271 (2002)

4. STRUCTURAL AND MAGNETIC PROPERTIES OF $La_{0.7}Sr_{0.3}Mn_{1-x}Cr_xO_3$ ($x \leq 0.6$)

Thomas F. Creel,[1] Jinbo Yang,[2] Mehmet Kahveci,[3] Satish K. Malik,[4] S. Quezado,[4] O. A. Pringle,[1] William B. Yelon,[5] William J. James[5]

[1]Department of Physics, Missouri University of Science and Technology, Rolla, MO, U.S.A.
[2]State Key Laboratory for Artificial Microstructure and Mesoscopic Physics and School of Physics, Peking University, Beijing
[3] Department of Physics, University of Missouri, Columbia, MO, U.S.A
[4]Departamento de Física Teórica e Experimental (DFTE), Universidade Federal do Rio Grande do Norte (UFRN), Natal, Brazil
[5]Department of Chemistry and Graduate Center for Materials Research, Missouri University of Science and Technology, Rolla, MO, U.S.A.

4.1 ABSTRACT

Structural and magnetic properties of $La_{0.7}Sr_{0.3}Mn_{1-x}Cr_xO_3$ (x=0.05, 0.1, 0.15, 0.20, 0.25, 0.30, 0.40, 0.50 and 0.60) have been studied in order to determine the magnetic and structural influence of the substitution of Cr for Mn. The data consist of neutron (λ = 1.479Å) and x-ray (λ = 1.5481Å; Cu Kα) powder diffraction and magnetization measurements. We previously suggested these systems transition from ferromagnetic to antiferromagnetic ordering with the intermediate concentrations containing coexisting ferromagnetic and antiferromagnetic domains. Upon further detailed examination, we find that the neutron data can be fit using a single,

homogeneous, long-range magnetically ordered state and compositionally-dependent charge ordering. At low Cr concentrations, the Mn^{3+}-O-Mn^{4}+ double exchange dominates. The substitution of Cr^{3+} drives the system towards an antiferromagnetic state by antiferromagnetic Cr^{3+}-O-Mn^{4+} and Cr^{3+}-O-Cr^{3+}, and ferromagnetic Cr^{3+}-O-Mn^{3+} superexchange interactions. Charge ordering at temperatures $\leq$ 100K is observed over a remarkably wide compositional range, producing a complex ferromagnetic state for $0.2<x<0.45$ and a ferrimagnetic state for $x>0.45$. The detailed behavior can be explained by a simple model describing the arrangement of the moments of the different species and by the effect of Cr^{3+} on its Mn near neighbors.

4.2 INTRODUCTION

The $LaMnO_3$ perovskites continue to be of significant interest due to the complex, temperature dependent electronic and magnetic phases they exhibit. A-site (La-site) and B-site (Mn-site) doping in these systems cause complex compositionally-dependent magnetic behavior. These perovskites are known for the unusually large effect that an external magnetic field has on their ability to transport electricity and heat [1, 2] and interesting metallic-insulating transitions associated with the ferromagnetic to paramagnetic transition [3]. Applications of these mixed-valence perovskites include cathodes for solid oxide fuel cells, magnetic storage devices, magnetoresistive read heads, catalysts, collosal magnetoresistance (CMR), and giant magnetoresistence (GMR) materials [4, 5, 6]. The underlying mechanism of the magnetic and transport properties of these manganites have been described with double exchange, super exchange,

semicovalent exchange, Jahn-Teller distortions, and electron-phonon couplings [7, 8, 9, 10, 11, 12, 14].

$LaMnO_3$ is antiferromagnetic at low temperatures with T_N~150K [15], crystallizing in the orthorhombic space group Pbnm. Oxygen stoichiometry is extremely important, influencing the Jahn-Teller distorted oxygen octahedron surrounding the d4 Mn^{3+} cation [16].

Substituting divalent Sr^{2+} for the trivalent La^{3+} creates d-electron holes by oxidizing Mn^{3+} to Mn^{4+} as can be described by the formula $La^{3+}_{1-x}Sr^{2+}_{x}\left(Mn^{4+}_{x}Mn^{3+}_{1-x}\right)O^{2-}_{3}$. The Curie temperature has been directly linked to the amount of Mn^{4+} present and can result in temperature-dependent ferromagnetic and antiferromagnetic couplings [17]. Martin and Shirane [18] found $La_{0.7}Sr_{0.3}MnO_3$ to be a ferromagnetic metal with T_C ~ 378K and a magnetic moment per Mn of about 3.6 μ_B. This is in good agreement with the calculated value of 3.7μ_B/fu assuming complete spin alignment of the magnetic moments of the Mn ions, 4μ_B for Mn^{3+} and 3μ_B for Mn^{4+} [15].

Previous studies substituting Cr on the B-site while substituting Sr^{2+} for La^{3+} on the A-site found the Cr ion to be Cr^{3+}, leading to $La^{3+}_{1-x}Sr^{2+}_{x}Mn^{4+}_{x}\left(Cr^{3+}_{y}Mn^{3+}_{1-x-y}\right)O^{2-}_{3}$ [19, 20, 21, 22]. X-ray diffraction, magnetic and magnetoresistance measurements indicate that T_C and the lattice parameter a decrease with increasing Cr content [22, 23]. Concentrations of Cr<20% exhibit temperature-dependent metal to semiconductor transitions, whereas concentrations of Cr≥20% result in insulating behavior [23, 24]. The large separation in magnetization between field-cooled (M_{FC}) and zero field-cooled (M_{ZFC}) magnetic measurements at low temperature have been ascribed to ferromagnetic and antiferromagnetic clusters or spin or cluster glass [25, 26]. The substitution of Cr^{3+}

results in antiferromagnetic Cr^{3+}-O^{2-}-Cr^{3+} and Cr^{3+}-O^{2-}-Mn^{4+} interactions and ferromagnetic Cr^{3+}-O^{2-}-Mn^{3+} interactions as predicted by superexchange rules [20, 27]. However, there remains some controversy as to the alignment between the ferromagnetically aligned Mn^{3+} ($4\mu_B$) and Mn^{4+} ($3\mu_B$) with Cr^{3+} ($3\mu_B$). For concentrations between 20% and 60%, magnetic order has been interpreted by others as coexisting inhomogeneous ferromagnetic and antiferromagnetic domains and spin glass [19, 20, 23, 26, 28, 29].

In this study, Mn is replaced in $La_{0.7}^{3+}Sr_{0.3}^{2+}Mn_{0.3}^{4+}\left(Cr_y^{3+}Mn_{0.7-y}^{3+}\right)O_3^{2-}$ with up to 60% Cr. Neutron diffraction, X-ray diffraction and magnetic measurements are used to study the nuclear and magnetic structure and magnetic properties of the Cr-substituted perovskite. Cr^{3+} is electronically the same as Mn^{4+} but has an ionic radius (0.615Å) slightly smaller than that of Mn^{3+} (0.656Å) [30]. Therefore the unit cell parameters are expected to decrease with increasing Cr^{3+} content.

4.3 EXPERIMENTAL

Polycrystalline samples of $(0<x<0.6)$ were prepared by a conventional solid state reaction method in air. Appropriate amounts of high purity La_2O_3, $SrCO_3$, MnO_2, and Cr_2O_3 powders were weighed and mixed according to the desired stoichiometry for each sample. The samples were ground using a high energy ball mill for 5 hours, pressed into pellets at 10,000 psi and then fired at 1350C for 24 hours in air with a room-air quench upon removal from the oven. After 24 hours of cooling, the samples were re-ground, pressed and fired using the same process.

Neutron-diffraction data were collected at 12K and 300K at the University of Missouri Research Reactor (MURR) facility using a position sensitive detector diffractometer with a neutron wavelength of λ = 1.479Å. X-ray diffraction data were collected with an XPERT PRO diffractometer using a Cu Kα wavelength of λ = 1.5481Å. Powder diffraction data were refined using the FullProf suite of programs [31]. Magnetic measurements were performed at the University of Brasilia, Brasilia DF, Brazil using a vibrating sample magnetometer and a Quantum Design Physical Property Measurement System with the AC magnetization option.

4.4 RESULTS AND DISCUSSION

4.4.1 Neutron Diffraction Studies

The refined neutron data are presented in Table 4-1. The nominal and refined Cr contents for the ten samples as well as the concentration of the impurity phase $MnCr_2O_4$ are provided. The chromium and $MnCr_2O_4$ percentages are based upon the total intensity of the scattered neutrons. For the remainder of this discussion, we will refer to the refined stoichiometries. The lattice parameters decrease with increasing Cr content while the oxygen stoichiometry remains constant within one-sigma error estimates except for the x=0.411 sample where the oxygen content is lower than in the other samples. At x=0.411, the Mn^{3+} and Mn^{4+} contents are approximately equal. The refined magnetic moments are presented as $\mu_{B\text{-}1}$ and $\mu_{B\text{-}2}$, referring to the observed average magnetic moments in each layer of a doubled unit cell. For x<0.194, the samples are ferromagnets with magnetic moments that decrease with increasing Cr content. Figure 4-1 shows the

neutron scattering (red dots) and refined neutron scattering (black line fit to red dots) for the combined nuclear and magnetic

Table 4-1 Refined parameters: magnetic moment (μ_B), a, c, volume, χ^2, and contaminant ($MnCr_2O_4$) phase versus nominal and refined Cr content. The magnetic moments are calculated on the Mn atom occupational sites and represent magnetic moments per Mn site within the cell structure. The numbers in parentheses represent a 1-σ fit error in the last digit. Columns labeled $\mu_{B\text{-}1}$ and $\mu_{B\text{-}2}$ are magnetic moments for each layer of the doubled unit cell.

	Nominal Cr Content (%)	Refined Cr Content (%)	$MnCr_2O_4$ Content (%)	$\mu_{B\text{-}1,\,Mn}(\mu_\beta)$	$\mu_{B\text{-}2,\,Mn}(\mu_\beta)$	a(Å)	c(Å)	Cell Volume $(Å)^3$	χ^2	O^{-2} Stoich
12K	5	4.2	1.6	3.13 (3)	3.13 (3)	5.491 (0)	13.311 (0)	347.53 (2)	3.31	3.1 (1)
	10	6.2	1.2	2.95 (4)	2.95 (4)	5.491 (0)	13.302 (0)	347.34 (2)	5.47	3.1 (1)
	15	14.3	1.5	2.48 (4)	2.48 (4)	5.491 (0)	13.305 (0)	347.33 (2)	3.11	3.0 (0)
	20	19.4	1.2	1.99 (7)	2.55 (8)	5.487 (0)	13.291 (0)	346.59 (1)	2.99	3.1 (1)
	25	22.1	1.6	1.8 (1)	2.3 (1)	5.486 (0)	13.291 (0)	346.34 (2)	3.75	3.0 (0)
	30	29.4	2.2	1.29 (5)	2.24 (6)	5.485 (0)	13.290 (0)	346.31 (2)	3.00	3.1 (1)
	30	36.5	2.7	0.53 (6)	2.63 (7)	5.480 (0)	13.286 (0)	345.50 (2)	2.63	3.1 (1)
	40	41.1	2.3	0.60 (6)	2.79 (7)	5.479 (0)	13.288 (0)	345.41 (2)	3.11	2.9 (1)
	50	48.5	2.4	- 0.8 (1)	2.1 (1)	5.476 (0)	13.267 (0)	344.50 (1)	2.30	3.0 (0)
	60	57.9	3.6	-1.7 (3)	2.2 (3)	5.470 (0)	13.264 (0)	343.62 (2)	3.80	2.9 (1)
300K	5	4.8	1.6	2.16 (3)	2.16 (3)	5.498 (0)	13.349 (0)	349.50 (2)	2.85	3.1 (1)
	10	6.2	1.2	1.65 (4)	1.65 (4)	5.499 (0)	13.342 (0)	349.35 (2)	4.58	3.1 (1)
	15	14.3	1.5	0.64 (7)	0.64 (7)	5.497 (0)	13.339 (0)	349.03 (2)	2.86	3.0 (0)
	20	19.4	1.2	0.5 (1)	0.4 (1)	5.494 (0)	13.327 (0)	348.37 (2)	4.68	3.1 (1)
	25	22.1	1.6	0.00	0.00	5.494 (0)	13.332 (0)	348.46 (2)	2.88	3.1 (1)
	30	29.4	2.2	0.00	0.00	5.491 (0)	13.326 (0)	347.94 (2)	2.57	3.1 (1)
	30	36.5	2.7	0.00	0.00	5.487 (0)	13.325 (0)	347.38 (2)	2.65	3.0 (0)
	40	41.1	2.3	0.00	0.00	5.486 (0)	13.318 (0)	347.07 (2)	3.05	2.8 (1)
	50	48.5	2.4	0.00	0.00	5.485 (0)	13.314 (0)	346.87 (1)	2.09	3.1 (1)
	60	57.9	3.6	0.00	0.00	5.477 (0)	13.305 (1)	345.68 (2)	3.22	2.9 (1)

phases for the $La_{0.7}Sr_{0.3}Mn_{0.952}Cr_{0.048}O_3$ sample. The insets in Figure 4-1 show the observed and fitted data obtained with the best nuclear-only model (right) in which the misfits highlight the magnetic contributions that are fit with the best nuclear and magnetic models (left). This refinement is typical of the refinements for x<0.194. The small peaks at ~17˚ and 35˚ are due to the presence of the $MnCr_2O_4$ impurity phase.

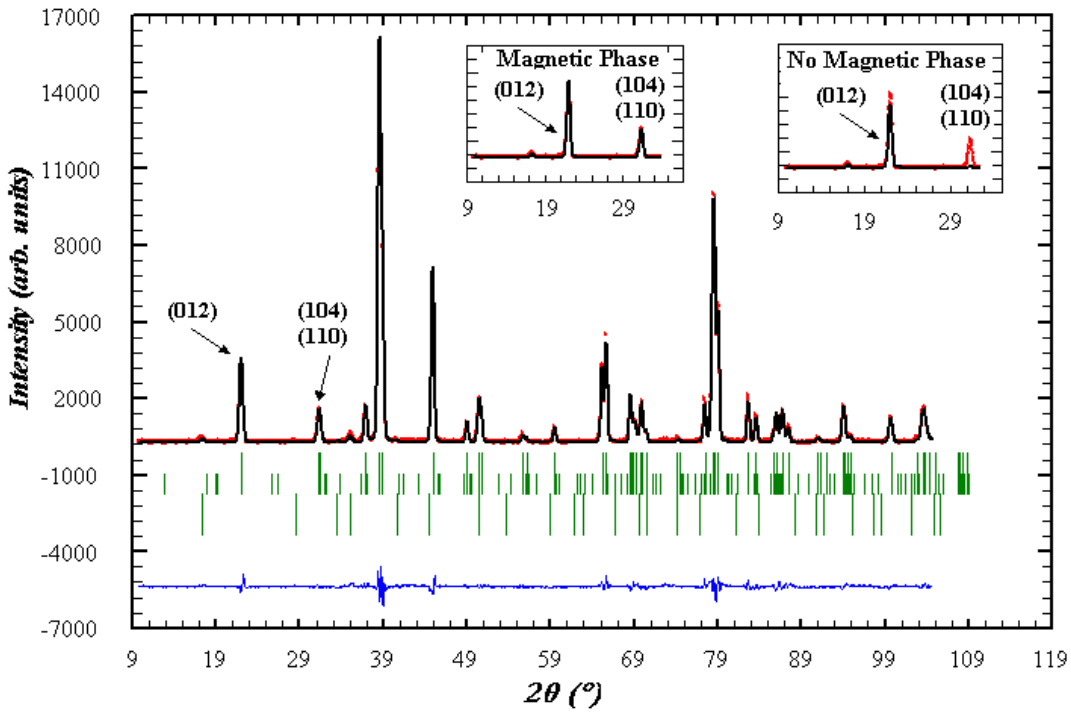

Figure 4-1 Neutron-diffraction refinement of the $La_{0.7}Sr_{0.3}Mn_{0.952}Cr_{0.048}O_3$ sample at 12K. The reflection markers below the plot are, in order, nuclear perovskite structure and ferromagnetic perovskite structure. The small peak intensities at ~17˚ and 35˚ are due to the $MnCr_2O_4$ phase. The insets show the magnified regions around the (102) and the (104) + (110) reflections prior to the addition of the magnetic phase (right) and after the magnetic phase (left) was added.

At 12K for $0.194 \leq x \leq 0.411$, we find the samples to be ferromagnets. However, while the ferromagnetic intensities from the (104) + (110) reflections are still dominant, we find the emergence of intensity in two peaks that are not visible at high temperature and are inconsistent with a simple ferromagnetic solution. These new peaks consist of one that has magnetic intensity only, the (003) + (011) reflections, and one that has nuclear and magnetic intensity, the (113) reflection. Both of these peaks can be fit by doubling the unit cell along the c-axis and allowing unequal moments on the B1 and B2 sites.

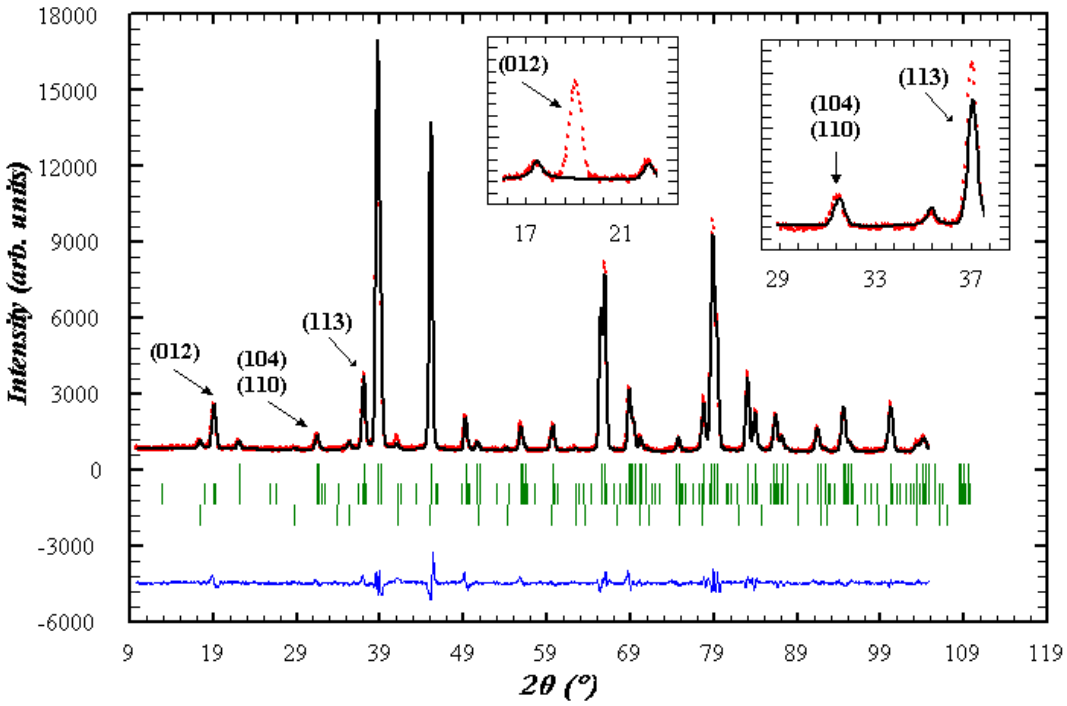

Figure 4-2 Neutron-diffraction refinement of the $La_{0.7}Sr_{0.3}Mn_{0.421}Cr_{0.579}O_3$ sample at 12K. The Bragg reflection markers below the plot are, in order, nuclear perovskite structure, magnetic perovskite structure, $MnCr_2O_4$ nuclear structure and AFM $MnCr_2O_4$ structure. The insets show the magnified regions around the two magnetic peaks prior to the addition of the magnetic phase.

At 12K, for $x \geq 0.485$ the magnetic peaks corresponding to the doubled unit cell along the c-axis, are now dominant whereas the ferromagnetic intensity from the (104) + (110) reflections is very weak (Figure 4-3c). Using the same refinement technique as for the lower Cr-content samples, we find different moments in the B1 and B2 layers with antiparallel alignment. Figure 2 shows the neutron scattering and refined neutron scattering solution for the $La_{0.7}Sr_{0.3}Mn_{0.421}Cr_{0.579}O_3$ sample that contains the new low-angle peaks observed in the x=0.411 and x=0.579 samples. The insets in Figure 4-2 show the observed and fitted data using the best nuclear-only model while the misfits highlight the magnetic contributions that are fit in the main graphic. The magnetic ordering had previously been fit with independent coexisting ferromagnetic and

antiferromagnetic phases [32]. However, we now have been able to fit all the magnetic peak intensities with one magnetic phase. Since the Mn and Cr concentrations on all B sites are equal, the refined unequal moments for this sample must arise through charge ordering, which creates higher and lower Mn^{4+} concentrations on the different layers.

At 300K, for $0.048 \leq x \leq 0.194$, we find ferromagnetic ordering that decreases with increasing Cr content, the average magnetic moments on the B1 and B2 sites being identical. Figure 4-3 shows a comparison of the low-angle neutron refinements depicting the refined neutron scattering for three samples, x=0.048, 0.411, and 0.579. The growth of the (003)+(011) reflection and the associated decrease of the (104)+(110) reflections with increasing Cr is easily seen.

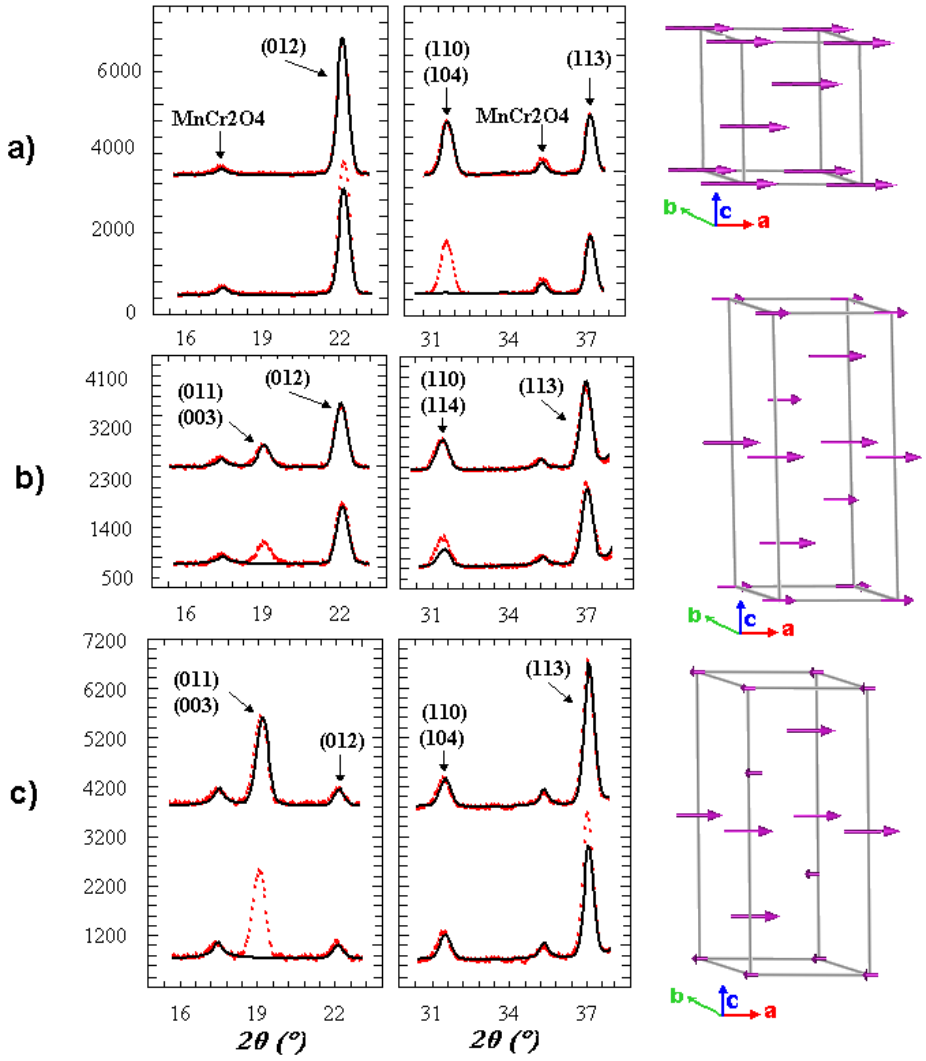

Figure 4-3 Neutron-diffraction data for the (top) $La_{0.7}Sr_{0.3}Mn_{0.942}Cr_{0.048}O_3$, (middle) $La_{0.7}Sr_{0.3}Mn_{0.589}Cr_{0.411}O_3$, and (bottom) $La_{0.7}Sr_{0.3}Mn_{0.421}Cr_{0.579}O_3$ samples. Each data graphic contains two plots, one with the nuclear and magnetic phase refined and one with only the nuclear phase solved, offset by 2000 units (top and middle) and 3000 units (bottom). The respective magnetic unit cells are to the right of each.

Figure 4-4 shows the neutron scattering data at 300K subtracted from data collected at 12K. The 300K-12K difference curve allows the elimination of all effects that are not temperature dependent. The large positive and negative swings for the (202), (006) and (024) reflections are due to temperature-driven shifts in peak positions. Significant reductions in the ferromagnetic intensities of the (110) and (104) reflections

are observed in all samples with increasing Cr content. The two new magnetic peaks, (113) and (003) + (011), are barely visible below x=0.365. Peak broadening is observed in all peaks for x=0.194, near the metal-to-insulator transition previously observed [23]. All other peaks within the remaining samples appear sharp and consistent with long range magnetic order. The peaks not annotated are associated with the $MnCr_2O_4$ contaminant phase.

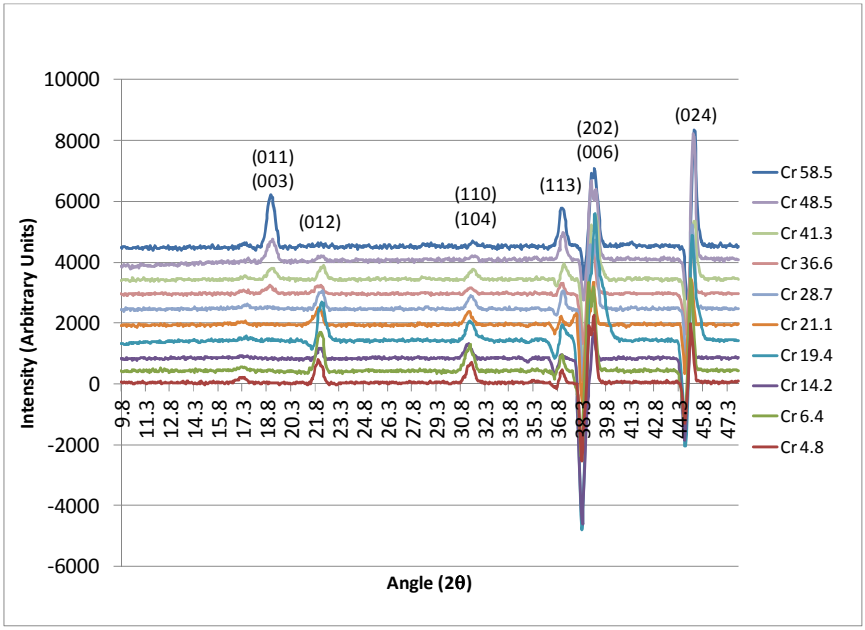

Figure 4-4 Intensity versus scattering angle of neutron scattering data collected at 300K subtracted from data collected at 12K for all Cr substituted concentrations. Successive concentrations are offset by 200 counts.

4.4.2 Magnetization Studies

Zero field-cooled (M_{ZFC}) and field-cooled (M_{FC}) magnetization measurements (Figure 4-5) indicate that T_C decreases with increasing Cr content. The T_C's and the

magnetic moments are in good agreement with those of Zhe et al [28] and Kallel et al. [23] for x<0.485. However, Kallel et al. [23] find a much higher T_C (~50K) for their x=0.50 sample than we find for the x=0.485 sample. This difference may be due to sample preparation or Cr content (ours is refined). When the samples are cooled in a zero-field environment and subsequently warmed to temperatures above T_C at an applied field of 100 Oe, all samples exhibit sharp antiferromagnetic-like transitions below T_C. Upon cooling in the same applied field, all samples exhibit softened transitions over larger temperature spans, at slightly higher temperatures, and larger magnetic moments per Mn site. These antiferromagnetic-like transitions occur at successively higher temperatures with increasing Cr content; 16.9°, 25.8°, 54.4°, 85.1° and 115.4° for x=0.142, 0.194, 0.211, 0.287 and 0.413 respectively. These antiferromagnetic-like features are very sensitive to small applied fields and temperatures. The x=0.064 sample exhibits the largest magnetic moments. The x=0.064 and x=0.048 samples exhibit a small discontinuity in the M_{FC} curves near 272K and 287K, respectively, while the x=0.064 sample exhibits the same discontinuity in the M_{ZFC} curve at 287K. Similar behavior was observed by Sun et al. [25]. There is a significant separation in magnetic moments between the x = 0.142 to x=0.211 M_{ZFC} and M_{FC} curves, possibly indicating a metal to insulator transition as observed by Kallel et al. [23]. The M_{ZFC} and M_{FC} curves for x=0.413 exhibit a broad ferromagnetic to paramagnetic transition with no clear T_C and a long tail of magnetization that does not go to zero out past 300K. At this Cr concentration, the amounts of Mn^{3+} and Mn^{4+} are approximately equal. The M_{ZFC} and M_{FC} curves for x=0.485 indicate a significant change in magnetic behavior with the

largest difference in magnetization between the M_{ZFC} and M_{FC} curves and a significantly lower T_C.

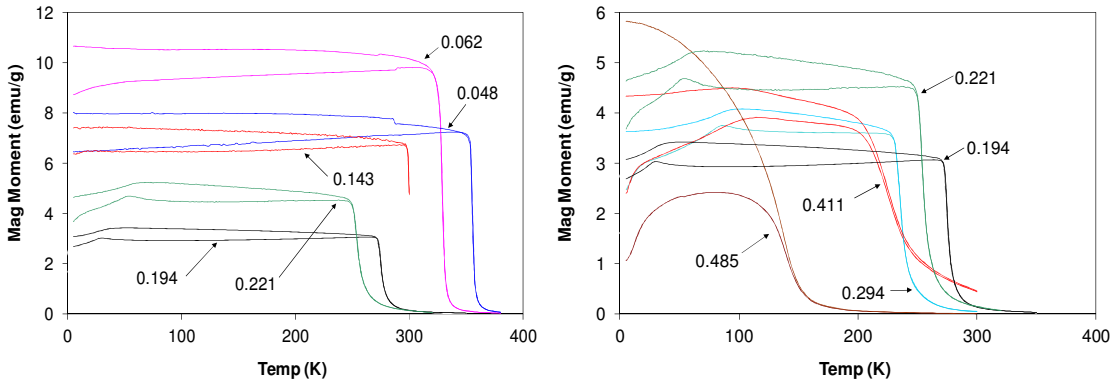

Figure 4-5 100 Oe zero field cooled (M_{ZFC}) and field cooled (M_{FC}) measurements of magnetic moments vs temperature for all nickel concentrations. The 0.194 and 0.211 are common to both for reference purposes. The lower curve for each Cr concentration is the M_{ZFC} curve while the upper curve is the M_{FC}.

The magnetizations versus magnetic field curves at 5K are plotted in Figure 4-6. For x<0.485, all samples demonstrate magnetization saturation at fields less than 25K Oe. However, for x=0.485, the system has not achieved saturation at a field greater than 75K Oe. It is at x=0.485 that a significant difference in M_{ZFC} and M_{ZFC} curves is observed along with a change in the underlying magnetic structure found from neutron refinements. The separation between x=0.143 and x=0.221 is likely witness to the onset of the metal to insulator transition [23], whereas the separation between x=0.411 and x=0.485 is attributed to the underlying layered magnetic structure switching from planes of parallel but unequal magnetic moments to planes of anti-parallel and unequal magnetic moments (ferrimagnetism).

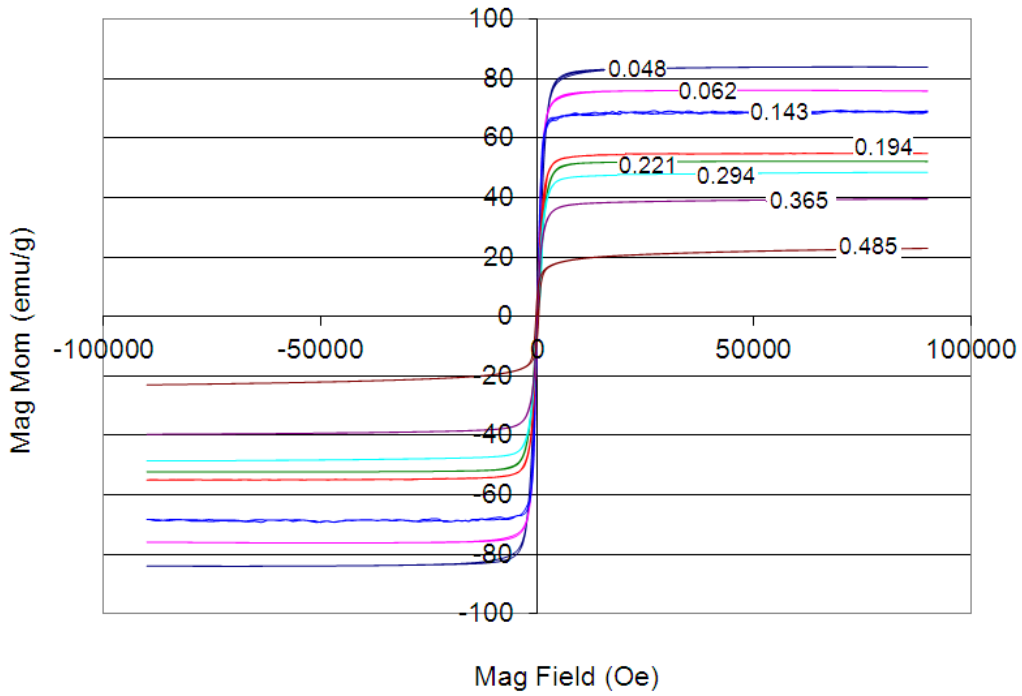

Figure 4-6 Magnetic Field vs Magnetization at 12K for all Cr concentrations.

4.4.3 Discussion

At low Cr concentrations, the results can be modeled assuming that the Cr^{3+} ions may order antiferromagnetically to the ferromagnetically ordered Mn^{3+} and Mn^{4+} ions (Figure 4-7a) as suggested by Mahendiran et al. [33] and Zhao et al. [29], and as we found in our earlier study of $La_{0.7}Sr_{0.3}Mn_{1-x}Ni_xO_3$ [34]. However, if this were the case, the net magnetic moment for the Cr substituted system would decrease with increased Cr content much more rapidly than observed. Zhe et al [28] reported that the Cr^{3+} orders ferromagnetically with Mn^{3+} near neighbors when the system is in a ferromagnetic ground state, in agreement with Kanamori-Goodenough superexchange rules (ferromagnetic Mn^{3+}-O-Cr^{3+}) [27, 35]. Without additional effects of Cr, this would lead to a pure ferromagnet with only a small compositional dependence of the net moment

loss, due to the replacement of the $4\mu_B$ Mn^{3+} by the $3\mu_B$ Cr^{3+}. To explain the observed results, we must also consider the superexchange between Cr^{3+} and Mn^{4+}, which is expected to be antiferromagnetic [1, 36]. The observed data for $x<0.194$ is fully explained assuming the spin of the Mn^{4+} ions which have one or more Cr^{3+} near neighbors will be flipped and align antiparallel to the Cr^{3+} and Mn^{3+} (Figure 4-7b). The probability

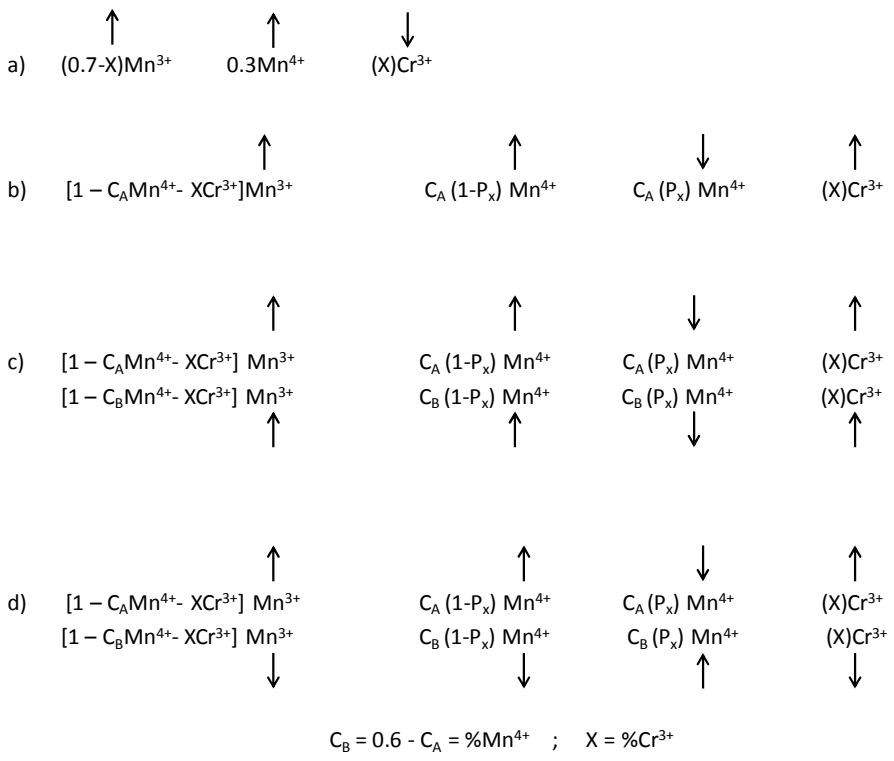

Figure 4-7 Possible magnetic ordering schemes: a) Cr^{3+} replaces Mn^{3+} but with opposite spin, b) Cr^{3+} replaces Mn^{3+} with the same spin but causes Mn^{4+} near neighbors to flip spin, c) same as b but configured in a charge order ferromagnetic-layered configuration, d) same as b but in a charge ordered antiferromagnetic-layered configuration. The "x" values represent Cr concentration.

of this occurring increases rapidly with increasing Cr content and can be calculated using the binomial theorem,

$$P(X=n)=(\frac{x!}{n!(x-n!)})p^n(q)^{(x-n)},$$

where *n=(0-6)* is the number of nearest neighbors, *x=(0-6)* is the field of nearest neighbor possibilities, *p=% Cr* and *q=(1-p),* to calculate the probability of having $0 \leq n \leq 6$ nearest Cr^{3+} neighbors on the B-site. On this basis, we find the relative strengths of the exchange interactions to be, in order; Cr^{3+}-O-Mn^{4+} antiferromagnetic superexchange, Cr^{3+}-O-Mn^{4+} superexchange and Mn^{3+}-O-Mn^{4+} double exchange interactions. The two superexchange interactions together, break the ferromagnetic alignment of the Mn^{3+} and Mn^{4+} moments.

As the Cr concentration reaches 0.194, the ordering scheme is modified by the appearance of charge ordering (at low temperature), which produces distinct B1 and B2 sites with different Mn^{3+} and Mn^{4+} concentrations. This produces different magnetic moments in the two layers and accounts for the new reflection (011) + (003). For $x \leq 0.411$, the overall interaction between these layers remains ferromagnetic (Figure 7c). In Figure 4-7b-d, P_x represents the probability that there is at least one Cr^{3+} near neighbor, while $1-P_x$ represents the probability there is no Cr^{3+} near neighbor. The proposed alignment scheme at 12K for $0.048 \leq x \leq 0.143$ is shown in Figure 4-7b, for $0.194 \leq x < 0.485$ in Figure 4-7c and for $0.485 \leq x < 0.585$ in Figure 4-7d.

To summarize, at low Cr concentration, the Cr^{3+} moment aligns parallel to the Mn^{3+} and Mn^{4+} moments, replacing Mn^{3+} in the oxygen octahedron. At this low concentration, the quantity of Cr^{3+} ions is very small and the probability is high that Cr^{3+} will have four Mn^{3+} and two Mn^{4+} neighbors. The dominance of the antiferromagnetic superexchange interaction between Cr^{3+}-O-Mn^{4+}, causes the two Mn^{4+} neighbors to flip their spin while the second strongest interaction, the ferromagnetic superexchange

between Cr^{3+}-O-Mn^{3+}, requires the moments on the Mn^{3+} neighbors to remain aligned with the Cr^{3+} moments. The random dispersion of the Cr^{3+} ions provides for a general reduction of the ferromagnetic moment observed for $x<0.194$ where the metal to insulator transition is coincident with the onset of charge ordering that is as complete as the system will allow. As the Cr concentration increases, the antiferromagnetic Cr^{3+}-O-Cr^{3+} superexchange interaction becomes increasingly important and more probable, ultimately resulting in the reversing of the orientation between the B1 and B2 layers at $x \approx 0.45$ and creating an overall antiferromagnetic stacking (Figure 4-7d). However, the charge ordering, which persists to the limit of phase stability ($x \leq 0.7$), leads to a non-zero net moment within an antiferromagnetic ordering, or ferrimagnetism. For higher temperature the charge ordering is expected to disappear creating a pure antiferromagnetic structure, but neither the neutron nor magnetization data we have collected reliably define such a phase boundary.

The results of refined and calculated magnetic moments and charge neutrality calculations are presented in Table 4-2. Magnetic moments of $4\mu_B$ for Mn^{3+}, $3\mu_B$ for Mn^{4+} and $3\mu_B$ for Cr^{3+} are used. Calculated magnetic moments are found by considering the probability that Mn^{4+} has no Cr^{3+} near neighbor, thereby resulting in ferromagnetic alignment of Mn^{3+} and Mn^{4+} (e.g. if Cr^{3+} only has Mn^{3+} near neighbors, the Cr^{3+} and Mn^{3+} will have a parallel alignment of moments). Column 10 of Table 4-2 contains solutions based upon Cr^{3+} replacing Mn^{3+} with reversed magnetic moment. At low doping, both produce similar solutions. However, there is a clear departure with increased Cr^{3+} content and the magnetic moments calculated using our model are in much better agreement with the measured values. Columns 2 through 9 of Table 4-2 contain charge

calculations based on the differing Mn^{3+} and Mn^{4+} concentrations in the B1 and B2 layers, derived from the fitted moments with column 9 containing the net charge calculated, demonstrating the degree of charge ordering in the doubled unit cells for $x \geq 0.194$. We suggest the persistence of charge ordering may stem from the Cr^{3+} and Mn^{4+} having the same t_{2g} electronic configurations.

Table 4-2 Calculated and refined magnetic moments (at 12K) and charge neutrality for all Cr concentrations. All columns except the last four are accounting for the charge while columns 9-11 present the calculated magnetic moments for comparisons to the final column that contains the refined magnetic moments.

Cr^{3+} Content	La + Sr - O	%	Mn^{3+}	%	Mn^{4+}	%	Cr^{3+}	Net charge	Cr^{3+} replaces Mn^{3+} with reversed spin (+ + -)	Cr^{3+} is FM to Mn^{3+} and AFM to Mn^{4+} (+ - +)	Mag Mom 12K Refined
Parent	-3.300	0.700	2.100	0.300	1.200				3.60	3.60	***
0.048	-3.300	0.652	1.956	0.300	1.200	0.048	0.144	0.000	3.36	3.18	3.13
0.062	-3.300	0.638	1.914	0.300	1.200	0.062	0.186	0.000	3.27	3.05	2.95
0.143	-3.300	0.557	1.671	0.300	1.200	0.143	0.429	0.000	2.70	2.46	2.48
.194 B1	-3.300	0.536	1.608	0.270	1.080	0.194	0.582	-0.030	2.37	2.36	2.55
.194 B2	-3.300	0.476	1.428	0.330	1.320	0.194	0.582	0.030	2.31	2.04	1.99
.211 B1	-3.300	0.509	1.527	0.270	1.080	0.221	0.663	-0.030	2.18	2.28	2.30
.211 B2	-3.300	0.449	1.347	0.330	1.320	0.221	0.663	0.030	2.12	1.95	1.80
.294 B1	-3.300	0.476	1.428	0.230	0.920	0.294	0.882	-0.070	1.71	2.28	2.24
.294 B2	-3.300	0.336	1.008	0.370	1.480	0.294	0.882	0.070	1.57	1.41	1.29
.365 B1	-3.300	0.495	1.485	0.140	0.560	0.365	1.095	-0.160	1.31	2.71	2.63
.365 B2	-3.300	0.175	0.525	0.460	1.840	0.365	1.095	0.160	0.99	0.61	0.53
.411 B1	-3.300	0.449	1.347	0.140	0.560	0.411	1.233	-0.160	0.98	2.65	2.79
.411 B2	-3.300	0.129	0.387	0.460	1.840	0.411	1.233	0.160	0.66	0.49	0.60
.485 B1	-3.300	0.325	0.975	0.190	0.760	0.485	1.455	-0.110	0.42	2.21	2.10
.485 B2	-3.300	0.105	0.315	0.410	1.640	0.485	1.455	0.110	-0.20	-0.69	-0.80
.579 B1	-3.300	0.085	0.255	0.330	1.320	0.585	1.755	0.030	-0.43	2.40	2.20
.579 B2	-3.300	0.145	0.435	0.270	1.080	0.585	1.755	-0.030	0.37	-1.53	-1.70
*Note - value from Martin & Shirane [19]											

Wollan and Koehler [17] previously observed the additional intensity corresponding to a doubling of the unit cell and proposed that the system transitioned from a "C" type to a "CE" type structure. Such ordering was originally proposed by Goodenough [14] as Jahn-Teller distorted or orbital ordering. Wollan and Koehler

proposed that excess Mn^{4+} ions from nonstoichiometric $LaMnO_{3+\&}$, would occupy the Mn^{3+} sites but with reversed spin. In the Cr-substituted system, the Cr^{3+} ion is electronically the same as the Mn^{4+} ion, suggesting the possibility of additional Mn^{4+}-like behavior. Goodenough [14] additionally argued that if the Mn^{3+} and excess Mn^{4+} ions formed part of an ordered lattice, double exchange would be inhibited due to a lifting of the degeneracy of the Mn^{3+}-O-Mn^{4+} with Mn^{4+}-O-Mn^{3+}, and the ordered state would exhibit high electrical resistivity. Both are characteristics of the Cr-doped system for $x>0.142$ [23].

On the basis of our refined neutron scattering data and magnetic measurements, a phase diagram is provided in Figure 4-8. The metal to semiconductor and metal to insulator transition boundaries are taken from Kallel et al. [23] and the T_C of the parent compound is taken from Martin and Shirane [18]. The large orange-filled circles are our T_C values extracted from M_{ZFC} magnetic measurements. The hollow circles are the inflection points at temperatures well below T_C, also extracted from M_{ZFC} magnetic measurements. The small blue-filled circles, green-filled diamonds, red-filled diamonds, and pink-filled triangles stem from neutron refinements. We suggest that the area encompassed by the line passing through the M_{ZFC} inflection points at temperatures less than T_C, is the boundary of charge order, the peak of which occurs at $x=0.413$, the same value at which the quantities of Mn^{3+} and Mn^{4+} are approximately equal. These are the same samples for which the neutron refinements at 12K showed a doubled unit cell. The onset of semiconductor behavior indicates the onset of localization of the charge carriers and associated with charge ordering. The transition between ferromagnetic metal to ferromagnetic semiconductor [23] correlates with the first appearance of an inflection

point at low temperatures in the M_{ZFC} curves. The transition between a ferromagnetic semiconductor to a ferromagnetic insulator [23] at around x=0.19, correlates with a significant change in the slope of the boundary line between the charge ordered ferromagnetic region and the ferromagnetic insulator phases and the first observance of the new reflection (011) + (003) corresponding to a doubled unit cell along the c-axis in the neutron data. We have also observed similar behavior in our study of the $La_{0.7}Sr_{0.3}Mn_{1-x}Ni_xO_3$ system [submitted for publication] but occurring over a much reduced span of Ni content.

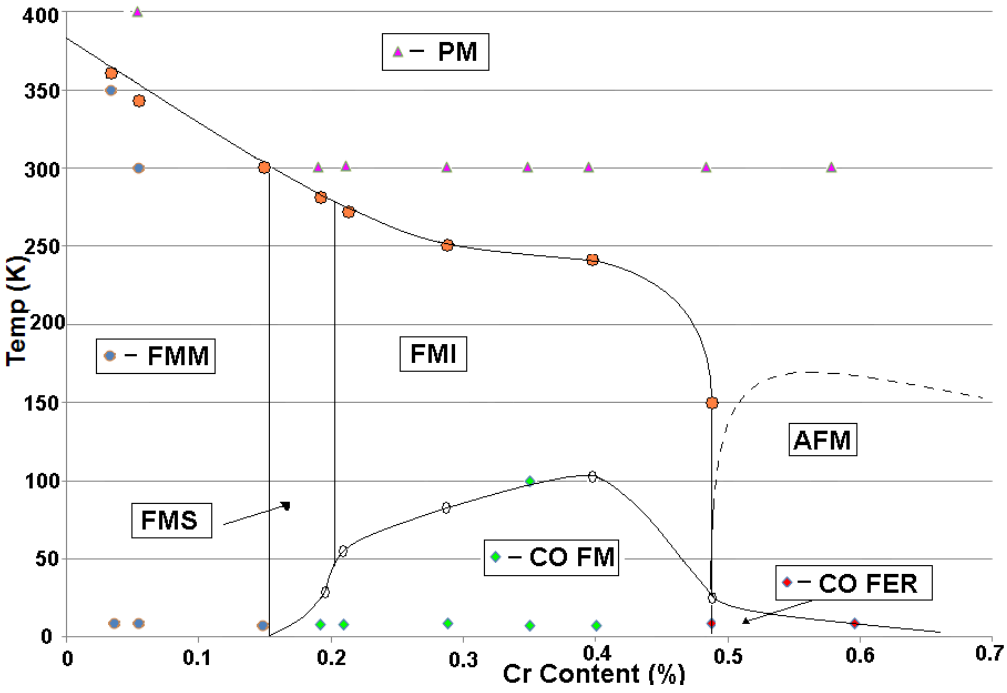

Figure 4-8 Phase diagram depicting Temperature vs. Cr content. Lines are provided as guides that fit the results from magnetic and neutron data. The dotted line identifying the antiferromagnetic (AFM) boundary is drawn as a best estimate as we have no data collected at the temperatures necessary to clearly define this boundary. The solid round blue-filled, triangular orange-filled, diamond green-filled and square red-filled data points are obtained from neutron scattering. The large orange-filled round points are derived T_C transitions from our magnetic data and the hollow circles are transition points below T_C within our magnetic data. The magnetic phases are: ferromagnetic metal (FMM), ferromagnetic semiconductor (FMS), ferromagnetic insulator (FMI), charge ordered ferromagnetic (CO FM), charge ordered ferrimagnetic (CO FER), AFM, and

paramagnetic (PM).

4.5 CONCLUSIONS

We have studied the structural and magnetic properties of the $La_{0.7}Sr_{0.3}Mn_{1-x}Cr_xO_3$ system and have presented an ordering schema that clarifies previous findings of the coexistence of ferromagnetism and antiferromagnetism in this system by accounting for both the ferromagnetic and antiferromagnetic couplings previously attributed to the Cr^{3+} ion with the Mn^{3+} and Mn^{4+} ions respectively. We find that the introduction of Cr^{3+} causes Mn^{4+} to reverse spin, but not Mn^{3+}, providing for a parallel alignment of Cr^{3+} and Mn^{3+} magnetic moments and an antiparallel alignment of Cr^{3+} and Mn^{4+} magnetic moments. Neutron diffraction is the only experimental tool that can provide such a direct measurement of magnetic structure.

Using neutron diffraction, we find:

1) At 12K, the observed magnetic moments require that the Cr^{3+} ion replace the Mn^{3+} ion with the same magnetic moment, resulting in ferromagnetic Cr^{3+}-O-Mn^{3+} and antiferromagnetic Cr^{3+}-O-Mn^{4+} superexchange interactions, that cause the Mn^{4+} to reverse its magnetic moment and break the Mn^{4+}-O-Mn^{3+} double exchange . The antiferromagnetic Cr^{3+}-O-Mn^{4+} and Cr^{3+}–O-Cr^{3+} superexchange drive the system toward an antiferromagnetic ordered system.

2) At 12K, charge ordering accompanies the metal to insulator transition at x~0.19, causing the system to transition from a single ferromagnetic state to a layered, charge-ordered ferromagnetic state for $x \geq 0.914$, where the in-plane

moments are aligned and parallel while inter-plane moments are antiparallel. The system transitions to a charge ordered antiferromagnetic state at $x \leq 0.485$, providing ferromagnetism.

3) The magnetic unit cell at 12K for $x<0.194$ is ferromagnetic, with the itinerant electrons providing the metallic state.

4) T_c decreases with increasing Cr content and drops below room temperature for $x > 0.19$.

5) The lattice parameters and unit cell volume decrease with increasing Cr content while the oxygen content remains stoichiometric within error tolerances, requiring the chromium ion to be Cr^{3+}.

6) All samples show a single perovskite phase and a small amount of a $MnCr_2O_4$ impurity phase that tends to increase with increased Cr content.

Using magnetization measurements, we find:

1) The low temperature magnetization differences between the M_{ZFC} and M_{FC} curves are due to competition between ferromagnetic Cr^{3+}-O-Mn^{3+} and Mn^{3+}-O-Mn^{4+} interactions and antiferromagnetic Cr^{3+}-O-Mn^{4+} interactions; the Mn^{3+}-O-Mn^{3+} interactions being weakly ferromagnetic or antiferromagnetic, impacting the measured magnetic moments very little.

2) The antiferromagnetic-like inflection points at temperatures much lower than T_C in the M_{ZFC} and M_{FC} magnetic measurements likely form the boundaries of charge ordering for the system. The peak of this boundary occurs at $x=0.413$, the value at which the quantity of Mn^{3+} approximately equals the quantity of

Mn^{4+}; the same value to which the M_{ZFC} and M_{FC} curves contain a long magnetic tail that does not go to zero at temperatures >300K.

3) The onset of metal to semiconductor behavior is coincident with the onset of charge ordering.
4) The magnetization saturation separation between the x=0.14 and x=0.21 correlates with the transition from the metal to insulator transition.
5) Evidence that the onset of ferrimagnetism may be the cause of the separation between the x=0.406 and x=0.485 magnetization vs magnetic field.

While magnetic measurements may leave some ambiguity about the nature of the low temperature state, the neutron-diffraction data clearly show that long range magnetism comprised of competing ferromagnetic and antiferromagnetic interactions between Mn^{3+}, Mn^{4+} and Cr^{3+} occur over a large range of compositions. Further, while the neutron data can only give an average magnetic moment for each distinct site, the totality of these results indicate Cr is in the Cr^{3+}state in the perovskite phase, in good agreement with previous work [1, 23, 24, 25, 27, 28]. The neutron data support the Cr^{3+}-O-Mn^{4+} antiferromagnetic superexchange and Cr^{3+}-O-Mn^{3+} ferromagnetic superexchange mechanisms drive the magnetic behavior of this system.

4.6 REFERENCES

1. Jonker, G. H. and Van Santen, J. H., Physica, vol. 16, 337-349, (1950)
2. Myron B. Salamon, Marcelo Jaime, Rev of Mod Phys, 73,583 (2001)

3. P. Schiffer, A. P. Ramirez, W. Bao, and S.W. Cheong, Phys. Rev. Lett., 75, 3336 (1995)
4. L. Brorovskikh, G. Mazo, E. Kemnitz, Solid State Sci, 5, 409-417 (2003)
5. R.J.H. Voorhoeve, D.W. Johnson, J.P. Remeika, P.K. Gallagher, Science 195, 827-833 (1977)
6. J.T. Vaughey, J.R. Mawdsley, T.R. Krause, Mater Res Bul, 42, 1963-1968 (2007)
7. A. J. Millis, P. B. Littlewood, and B. I. Shraiman, Phys. Rev. Lett., 74, 25, 5144 (1995)
8. A.J. Millis, Phys Rev. B 53, 8434 (1996)
9. W. Archiald, J.-S. Zhou, J.B. Goodenough, Phys. Rev. B 53, 14445 (1996)
10. Zener, C., Phys. Rev., vol. 82, 403-405 (1951)
11. H. A. Kramers, Physica 1, 182 (1934)
12. H. A. Jahn, E. Teller, Proceedings of the Royal Society of London. Series A, Mathematical and Physical Sciences, 161, 905, 220 (1937)
13. J.B. Goodenough and A. L. Loeb, Phys Rev., 98, 2, 391 (1955)
14. Goodenough J. B., Phys Rev, 100, 2, 564, (1955)
15. A. Urushibara, Y. Moritomo, T. Arima, A. Asamitsu, G. Kido, and Y. Tokura, Phys. Rev. B 51, 14 103 (1995)
16. B.C. Tofield, W.R.Scott, J of Solid State Chem., 10, 183 (1974)
17. Wollan, E. O., Koehler, W. C., *Phys. Rev*., vol. 100, 545-563, (1955)
18. Martin, M., Shirane, G., Endoh, Y., Hirota, K., Moritomo, Y., Tokura, Phys. Rev., 53 (21) 14285-14290 (1996)
19. G. H. Jonker and J. H. Van Santen, Physica 19, 120 (1953)

20. G. H. Jonker, Physica 22, 707 (1956)

21. Oishi, M., Yashiro, K., Sato, K, Mizusaki, J.,and Kawada, T., J. of Solid State Chem., 181, 3177 (2008)

22. O.Z. Yanchevskii, A. G. Belous, A. I. Tovstolytkin, O. I. V'unov, D. A. Durilin, Inorg. Mat., 42, 10 1121 (2006)

23. Kallel, N., Dhahri J., Zemni, S., Dhahri, E., Oumezzine M., Ghedira, M., and Vincent, H., Phys. Status Solidi, 184, 2, 319 (2001)

24. N. Kallel, K. Frohlich, M. Oumezzine, M. Ghedira, H. Vincent and S. Pignard, Phys. Stat. Sol. 1, 7, 1649 (2004)

25. Sun, Y., Tong, W., Xu, X, and Zhang, Y., Appl. Phys. Lett., 78, 5, 643 (2001)

26. Li, W., Zhang, B., Lu, W., Sun, Y., and Zhang Y., J of Phys. and Chem. of Solids, 68, 1749 (2007)

27. J. B. Goodenough, A. Wold, R. Arnott, N. Menyuk, Phys Rev. 124, 373 (1961)

28. Zhe Qu, Li Pi, Shun Tan, Simi Chen, Zekun Deng and Yuheng Zhang, Phys Rev B. 73, 1847 (2006)

29. T. S. Zhao, W. X. Xianyu, B. H. Li and Z. N. Qian, J. of All. and Com. 459, 29 (2008)

30. R. D. Shannon, Acta Crystallogr., Sect. A: Cryst. Phys., Diffr., Theor. Gen. Crystallogr. 32, 751 (1976).

31. J. Rodriguez-Carvajal, FULLPROF 2K, Version 3.00, Laboratoire Leon Brillouin-JRC, 2004

32. Thomas F. Creel, Jinbo B. Yang, Mehmet Kahveci, Jagat Lamsal, Satish K. Malik, S. Quezado, B. W. Benapfl, H. Blackstead, O. A. Pringle, William B. Yelon and William J. James, IEEE Tran. on Mag., 46, 6, 1832 (2010)

33. R. Mahendiran, M. Hervieu, A.Maignan, C. Martin, B. Raveau, Sol St Comm. 114, 429 (2000)

34. Thomas F. Creel, Jinbo B. Yang, Mehmet Kahveci, Jagat Lamsal, Satish K. Malik, S. Quezado, B. W. Benapfl, H. Blackstead, O. A. Pringle, William B. Yelon and William J. James, MRS Proceedings, 1327 , mrss11-1327-g08-02 doi:10.1557/opl.2011.852 (2011)

35. J. Kanamori, J. Phys. Chem. Solids, 10, 87 (1959)

36. N. Kallel, Sami Kallel, Ahmed Hagaza, Mohamed Oumezzine, Physica B, 404, 285 (2009)

5. STRUCTURAL AND MAGNETIC PROPERTIES OF $La_{0.7}Sr_{0.3}Mn_{1-x}Ni_xO_3$ ($x \leq 0.4$)

Thomas F. Creel,[1] Jinbo Yang,[2] Mehmet Kahveci,[3] Satish K. Malik,[4] S. Quezado,[4] O. A. Pringle,[1] William B. Yelon,[5] William J. James[5]

[1]Department of Physics, Missouri University of Science and Technology, Rolla, MO, U.S.A.

[2]State Key Laboratory for Artificial Microstructure and Mesoscopic Physics and School of Physics, Peking University, Beijing

[3]Department of Physics, University of Missouri, Columbia, MO, U.S.A

[4]Departamento de Física Teórica e Experimental (DFTE), Universidade Federal do Rio Grande do Norte (UFRN), Natal, Brazil

[5]Department of Chemistry and Graduate Center for Materials Research, Missouri University of Science and Technology, Rolla, MO, U.S.A.

5.1 ABSTRACT

We have studied the structural and magnetic properties of $La_{0.7}Sr_{0.3}Mn_{1-x}Ni_xO_3$ (x=0.05, 0.1, 0.20, 0.30 and 0.40) perovskites using x-ray and neutron diffraction and magnetic measurements. Our data consist of neutron (λ = 1.479Å) and x-ray (λ = 1.5481Å; Cu Kα) powder diffraction and magnetization measurements. We previously suggested these systems transition from ferromagnetic to antiferromagnetic ordering with the intermediate concentrations containing coexisting domains of ferromagnetically and

antiferromagnetically ordered states. Upon further detailed examination, we find that the samples are homogeneous and that neutron data can be fitted to a single long-range magnetically ordered state. The compositional dependent changes are driven by a shift in the dominant near neighbor interaction from ferromagnetic to antiferromagnetic. In the intermediate compositions, peaks previously identified as due to antiferromagnetic ordering, in fact arise from charge ordering while the system remains in a ferromagnetic state with the Ni moments antiparallel to the Mn moments. This interpretation supersedes multiphase and spin glass models for these complex systems.

5.2 INTRODUCTION

Manganese-based perovskite materials continue to be of significant interest due to their wide ranging magnetic and electronic transport properties. From undoped $LaMnO_3$ to A-site doped $La_{1-x}Sr_xMnO_3$ to A-site and B-site doped $La_{1-x}Sr_xMn_{1-y}Z_yO_3$, these systems exhibit complex magnetic behavior, transitioning between ferromagnetic, paramagnetic and antiferromagnetic phases with little or no change in the underlying crystallographic structure. These perovskites are known for the unusually large effect that an external magnetic field has on their ability to transport electricity and heat [1, 2] while other typical magnetic materials show little sensitivity to the same fields. Prior to the study of these perovskites, only very “clean” metals with a large electronic mean free path in zero field and metallic multilayers were found to show large field effects on transport properties [1, 3, 4]. Applications of these mixed-valence perovskites include cathodes for solid oxide fuel cells, magnetic storage devices, magnetoresistive read heads, catalysts and collosal magnetoresistance (CMR) and giant magnetoresistence

(GMR) materials [5, 6, 7]. The magnetic and transport properties of these manganites have been described using double exchange, superexchange, semicovalent exchange, Jahn-Teller distortions, and electron-phonon coupling [8, 9, 10, 11, 12, 13, 14, 15].

$LaMnO_3$ is antiferromagnetically ordered at low temperatures (T_N~150K) and is a charge gap insulator due to the large correlation energy of the *d* electrons in the e_g band (d_z^2, $d_{x^2-y^2}$) [16, 17]. Charge neutrality dictates that all the Mn ions are in the 3+ state. Wollan and Koehler [3] were able to produce Mn^{4+} in $LaMnO_{3+\delta}$ by firing at different temperatures in an oxygen-rich environment. They produced up to 20% Mn^{4+} at an 1100C firing temperature in oxygen.

Upon replacing trivalent La^{3+} by divalent Sr^{2+}, Mn^{4+} is created as can be described by the formula $La^{3+}_{1-x}Sr^{2+}_{x}\left(Mn^{4+}_{x}Mn^{3+}_{1-x}\right)O^{2-}_{3}$. By substituting trivalent La^{3+} for divalent Sr^{2+} or Ca^{2+}, Wollan and Koehler [3] were able to increase the Mn^{4+} concentration. They found the Curie temperature (T_C) to be directly linked to the amount of Mn^{4+} present and samples with 30% Mn^{4+} exhibited almost pure ferromagnetic ordering with approximately the full predicted ferromagnetic moment per atom. For x~0.35, their samples were purely ferromagnetic whereas for $x<0.25$ and $0.40<x<0.5$, their samples contained both ferromagnetic and antiferromagnetic phases.

Martin and Shirane [18] determined T_C for $La_{0.7}Sr_{0.3}MnO_3$ to be 378.1K. The system is a ferromagnetic metal for temperatures $\leq$ 378.1K with a magnetic moment per B-site of about 3.6 μ_B. Urushibara et al. [17] determined T_C for $La_{0.7}Sr_{0.3}MnO_3$ to be 369K with a magnetic moment of $3.5\mu_B$ when prepared in a 50/50 mixture of O_2 and Ar. Their system was metallic for all temperatures. Both [17, 18] magnetic moments are in good agreement with the calculated value of $3.7\mu_B$/formula unit assuming complete spin

alignment of the magnetic moments of the Mn ions, $4\mu_B$ for Mn^{3+} and $3\mu_B$ for Mn^{4+}. In the metallic region [17, 19, 20, 21], the dominant interaction between Mn^{3+} and Mn^{4+} is double exchange. For the other transition metal pairs, the superexchange mechanism is dominant and antiferromagnetic. A possible exception to this rule is the Mn^{3+}-O^{2-}-Mn^{3+} superexchange interaction which may be either ferromagnetic or antiferromagnetic [3].

While there is a body of research in the rare earth Ni-based perovskites ($RNiO_3$) [22] that find Ni to be in the Ni^{3+} low spin state, there has been little study of the Ni-substituted lanthanum-based perovskite, $La_{1-y}Sr_yMn_{1-x}Ni_xO_3$ where $0 \leq y \leq 0.3$ and $0 \leq x \leq 0.4$. There remains some ambiguity regarding the state of the Ni ion, whether it is Ni^{2+} or Ni^{3+}, whether the exchange interaction is ferromagnetic or antiferromagnetic, about the exchange mechanism (superexchange or double exchange) and the transport properties. In their study of $La_{0.67}Sr_{0.33}Mn_{1-x}Ni_xO_3$, Wang et al. [23] found Ni to be in the Ni^{2+} state citing x-ray spectroscopy but providing no data. They attributed their reduced volume and cell parameters to oxygen non-stoichiometry (Ni^{2+} is much larger than Mn^{3+}). They found for x=0.20, a broad temperature transition from ferromagnetic to paramagnetic behavior in their magnetization measurements which they attributed to spin glass states. Further, they found the metal-to-insulator transition to occur between x =0.15 and x=0.20 with x=0.20 to be completely insulating, and with increased Ni content, a reduction of T_C, cell parameters, volume and an increase in the temperature differences between T_C and the metal-to-insulator transition. In their study of $La_{0.70}Sr_{0.30}Mn_{1-x}Ni_xO_3$, Feng et al. [24] found the metal-to-insulator transition occurring at x~0.20, with T_C and magnetization decreasing with increasing Ni content. They also found saturation magnetization values smaller than the calculated values assuming the Ni ion to be ferromagnetically coupled to

the Mn ions. Wold et al. [25] found Ni ions in the Ni^{2+} and Ni^{3+} states in $LaMn_{1-y}Ni_yO_3$, with the Ni^{3+} in the low spin state with a ferromagnetic Ni^{3+}- O^{2-}-Mn^{3+} superexchange interaction.

A possible resolution to these contradictions is to assume that the dominant interaction controlling the nickel ordering is the antiferromagnetic interaction between Mn^{4+}-O^{2-}-Ni^{3+} rather than the ferromagnetic Ni^{3+}-O^{2-}-Mn^{3+} interaction. This interpretation arises from our neutron diffraction results and allows us to describe the magnetic behavior over the full compositional range.

In this study, we replace Mn in $La_{0.7}Sr_{0.3}MnO_3$ with up to 40% Ni and use neutron scattering, x-ray scattering and magnetic measurements to study the nuclear and magnetic structure and magnetic properties of the Ni-substituted perovskite. Neutron diffraction is uniquely appropriate to study the nuclear and magnetic structure of these perovskites due to the neutron magnetic scattering and the unique properties of the nuclear neutron scattering (including the negative Mn scattering length) which allows the crystal structure and the oxygen stoichiometry to be accurately determined. The possible oxidation states, electronic configuration, spin states, crystal radii and ionic radii of our constituent elements are listed in Table 5-1 [26]. The ionic radii point towards Ni being in the low-spin Ni^{3+} state upon substitution of Ni for Mn in the perovskite structure.

Table 5-1 Crystal and Ionic radii from R. D. Shannon [26].

Ion	Ox. State	Elec. Config.	Coord. #	Spin State	Crystal Rad (Å)	Ionic Rad (Å)
La^{+3}	3	$4d^{10}$	6		1.172	1.032
Sr^{+2}	2	$4p^6$	6		1.320	1.18
O^{-2}	-2	$2p^6$	6		1.260	1.4
Mn^{+2}	2	$3d^5$	6	LS	0.810	0.67
Mn^{+2}	2	$3d^5$	6	HS	0.970	0.83
Mn^{+3}	3	$3d^4$	6	LS	0.720	0.58
Mn^{+3}	3	$3d^4$	6	HS	0.785	0.645
Mn^{+4}	4	$3d^3$	6		0.670	0.53
Mn^{+7}	7	$3p^6$	6		0.600	0.46
Ni^{+2}	2	$3d^8$	6		0.830	0.69
Ni^{+3}	3	$3d^7$	6	LS	0.700	0.56
Ni^{+3}	3	$3d^7$	6	HS	0.740	0.6
Ni^{+4}	4	$3d^6$	6	LS	0.620	0.48

5.3 EXPERIMENTAL

Polycrystalline samples of $La_{0.7}Sr_{0.3}Mn_{1-x}Ni_xO_3$ ($0 \leq x \leq 0.4$) were prepared using a conventional solid-state reaction method in air. Appropriate amounts of high purity La_2O_3, $SrCO_3$, MnO_2, and Ni_2O_3 powders were weighed and mixed according to the desired stoichiometry for each sample. The samples were ground using a high energy ball mill for 5 hours, pressed into pellets at 10,000 psi and then fired at 1350 C for 24 hours in air with a room-air quench upon removal from the oven. After 24 hours of cooling, the samples were re-ground, pressed and fired using the same process.

Neutron-diffraction data were collected at the University of Missouri Research Reactor (MURR) facility using a position sensitive detector diffractometer with a neutron

wavelength of λ = 1.479Å. X-ray diffraction data were collected with an XPERT PRO diffractometer using a Cu Kα wavelength of λ = 1.5481Å. Powder diffraction data were refined using the FullProf suite of programs [27]. Magnetic measurements were performed at the University of Brasilia, Brasilia DF, Brazil using a vibrating sample magnetometer and a Quantum Design Physical Property Measurement System with the AC magnetization option.

5.4 RESULTS AND DISCUSSION

In our previous work on $La_{0.7}Sr_{0.3}Mn_{1-x}Ni_xO_3$ [28], we reported that the system crystallizes in the rhombohedral perovskite structure. At low nickel concentrations the system is a ferromagnetic metal while at high concentrations the system is an antiferromagnetic insulator. In the intermediate regions we previously reported the coexistence of two magnetic phases.

In this work, we provide a revised magnetic ordering schema based on further analysis of neutron-scattering data and magnetic measurements. At low Ni concentrations the system is comprised of ferromagnetic layers (Figure 5-1a) with the Ni^{3+} moments aligned

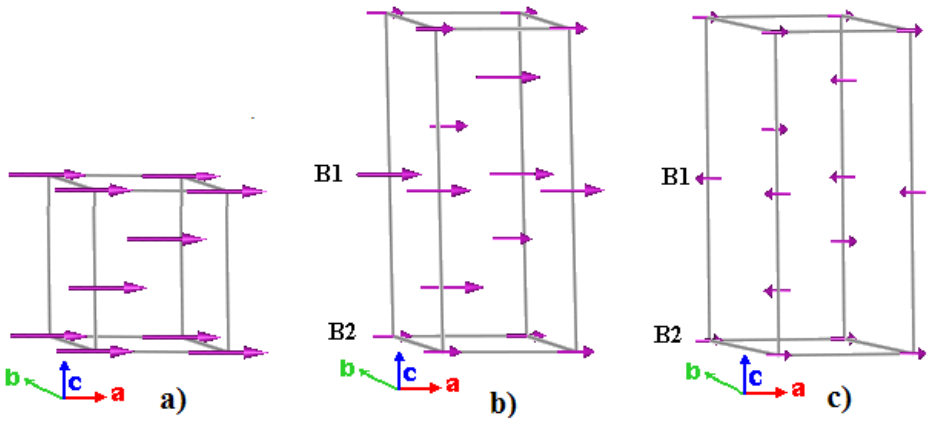

Figure 5-1 Magnetic unit cells for the perovskite. Depicted magnetic unit cells are: a) ferromagnetic unit cell for 8% Ni, b) the ferromagnetic (unequal moment magnitudes) doubled unit cell containing B1 and B2 layers for 21% Ni and c) the antiferromagnetic unit cell containing B1 and B2 layers for 31% Ni. The moment directions in the basal plane and labeling of B1 and B2 layers are arbitrary and chosen for convenience.

antiferromagnetically to the Mn^{3+} and Mn^{4+} moments, causing a net reduction in the measured ferromagnetic moments as before. However, with sufficient nickel, instead of random ferromagnetic and antiferromagnetic domains, charge ordering appears, leading to a ferromagnetic state with layers of unequal ferromagnetic moments (Figure 5-1b). At high nickel concentrations, the interaction between adjacent planes is antiferromagnetic with the Mn^{4+} moments antiparallel to the Ni^{3+} and Mn^{3+} moments (Figure 5-1c). Only peaks identified as due to antiferromagnetic ordering are observed in the neutron-diffraction data. Peaks consistent with ferromagnetic and antiferromagnetic states are observed and fitted with a single phase model.

Refined neutron-diffraction data from the prepared stoichiometries of x = 0.05, 0.10, 0.20, 0.30 and 0.40 result in values of x = 0.05, 0.08, 0.16, 0.21 and 0.31 with the presence of 0.26%, 1.65%, 3.63%, 7.31% and 8.89% of NiO impurity respectively. The NiO percentages are derived from multiphase Rietveld refinements using the FullProf

code. For the remainder of this discussion, we will refer to the refined stoichiometries. The neutron refinement results are presented in Table 5-2. The atomic parameters (a, c and volume) decrease with increasing Ni content while the oxygen stoichiometry changes very little. The decreasing cell parameters combined with the constant oxygen stoichiometry indicate Ni to be in the Ni^{3+} state. If Ni were in the Ni^{2+} state, one would expect the volume to increase, given stoichiometric oxygen.

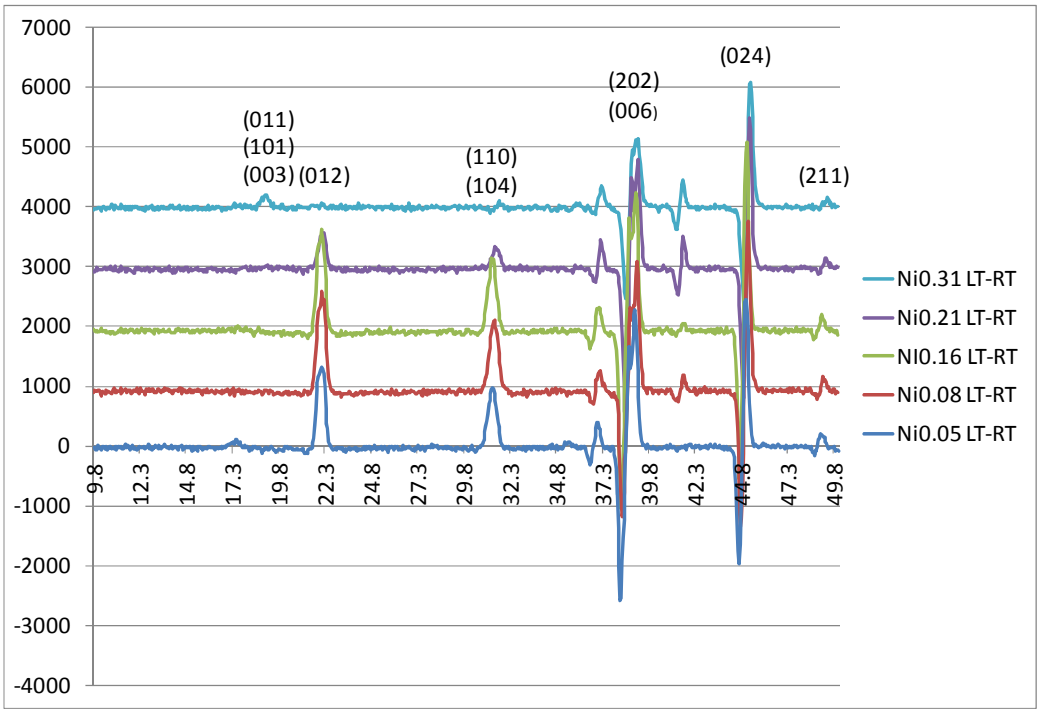

Figure 5-2 Intensity versus scattering angle of neutron-scattering data collected at 300K subtracted from data collected at 12K for all Ni-substituted concentrations. Successive concentrations are offset by 1000 counts.

Figure 5-2 shows the neutron diffraction data at 300K subtracted from data collected at 12K. This difference curve allows the elimination of all effects which are not temperature dependent. The large positive and negative swings for the (202), (006) and (024) reflections are due to temperature-driven shifts in lattice parameters, causing a shift

in peak positions. Significant reductions in the ferromagnetic intensities occur between x=0.16 and x=0.21. The (012) and the combined (110) and (104) peaks contain both nuclear and ferromagnetic contributions to the intensities. The ferromagnetic contribution decreases steadily with increasing nickel content and disappears completely before x=0.31. At x=0.31, a peak associated with a doubling of the unit cell along the c-axis with indices (101 + 003) is clearly visible. In fact, this peak is barely visible at x=0.21. The peaks not annotated are associated with the NiO phase.

At 12K, ferromagnetic ordering is found for $0.05 \leq x \leq 0.16$. The refined moment on the manganese site decreases with increasing nickel content. The magnetic cell is pictured in Figure 5-1a. At x=0.05, a magnetic moment of $3.27\mu_B$ per B-site is obtained. This value is lower than that obtained for the parent perovskite $La_{0.7}Sr_{0.3}MnO_3$ where Martin and Shirane [18] find $3.6\mu_B$ per manganese site while Urushibara et al [17] find $3.5\mu_B$ per manganese site in a reduced oxygen atmosphere. This behavior points to an antiferromagnetic alignment between the Ni^{3+} and the ferromagnetically aligned Mn^{3+} and Mn^{4+} moments at low concentrations.

Table 5-2 Refined parameters: magnetic moment (μ_B), a, c, volume, and χ^2 versus refined Ni content from neutron-diffraction refinements. The magnetic moments are calculated on the Mn atom occupational sites and represent average magnetic moments per Mn site. The number in parenthesis represents the 1σ uncertainty in the last digit.

Ni Content		0.05	0.08	0.16	0.21	0.31
12K	$\mu_{B\text{-}1,\ Mn}(\mu_\beta)$	3.27 (2)	3.15 (2)	2.91 (2)	1.67 (9)	- 1.09 (3)
	$\mu_{B\text{-}2,\ Mn}(\mu_\beta)$	3.27 (2)	3.15 (2)	2.91 (2)	2.59 (9)	1.09 (3)
	a (Å)	5.4941 (1)	5.4910 (1)	5.4831 (1)	5.4769 (2)	5.4650 (2)
	c (Å)	13.3110 (3)	13.3032 (3)	13.2841 (3)	13.2731 (5)	13.2511 (7)
	Cell Vol $(Å)^3$	347.96 (1)	347.37 (1)	345.87 (1)	344.81 (2)	342.74 (2)
	Oxygen Stoich	3.02 (2)	3.01 (2)	2.98 (2)	3.03 (3)	2.96 (3)
	χ^2	3.22	3.38	2.27	2.74	2.79
300K	$\mu_{FM,\ Mn}(\mu_\beta)$	1.91 (3)	1.25 (4)	0.3 (2)	*n/a*	*n/a*
	$\mu_{AFM,\ Mn}(\mu_\beta)$	*n/a*	*n/a*	*n/a*	*n/a*	0.53 (6)
	a (Å)	5.5007 (1)	5.4988 (1)	5.4901 (1)	5.4821 (2)	5.4723 (2)
	c (Å)	13.3485 (4)	13.3435 (3)	13.3219 (4)	13.3121 (5)	13.2911 (7)
	Cell Vol $(Å)^3$	349.78 (2)	349.41 (1)	347.75 (2)	346.48 (2)	344.69 (3)
	Oxygen Stoich	3.02 (2)	3.01 (2)	2.98 (2)	3.03 (3)	2.96 (3)
	χ^2	2.80	2.56	2.27	2.88	2.97

Magnetic moments for Mn^{3+} ($4\mu_B$) and Mn^{4+} ($3\mu_B$) are reliably known from a large body of works. However, the magnetic moment for the Ni^{3+} ion is not known in this system. To determine the Ni^{3+} magnetic moment, we fit a straight line to the net moment between x=0 and x=0.16 while accounting for the reduction of the Mn^{3+} concentration. For x=0 (parent compound), we use the value of $3.6\mu_B$ from Martin and Shirane [18]. For the remaining points, we use our refined values. This yields a Ni^{3+} moment of $1.54\mu_B$ in reasonable agreement with the $1.73\mu_B$ calculated by Goodenough and Loeb [14] for the Ni^{3+} square (dsp^2) covalent bond. It is closer to the $1\mu_B$ spin only value of low spin Ni^{3+} than the spin only value of $3\mu_B$ of high spin Ni^{3+}. The same results are seen in the $RNiO_3$ [22].

At 12K for x=0.21, in addition to the ferromagnetic intensity observed on the (012) and the combined (110) + (104) peaks, we observe the emergence of a very small peak comprised of the (101) and (003) reflections that is only present at low temperature

and therefore conclude that it is magnetic. This implies a doubling of the unit cell in which the B-site is split into B1 and B2 layers (Figure 5-1b). The insets in Figure 5-3 show the observed and fitted data using the best nuclear-only model. The misfits highlight the magnetic contributions. This was previously explained by using a two phase model consisting of a small antiferromagnetic component in a ferromagnetic matrix [28]. Upon further study, we find no evidence of phase separation in the neutron data; all the peak widths and shapes are consistent with a single phase material. If the system had separated into antiferromagnetic and ferromagnetic domains, we would expect to find different cell parameters yielding doubled peaks or causing peak broadening, if for no other reason than differing magnetostriction. Therefore, we looked for an alternative single phase model where all the magnetic scattering can be fit with a single magnetic phase. This is accomplished by considering a charge ordered state in which the unit cell is doubled along the c-axis (Figure 5-1b, Table 5-3). In this charge ordered state, all of the Mn^{4+} is assumed to be on the B2 layer, Ni^{3+} is distributed on both layers and Mn^{3+} accounts for the remaining sites on both layers.

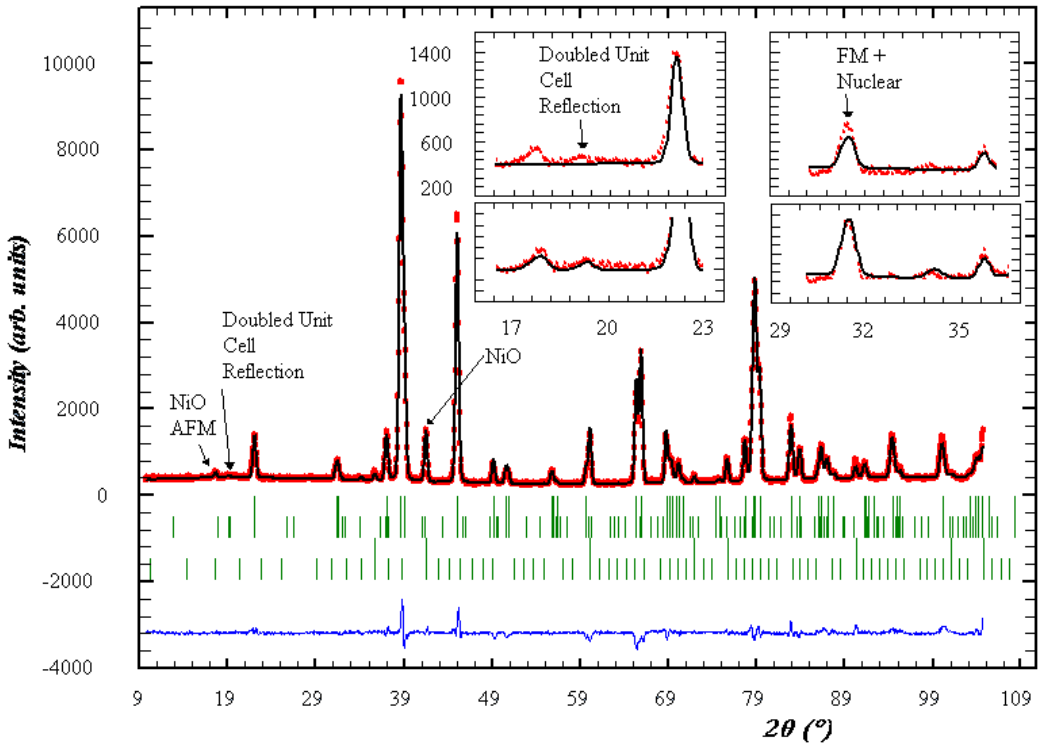

Figure 5-3 Neutron-diffraction refinement of the $La_{0.7}Sr_{0.3}Mn_{0.79}Ni_{0.21}O_3$ sample at 12K (refined stoichiometric Ni content). The reflection markers below the plot are, in order, nuclear perovskite structure, ferromagnetic perovskite structure, NiO nuclear structure and AFM NiO structure. The insets show the magnified regions around the small magnetic peaks prior to magnetic refinement.

This is the most highly ordered configuration we can achieve with these cations. The net charge on the B1 and B2 layers is -0.30 and +0.30 respectively. The intensity observed from the (101) and (003) reflections can be solved using a unit cell doubled along the c-axis, allowing the (0,0,0), (2/3,1/3,1/3) and (1/3,3/2,2/3) reflections to be estimated independently of the (0,0,1/2), (2/3,1/3,5/6) and (1/3,2/3,1/3) positions within the $P\bar{1}$ space group, yielding different average moments in the B1 and B2 layers with parallel alignment. The refined moments on the two layers are $2.59\mu_B$ and $1.67\mu_B$, in

reasonable agreement with the moments calculated using our new model, $2.84\mu_B$ (calculation goes as $0.79*4\mu_B + 0*3\mu_B - 0.21*1.54\mu_B$) and $2.24\mu_B$.

At 12K for x=0.31, we only find antiferromagnetic ordering. The magnetic cell is depicted in Figure 5-1c. The fitted moment on the B-site is much lower than the moments observed in the lower-doped samples. The fitted moments can be modeled by assuming that the Ni^{3+} and Mn^{4+} moments are antiparallel while the Mn^{3+} and Ni^{3+} moments are parallel. The magnetic layers are antiferromagnetically stacked, supporting a ferromagnetic superexchange between Mn^{3+} and Ni^{3+} and an antiferromagnetic superexchange between Mn^{4+} and Ni^{3+} with the latter being dominant. Agreement between observed and calculated moments is achieved assuming constant Mn^{3+}, Mn^{4+} and Ni^{3+} moments at all x. This implies that the system is long range ordered, eliminating the need for spin glass or cluster models. The observed sharp diffraction peaks further support this conclusion.

Table 5-3 Calculated and refined magnetic moments (at 12K) and charge neutrality calculation for all Ni concentrations. All columns except the last two present charge neutrality calculations, the last two columns contain calculated and refined magnetic moments using $1.54\mu_B$ for Ni.

Ni Content	La + Sr - O Net charge	%	Mn^{3+} Net Charge	%	Mn^{4+} Net Charge	%	Ni^{3+} Net Charge	Total Net Charge	Mag Mom Calc ($\mu\beta$)	Mag Mom 12K Refined
Parent	-3.30	0.70	2.10	0.30	1.20				3.70	*3.6
0.05	-3.30	0.65	1.95	0.30	1.20	0.05	0.15	0.00	3.42	3.27
0.08	-3.30	0.62	1.86	0.30	1.20	0.08	0.24	0.00	3.26	3.15
0.16	-3.30	0.54	1.62	0.30	1.20	0.16	0.48	0.00	2.81	2.91
0.21-B1	-3.30	0.79	2.37	0.00	0.00	0.21	0.63	-0.30	2.84	2.59
0.21-B2	-3.30	0.19	0.57	0.60	2.40	0.21	0.63	0.30	2.24	1.67
0.31-B1	-3.30	0.39	1.17	0.30	1.20	0.31	0.93	0.00	1.14	1.09
0.31-B2	-3.30	0.39	1.17	0.30	1.20	0.31	0.93	0.00	-1.14	-1.09
*Note - value from Martin & Shirane [19]										

The results are summarized in Table 5-3 which gives the charge distribution and magnetic moments assuming stoichiometric oxygen. Also included are the calculated magnetic moments using our new model described above, where the Ni magnetic moments align antiferromagnetically to the ferromagnetically aligned Mn moments for $x<0.31$. At $x=0.31$, the system orders antiferromagnetically.

The Curie temperature in the ferromagnetic region decreases steadily with increased Ni concentration and is less than 300K at $x=0.21$. At $x=0.31$ the system is antiferromagnetic and T_N exceeds room temperature.

Magnetization measurements (Figure 5-4) indicate that T_C decreases with increasing Ni concentration. There are differences between the zero field-cooled versus field-cooled magnetization (M_{ZFC} and M_{FC}) below T_C for all samples. All samples except $x=0.05$ exhibit antiferromagnetic-like behavior below 50K. For $x=0.08$ and $x=0.16$, both M_{ZFC} and M_{FC} curves exhibit an antiferromagnetic-like transition at approximately 45K that increases in intensity with increased nickel content. With the onset of charge ordering at $x=0.21$, a distinctive antiferromagnetic-like transition at approximately 10K is seen only in the M_{ZFC} curve. The differences between M_{ZFC} and M_{FC} curves have routinely been ascribed to spin glass, spin clusters or re-entrant spin glass [23, 24, 29]. However, we believe that these differences are actually due to charge ordering and the complex competition between the Ni^{3+}-O-Mn^{3+} ferromagnetic couplings and the Ni^{3+}-O-Mn^{4+} and Ni^{3+}-O-Ni^{3+} antiferromagnetic couplings. For $x=0.08$ and 0.16, the applied magnetic field coerces a magnified magnetic response while at $x=0.21$, it suppresses the weakly charge ordered state as was observed by Tomioka et al [31] in the $Pr_{0.5}Sr_{0.5}MnO_3$ system.

The T_C's and the magnetic moments are in good agreement with those of Hu et al. [30] and Wang et al. [23]. There is a significant separation between M_{ZFC} and M_{FC} curves for x = 0.16 to 0.21, indicating a likely metal to insulator transition as observed by Feng et al [24] where they found this transition occurs near x=0.20. In our model the metal to insulator transition is also accompanied by charge ordering.

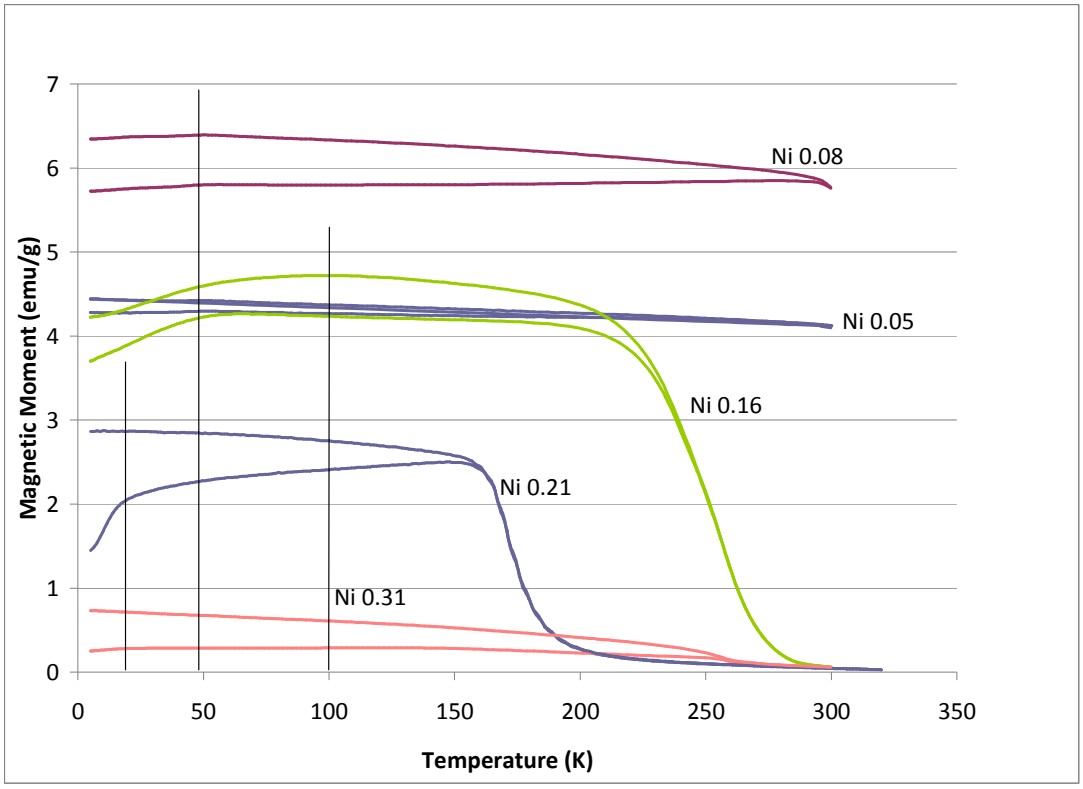

Figure 5-4 Zero field-cooled (M_{ZFC}) and 100 Oe field-cooled (M_{FC}) measurements of magnetization vs temperature for all nickel concentrations. For each sample, the M_{ZFC} is the lower while the M_{FC} is the upper segment of the curves. The vertical lines are to guide the eye.

The M_{ZFC} and M_{FC} curves for x=0.16 exhibit a broad ferromagnetic to paramagnetic transition, which may be an indication of the imminent onset of charge ordering and metal to insulator transition. The x=0.16 M_{ZFC} curve exhibits a transition to

an antiferromagnetic-like behavior below 50K while the M_{FC} curve exhibits an antiferromagnetic-like behavior below 100K that is a function of temperature. These M_{ZFC} and M_{FC} curves exhibit complex magnetic ordering in conjunction with the presence of a small amount of NiO. Our data are in agreement with that of Feng et al [24] and suggest that the metal to insulator transition occurs over a finite temperature range between x=0.20 and x=0.31 and may also be associated with a change from charge ordering to antiferromagnetism. In the M_{ZFC} and M_{FC} curves for x=0.21 and x=0.31, there are long tails of magnetization that do not go to zero out to 300K with x=0.21 spanning more than 125K while for x=0.31 the transition spans approximately 50K. For x=0.21, these long magnetization tails are likely due to a combination of charge ordering, competition between the ferromagnetic couplings of Ni^{3+}-Mn^{3+} moments and the antiferromagnetic couplings of the Ni^{3+}-Mn^{4+} and Ni^{3+}-Ni^{3+} moments and a small effect from NiO. The amount of NiO for x=0.31 is larger than for x=0.21 but the x=0.31 sample exhibits a smaller magnetic moment with a magnetic tail that spans a shorter temperature range. Therefore, although some of the magnetization tail may be attributed to the antiferromagnetic NiO, it is likely that the charge ordering and magnetic couplings have a larger influence. For x=0.31 the long magnetization tail is likely due to NiO.

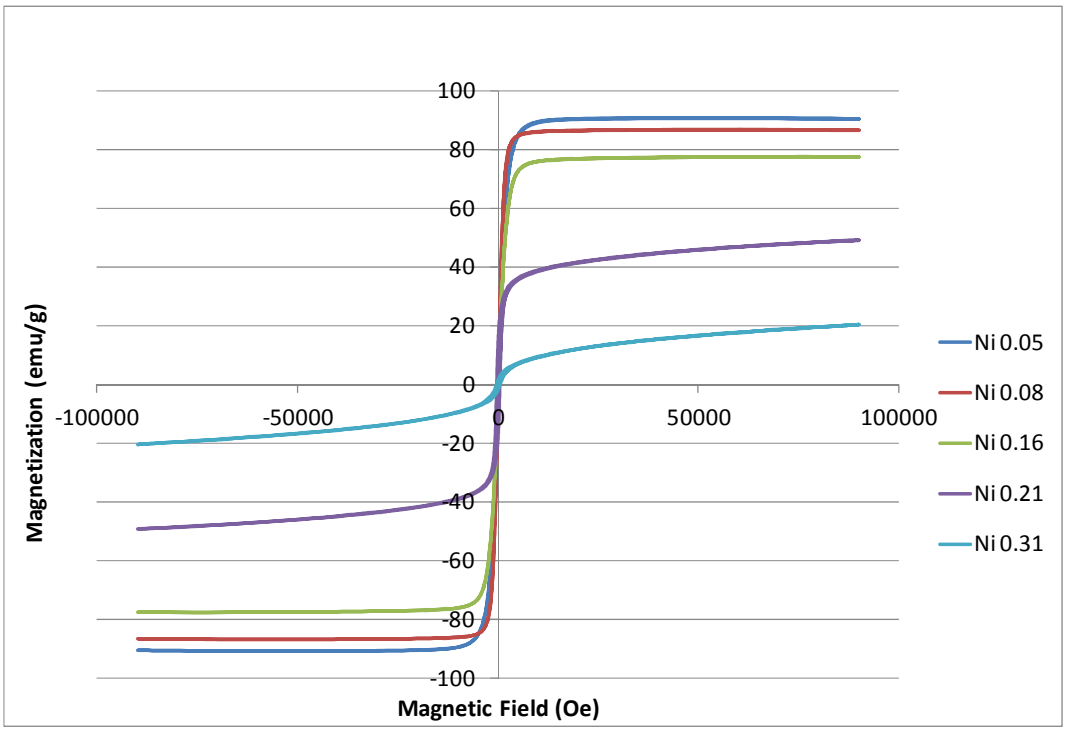

Figure 5-5 Magnetization vs. Magnetic Field at 12K for all Ni concentrations.

The magnetizations versus magnetic field curves at 5K are plotted in Figure 5-5. For x=0.05, 0.08 and 0.16, the magnetization saturates to values of 90.8emu/g, 86.7 emu/g and 77.5emu/g respectively. However, for x=0.21 and 0.31, maximum values of 49.29 emu/g and 20.42 emu/g are reached at a 9T field without complete saturation. These differences are likely additional indicators for the transition from ferromagnetic to antiferromagnetic interactions. The separation between x=0.16 and x=0.21 is witness to the onset of charge ordering and the metal to insulator transition as discussed by Feng et al [24], whereas the separation between x=0.21 and x=0.31 is attributed to the onset of antiferromagnetic ordering. One should note that the magnetization versus magnetic field data for the x=0.31 sample indicates a very small residual ferromagnetic component that is too small (~5 emu/g) to be observed in our neutron diffraction data.

5.5 CONCLUSIONS

We have studied the structural and magnetic properties of the $La_{0.7}Sr_{0.3}Mn_{1-x}Ni_xO_3$ system and have presented a new model that clearly accounts for the ferromagnetic and doubled-unit cell intensities observed. Neutron-diffraction is the only experimental tool that can provide a direct measurement of magnetic structure, and to our knowledge, this is the first powder neutron-diffraction study of this system.

Using neutron diffraction, we find:

7) All samples show a single perovskite phase and a small amount of a NiO impurity phase that increases with increasing Ni content.

8) At low Ni concentrations the system orders ferromagnetically while at high Ni concentration the system orders antiferromagnetically. At intermediate composition, the system shows charge ordering with a ferromagnetic ground state. For all compositions the neutron-diffraction data are fit with constant Ni^{3+}, Mn^{3+} and Mn^{4+} moments, excluding the existence of spin glass or cluster glass behavior.

9) The neutron-diffraction data clearly indicate that the antiferromagnetic coupling between Mn^{4+} and Ni^{3+} must be the driving force in this system.

10) The nickel moments align antiferromagnetically to the ferromagnetically coupled Mn^{3+} and Mn^{4+} moments for $x<0.31$. At $x=0.31$ the antiferromagnetic coupling between Ni^{3+} and Mn^{4+} moments becomes dominant, leading to a long range antiferromagnetic state.

11) The lattice parameters and unit cell volume decrease with increasing Ni content while the oxygen content remains stoichiometric within error

tolerances, requiring the nickel ion to be Ni^{3+}.

12) The magnetic unit cell for $x \geq 0.21$ consists of a doubled nuclear cell along the c-axis.

13) The likely exchange mechanism for Ni^{3+}-O^{2-}-Mn^{3+} is double exchange whereas for Ni^{3+}-O^{2-}-Mn^{4+} it is superexchange, accounting for the transition from charge ordering to antiferromagnetism as the Mn^{3+} concentration decreases.

Using magnetization measurements, we find:

6) Competition between the ferromagnetic couplings of Ni^{3+}-Mn^{3+} moments and the antiferromagnetic couplings of Ni^{3+}-Mn^{4+} and Ni^{3+}-Ni^{3+} moments as evidenced by the long tails of magnetization in samples with higher Ni concentration and antiferromagnetic-like behavior at lower temperatures.

7) Evidence of the imminent onset of charge ordering and metal to insulator transition in the x=0.16 sample from the broad ferromagnetic to paramagnetic transition, the separation between the x=0.16 and x=0.21 magnetization and magnetic moments, and the temperature-dependent M_{ZFC} and M_{FC} magnetization differences within the x=0.16 sample.

8) Agreement between our magnetic model derived from the neutron data with earlier studies of the dramatic change in magnetic behavior between x=0.16 and x=0.21 and between x=0.21 and x=0.31.

While magnetic measurements may leave some ambiguity about the nature of the low temperature state, the neutron-diffraction data clearly show that over a small range of

composition, long range magnetism comprised of competing ferromagnetic and antiferromagnetic interactions between Mn^{3+}, Mn^{4+} and Ni^{3+} coupled with charge ordering leads to a doubled unit cell with a ferromagnetic ground state.

5.6 REFERENCES

1. G. H. Jonker, and J. H. Van Santen, Physica, 16, 337-349, (1950).
2. Myron B. Salamon, Marcelo Jaime, Rev of Mod Phys, 73,583 (2001)
3. E. O. Wollan, W. C. Koehler, *Phys. Rev*., 100, 545-563, (1955)
4. J. B. Goodenough, Magnetism and the Chemical Bond. (Huntington: Krieger, 1976.)
5. L. Brorovskikh, G. Mazo, E. Kemnitz, Solid State Sci, 5, 409-417 (2003)
6. R.J.H. Voorhoeve, D.W. Johnson, J.P. Remeika, P.K. Gallagher, Science 195, 827-833 6(1977)
7. J.T. Vaughey, J.R. Mawdsley, T.R. Krause, Mater Res Bul, 42, 1963-1968 (2007)
8. A. J. Millis, P. B. Littlewood, and B. I. Shraiman, Phys. Rev. Lett., 74, (25) 5144 9(1995)
9. A.J. Millis, Phys Rev. B 53, 8434 (1996)
10. W. Archibald, J.-S. Zhou, J.B. Goodenough, Phys. Rev. B 53, 14445 (1996)
11. C. Zener, Phys. Rev., 82, 403-405 (1951)
12. H. A. Kramers, Physica 1, 182 (1934)
13. H. A. Jahn, E. Teller, Proceedings of the Royal Society of London. Series A, Mathematical and Physical Sciences, 161, 905, 220 (1937)
14. J.B. Goodenough and A. L. Loeb, Phys Rev., 98, 2, 391 (1955)

15. J.B. Goodenough, Phys Rev, 100, 2, 564, (1955)

16. T. Arima, Y. Tokura, and J. B. Torrance, Phys Rev. B, 48, 17, 006 (1993)

17. A. Urushibara, Y. Moritomo, T. Arima, A. Asamitsu, G. Kido, and Y. Tokura, Phys. Rev. B 51, 14 103 (1995)

18. Martin, M., Shirane, G., Endoh, Y., Hirota, K., Moritomo, Y., Tokura, Phys. Rev., 53 (21) 14285-14290 (1996)

19. Y Tokura, A Urushibara, Y Moritomo, T Arima, A Asamitsu, G Kido and N Furukawa, J. Phys. Soc Japan, 63,3931,(1994)

20. A Asamitsu, Y Moritomo, Y Tomioka, T Arima and Y Tokura, Nature, 373, 407 (1995)

21. H Kuwahara, Y Tomioka, A Asamitsu, Y Moritomo, Y Tokura, Science, 270, 961 (1995)

22. L. M. Medarde, J. Cond. Mat. Phys., 9, 1679 (1997)

23. Z. H. Wang, J.W. Cai, B.G. Shen, X. Chen, W.S. Zhan, J. Phys.:Condens. Matter 12, 601 (2000)

24. Ji-Wen Feng, Lian-Pin Hwang, Applied Phys Ltrs, 75, 11,1592 (1999)

25. A. Wold, R. J. Arnott, and J. B. Goodenough, J. Appl. Phys, 29, 387-389 (1958)

26. R. D. Shannon, Acta Crystallogr., Sect. A: Cryst. Phys., Diffr., Theor. Gen. Crystallogr. 32, 751 (1976).

27. J. Rodriguez-Carvajal, FULLPROF 2K, Version 3.00, Laboratoire Leon Brillouin-JRC, 2004

28. Thomas F. Creel, Jinbo B. Yang, Mehmet Kahveci, Jagat Lamsal, Satish K. Malik, S. Quezado, B. W. Benapfl, H. Blackstead, O. A. Pringle, William B.

Yelon and William J. James, MRS Proceedings, 1327 , mrss11-1327-g08-02 doi:10.1557/opl.2011.852 (2011)

29. H. Kawano, R. Kajimoto, M. Kubota and H. Yoshizawa, Phys Rev B, 53, 22, 709 (1996)
30. Jifan Hu, Chengjie Ji, Hongwei Qin, Juan Chen, Yanming Hao, Yangxian Li, J. of Mag. and Mag. Mat. 241, 271 (2002)
31. Y. Tomioka, A. Asamitsu, Y. Moritomo, H. Kuwahara and Y. Tokura, Phys Rev Lett., 74, 25, 5108 (1995)

6. A COMPARATIVE REVIEW OF THE 3D TRANSITION METAL SUBSTITUTED MANGANITE PEROVSKITES

6.1 BACKGROUND

The properties exhibited by the Cr-substituted and Ni-substituted systems are as interesting as they are different. It is informative to review and compare the results of the work presented within this dissertation with studies of other work on *3d*-substituted systems, to include Cr, Fe, Co, Ni and Cu. Of these 3d transition metals, Cr^{3+} has the least occupied outer valence shells and has the same t_{2g} electronic configuration as Mn^{4+}, while Cu has the most filled outer valence shells. Table 6-1 Electronic configuration and neutron scattering lengths for the 3d transition elements compared in this summary.Table 6-1 contains the electronic configuration of all these transition elements along with their neutron scattering lengths. Of note is that the Cr atom base state is high spin, while the Cu atom prefers the low spin, both pulling one electron from the 4s shell to achieve the lowest energy state. The filling of the d-shells in Mn through Ni progresses by filling the d-shell with the additional electron as one moves from left to right in the periodic table. The configurations of these outer valence electrons are at the core of the resultant magnetic interactions observed in these 3d-substituted systems. Neutron scattering lengths of the *3d* elements are sufficiently different, especially considering the uniquely negative scattering length of Mn, that coupled with the neutron magnetic moment, provides neutron scattering the unique ability to accurately determine the nuclear and magnetic structure of these systems. The unique neutron scattering lengths of the elements also allows relatively small amounts of *3d* elements to be accurately located

within the unit cell structure. In sections 6.2 through 6.5, results from other work are combined with data presented within this dissertation, and summarized.

Table 6-1 Electronic configuration and neutron scattering lengths for the 3d transition elements compared in this summary.

	Cr	Mn	Fe	Co	Ni	Cu
Electronic Config.	$(Ar)3d^5 4s^1$	$(Ar)3d^5 4s^2$	$(Ar)3d^6 4s^2$	$(Ar)3d^7 4s^2$	$(Ar)3d^8 4s^2$	$(Ar)3d^{10} 4s^1$
Neutron Scattering Length (fm)	3.635(7)	-3.73(2)	2.49(2)	10.3(1)	7.718(4)	5.680(5)
Most Stable	Cr^{3+}	Mn^{2+}	Fe^{2+}/Fe^{3+}	$Co^{2+}/^{3+}$	Ni^{2+}	Cu^{2+}

All six transition metal substituted $La_{0.7}Sr_{0.3}Mn_{1-x}M_xO_3$ systems where M = Cr, Fe, Co, Ni, and Cu have a metal to insulator transition that occurs around x = 0.2. This is the concentration that was interpreted as the onset of charge ordering within this dissertation. Further, magnetization as a function of temperature for all systems indicated:

- That relative differences between the magnetization saturation values show larger separation between concentrations that undergo transitions in magnetization and conductivity.
- T_C decreases with increasing transition metal content

- M_{ZFC} and M_{FC} curves show transition points with antiferromagnetic characteristic well below T_C that have been interpreted in this dissertation as T_{CO}, the temperature at which charge ordering sets in.

Neutron and x-ray refinements indicate:

- Lattice parameters and cell volume decrease with increasing transition metal content.
- Magnetic moments decrease with increasing transition metal content.
- Unique neutron refinements were presented in this dissertation that interpret the unit cell reflections coincident with a doubling of the c-axis, are not antiferromagnetic reflections, but are instead, a consequence of the amount of charge ordering within each half of a c-axis doubled unit cell.

6.2 SUBSTITUTION OF THE Mn B-SITE BY Cr

The Cr-substituted manganite perovskites exhibit some of the highest T_C's of the manganite perovskite systems. The Cr^{3+} ion has the same electronic configuration as Mn^{4+}, but replaces Mn^{3+} on the B-site, leaving the quantity of Mn^{4+} to be the same as the quantity of Sr^{2+} doped on the A-site in $La_{0.7}^{3+}Sr_{0.3}^{2+}Mn_{0.3}^{4+}(Cr_y^{3+}Mn_{0.7-y}^{3+})O_3^{2-}$. Kallel et al. [1] studied structural, magnetic and electrical properties of $La_{0.7}Sr_{0.3}Mn_{1-x}Cr_xO_3$ using x-ray diffraction, magnetic and electronic measurements. All samples crystalized in the rhombohedral $R\bar{3}c$ space group. Their resistivity measurements indicate a metal to insulator transition at x~0.2. (Figure 6-1) and their magnetization as a function of

temperature indicate T_C decreases with increasing Cr content (Figure 6-2), in good agreement with the Cr-substituted system presented in this dissertation (chapter 4).

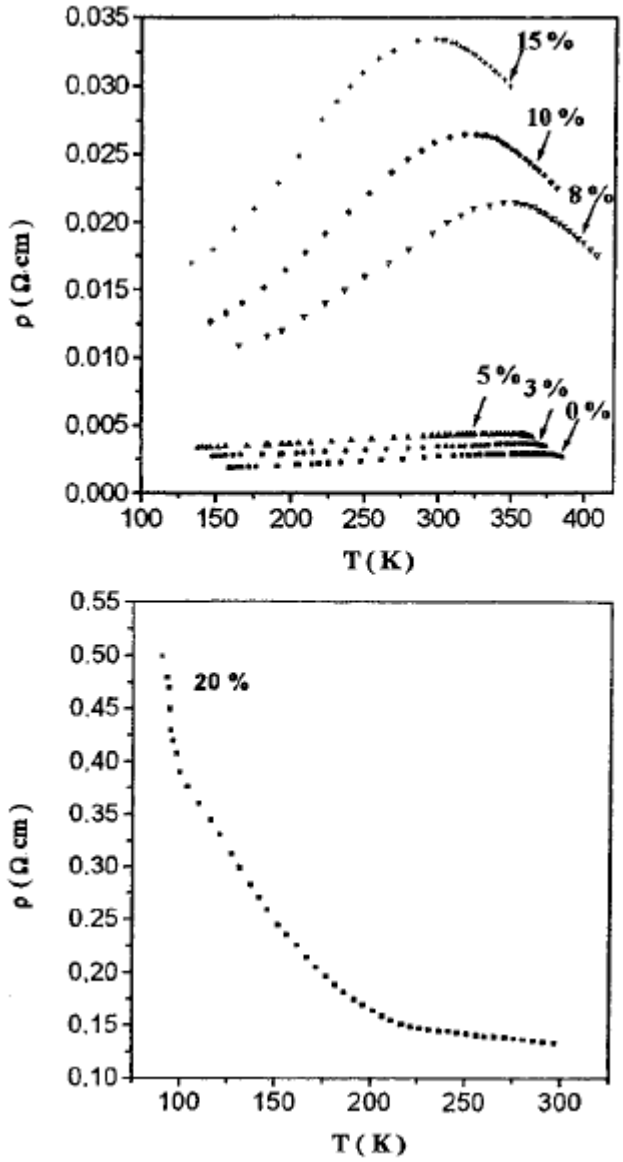

Figure 6-1 Resistivity as a function of temperature from Kallel et al. [1].

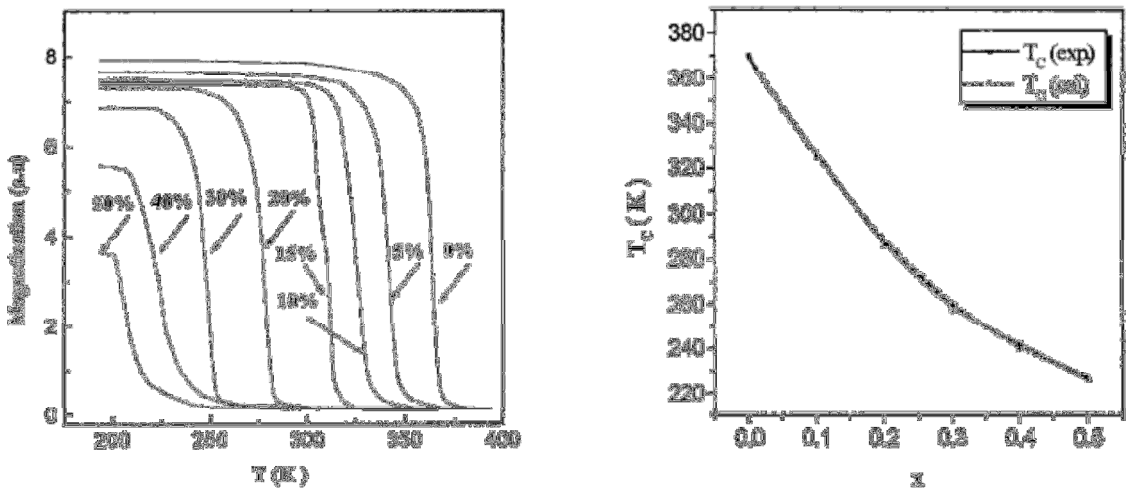

Figure 6-2 Magnetization as a function of temperature and plot of T_C vs Cr concentration from Kallel et al. [1]

6.3 SUBSTITUTION OF THE Mn B-SITE BY Fe

Hernandez et al. [3] and Barandiaran et al. [4] studied $La_{0.7}Sr_{0.3}Mn_{1-x}Fe_xO_3$ ($x \leq 0.3$) by magnetization measurements and Mössbauer spectrometry. They found T_C decreased with increasing Fe and at 4.2K, all samples are ferromagnetic. However, for $x>0.1$, the samples exhibited a combination of ferromagnetic and antiferromagnetic properties similar to those observed in the Cr-substituted systems (Figure 6-3). They also found an increasing local distortion in the MnO_3 octahedral sites with increasing Fe content, and for $x \geq 0.2$, magnetization saturation was not reached in their magnetization vs. magnetic field (Figure 6-4). Their M_{ZFC} and M_{FC} curves show similar behavior to the Cr-substituted systems but with significantly lower T_C transitions (Figure 6-5).

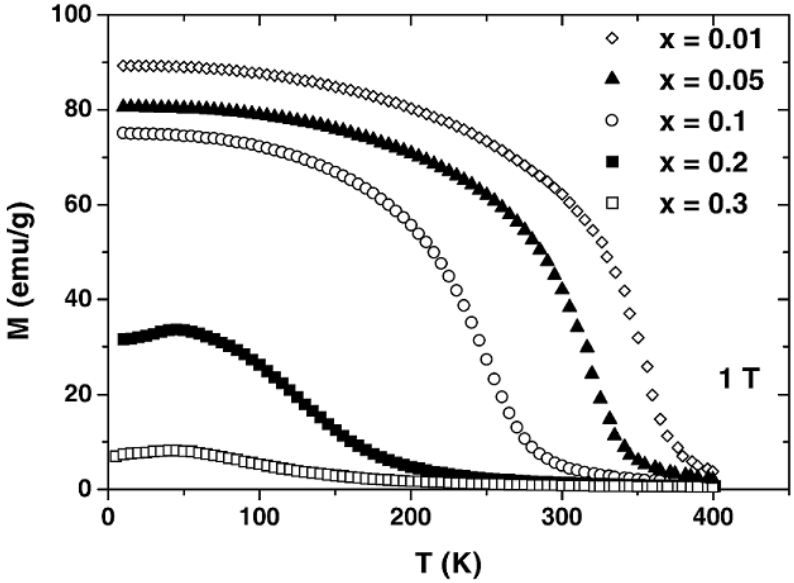

Figure 6-3 Magnetic measurements vs Temperature for $La_{0.7}Sr_{0.3}Mn_{1-x}Fe_xO_3$ from Barandiaran et al. [4].

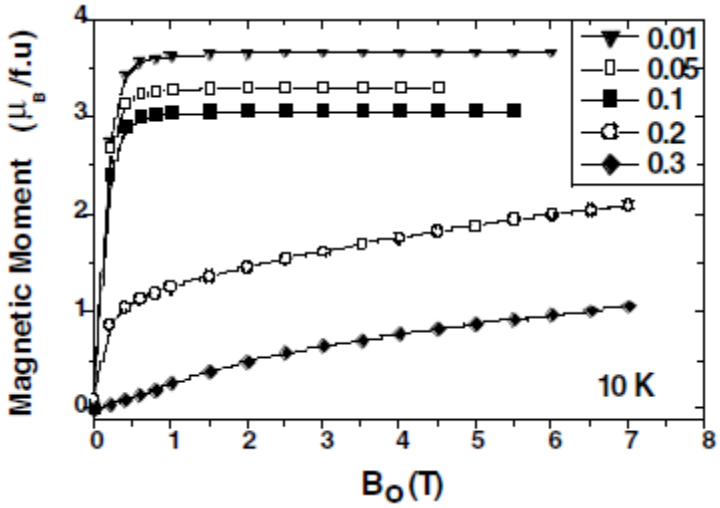

Figure 6-4 Magnetization vs. magnetic field for $La_{0.7}Sr_{0.3}Mn_{1-x}Fe_xO_3$ from Barandiaran et al. [4].

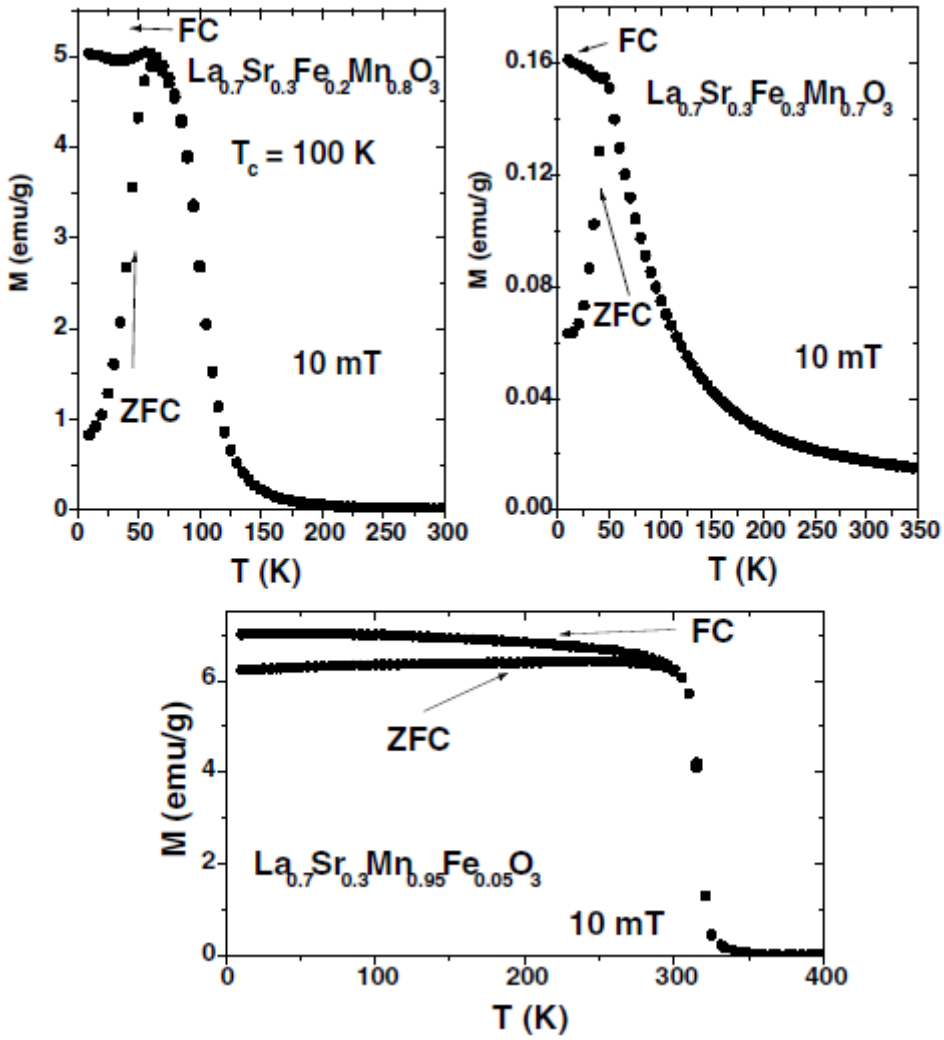

Figure 6-5 Field cooled and zero field cooled measurements for $La_{0.7}Sr_{0.3}Mn_{1-x}Fe_xO_3$ (x=0.05, 0.2 and 0.3) from Barandiaran et al. [4].

Tiwari et al. [5] studied La0.7Sr0.3Mn1-xFexO3 ($x \leq 0.25$) by x-ray diffraction, electrical resistivity, and tunneling conductance measurements. They found Fe to be in the Fe^{3+} state and a semiconductor to insulator transition around x=0.2 (Figure 6-6). Further, they suggested that the Fe^{3+} energy is high enough to prevent it from participating in electron hopping to the Mn^{3+} or Mn^{4+} ions, thus indicating the depletion of hopping electrons with increasing doping of Fe. In the undoped sample (x=0), starting at the high temperatures,

resistivity first increases with decreasing temperature, exhibits a peak at T~Tc) and then decreases as T is further reduced below (see inset of Figure 6-6). As the Fe concentration increases, the resistivity increases and the peak in resistivity moves to a lower T. For $x \leq 0.2$ all the samples show a similar peak in resistivity, characteristic of a metal-insulation transition, and the samples are metallic at lower temperatures. The x=0.25 sample shows insulating behavior throughout the whole temperature range.

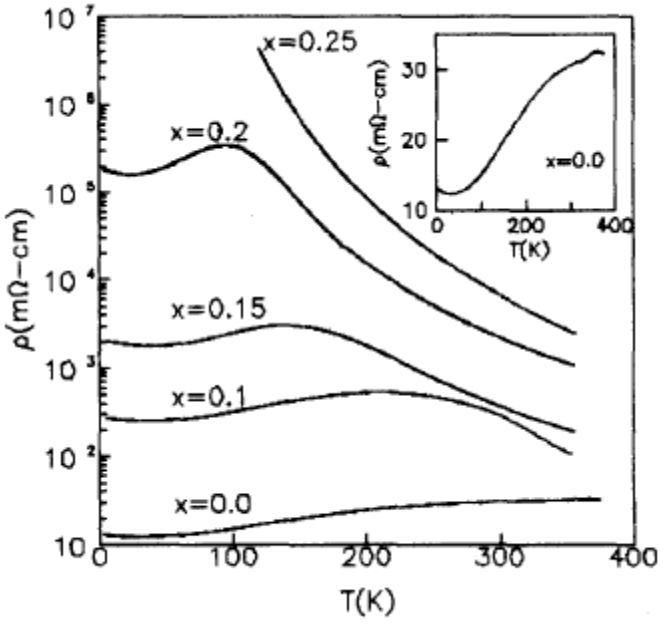

Figure 6-6 Resistivity measurements as a function of temperature from Tiwari et al. [5].

6.4 SUBSTITUTION OF THE Mn B-SITE BY Co

Srikiran et al. [6] studied structural and magnetic properties of $La_{0.7}Sr_{0.3}Co_{1-x}Mn_xO_3$ (x=0.1, 0.5, 0.75 and 0.9) by neutron diffraction and magnetic measurements.

Their samples were prepared by the solid state method and crystalized in the rhombohedral $R\bar{3}c$ space group. Magnetic moments from magnetic measurements of 0.4, 0.81, 2.6 and 3.25 μ_B for x=0.1, 0.5, 0.75 and 0.9 respectively, was in good agreement with their neutron data.

Their magnetization as a function of magnetic field (Figure 6-7) indicate saturation was not reached in samples with x>0.1 and decreased with increasing Co content. T_C decreases with increasing Co content and there is evidence of antiferromagnetic-like transitions well below T_C for x≤0.5, similar to that observed in the other transition metal systems (Figure 6-8).

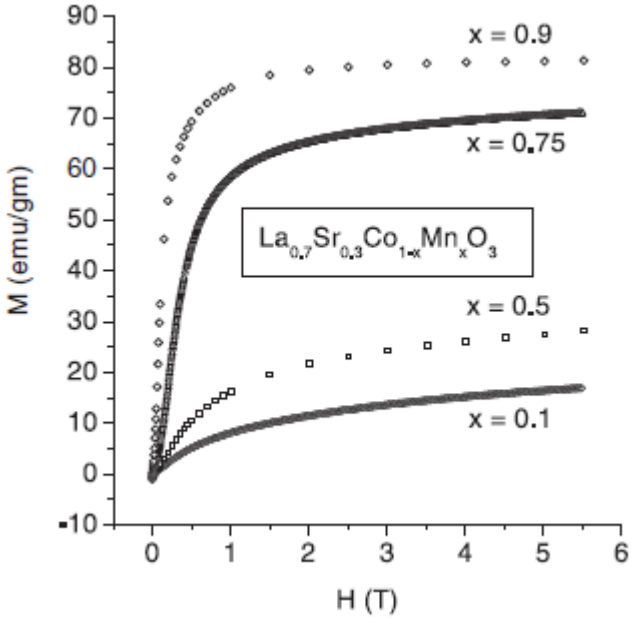

Figure 6-7 Magnetization as a function of magnetic field from Srikiran et al. [6]

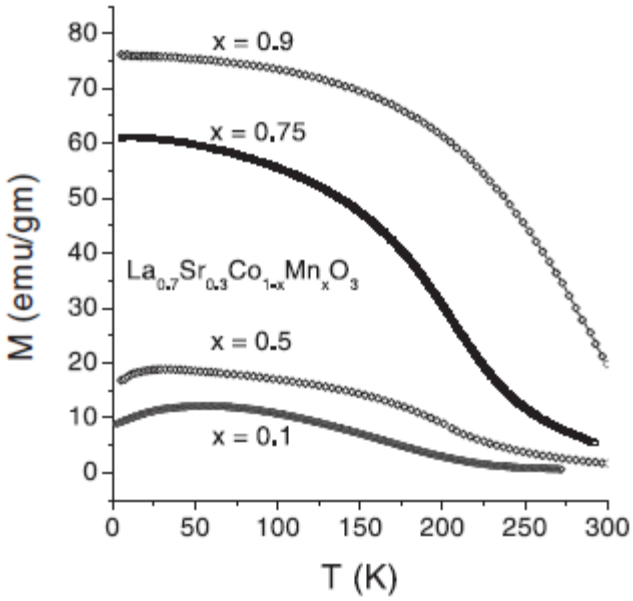

Figure 6-8 Magnetization as a function of Temperature from Srikiran et al. [6].

Zhao et al. [7] studied $La_{0.7}Sr_{0.3}Mn_{1-x}Co_xO_3$ ($0 \leq x \leq 0.5$) by x-ray powder diffraction and magnetic measurements. Their samples were prepared by the solid state method and crystalized in the $R\bar{3}c$ space group. Magnetization decreased with increasing Co content, 5.70, 5.48, 3.45, 2.67, and 0.00 for x=0, 0.01, 0.10, 0.20, 0.30, and 0.5 respectively For x≥0.3, the paramagnetic metal to ferromagnetic metal transition disappears and the temperature dependence of the resistivity follows semiconducting behavior with another transition to insulating behavior at x=0.5 (Figure 6-9). For samples with x=0.1 and 0.3, magnetoresistance effects are enhanced as compared with the undoped parent. However, for x=0.5, the magnetoresistance effect is suppressed. For x≥0.3, hysteresis is observed in the magnetization vs magnetic field measurements (Figure 6-10).

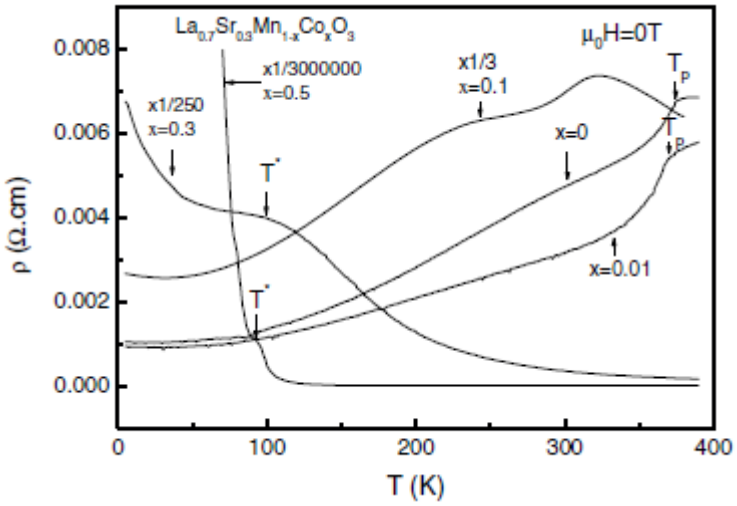

Figure 6-9 Resistivity as a function of temperature from Zhao et al. [7].

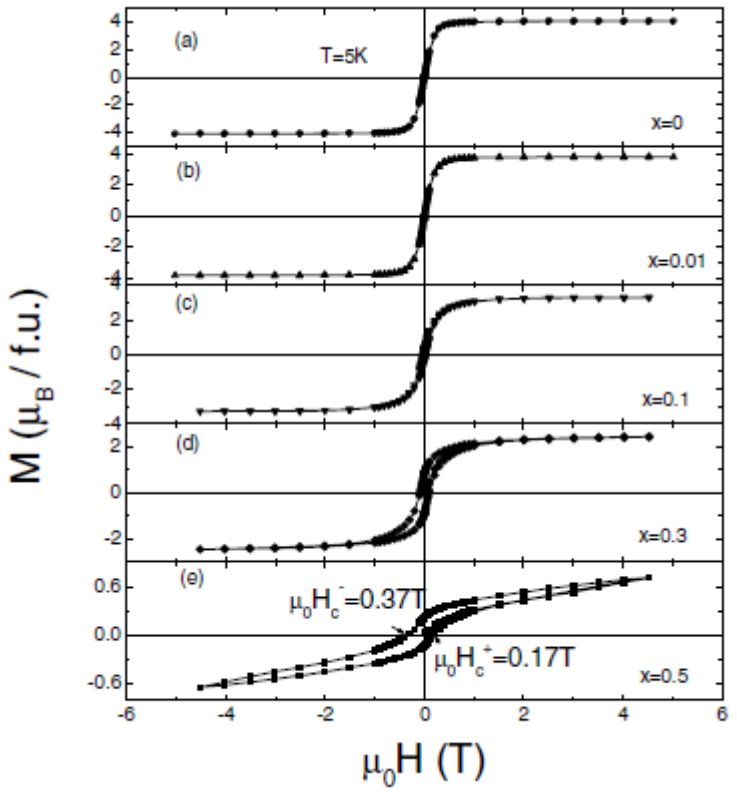

Figure 6-10 Magnetization as a function of magnetic field from Zhao et al. [7].

6.5 SUBSTITUTION OF THE Mn B-SITE BY Ni

The Ni-substituted system has been reported as having Ni in the Ni^{2+} and Ni^{3+} states [8, 9]. In this dissertation, we presented data for the $La_{0.7}Sr_{0.3}MnO_3$ system where Mn was replaced with up to 40% Ni and analyzed with neutron scattering, x-ray scattering and magnetic measurements to determine the nuclear and magnetic structure and magnetic properties of this Ni-substituted perovskite. The atomic parameters (a, c and volume) decrease with increasing Ni content while the oxygen stoichiometry changes very little. The decreasing cell parameters combined with the constant oxygen stoichiometry indicate Ni to be in the Ni^{3+} state. If Ni were in the Ni^{2+} state, one would expect the volume to increase, given stoichiometric oxygen. The replacement of Mn^{3+} by Ni^{3+} drives the system from a ferromagnet to an antiferromagnet. Neutron data for low Ni concentrations indicate the system is ferromagnetic with the Ni^{3+} moments aligned antiferromagnetically to the Mn^{3+} and Mn^{4+} moments, causing a net reduction in the measured ferromagnetic moments. This is unlike the Cr-substituted system where the Cr^{3+} aligned ferromagnetically to Mn^{3+} and antiferromagnetically to Mn^{4+}. At x=0.21, the neutron data (Chapter 5) indicate unequal but aligned magnetic moments, providing for a charge ordered ferromagnet. For $x \geq 0.31$, the interaction between adjacent planes (Chapter 5) changes to antiferromagnetic where the Ni^{3+} moments are antiparallel to the Mn^{3+} and Mn^{4+} moments. These last two results are similar to those observed in the Cr-substituted system, except they occur over a much narrower range of transition metal content; likely due to the nearly complete d-shell electrons. As the Ni concentration grows, the antiferromagnetic Ni^{3+}-O-Ni^{3+} superexchange interaction becomes

increasingly important and more probable, ultimately resulting in the reversing of the orientation between the B1 and B2 layers at $x \geq 0.31$, creating an antiferromagnetic system.

Feng et al. [10] studied $La_{0.7}Sr_{0.3}Mn_{1-x}Ni_xO_3$ (x = 0.05, 0.10, 0.15, 0.18, 0.20, 0.25, 0.30, and 0.40). They find a metal to insulator transition near x=0.20 (Figure 6-11), a Ni concentration coincident with the reported (Chapter 5) onset of charge ordering, also an insulating state. Their magnetization as a function of temperature with several different magnetic fields applied, are presented in Figure 6-12. The arrow and vertical line indicate T_C and resistivity peak, respectively. For $x \leq 0.05$, the metal to insulator transition occurs near T_C. However, for $0.1 \leq x \leq 0.2$, the peak in resistivity occurs at a temperature well below T_C, and decreases in temperature with increasing Ni content. No resistivity peak is observed for $x \geq 0.20$, indicating insulating behavior only.

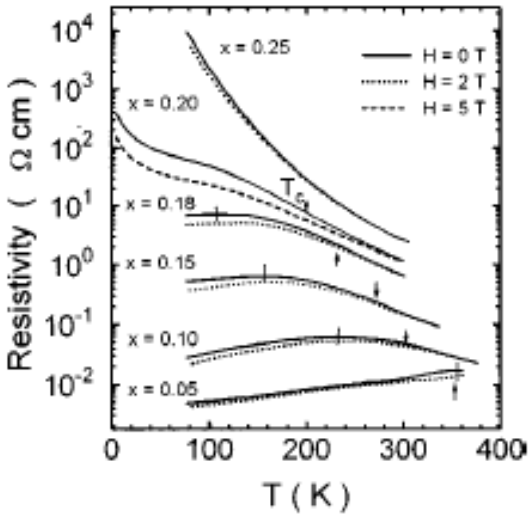

Figure 6-11 Resistivity as a function of temperature from Feng et al. [10]

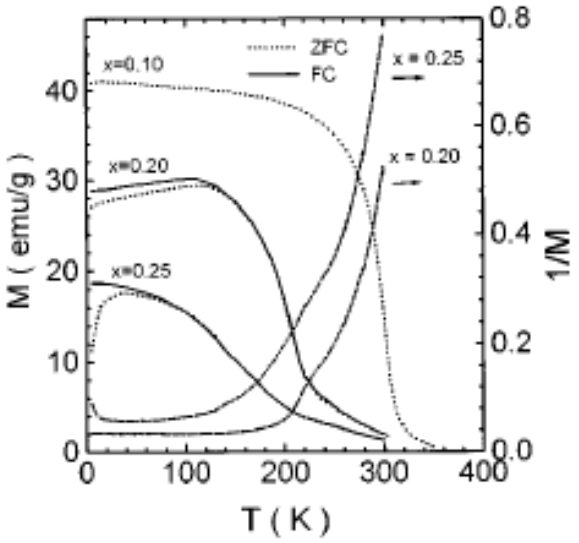

Figure 6-12 Magnetization (M) as a function of temperature from Feng et al. [10].

6.6 SUBSTITUTION OF THE Mn B-SITE BY Cu

Kim et al. [11] studied $La_{0.7}Sr_{0.3}Mn_{1-x}Cu_xO_3$ ($0 \leq x \leq 0.20$) by neutron diffraction, magnetic measurements and magnetoresistance measurements. They prepared their samples using the conventional solid state reaction method and all samples crystalized in the rhombohedral structure, $R\bar{3}c$ space-group. Table 6-2 contains the structural and magnetic parameters from the neutron refinements. This system shows no sign of antiferromagnetic couplings between Cu^{3+} and Mn ions. The x = 0.15 sample shows evidence of both copper ions, Cu^{3+} and Cu^{2+}, unlike the other transition metal-substituted systems. This will affect the exchange mechanisms and magnetic interactions in this system and is observed through the reduction in ferromagnetic moments with

increased Cu content. This indicates a likely reduction in the Mn^{3+}-O-Mn^{4+} ferromagnetic double exchange interactions, a direct result of the reduction in Mn^{3+} ions.

The field cooled (M_{FC}) and zero field cooled (M_{ZFC}) magnetization versus temperature measurements are provided in Figure 6-13. The T_C decreases with increased Cu^{3+} content. While the signature separation between the M_{ZFC} and M_{FC} curves is present, the complex curves observed in the other 3d-substituted systems is only weakly observable in the x=0.15 sample and only in the M_{ZFC} curves. This indicates there may be antiferromagnetic ordering up to 50K that is too small to be observable within the resolution of the neutron diffraction analysis.

Electric resistivity versus temperature from Kim et al. [11] for $La_{0.7}Sr_{0.3}Mn_{1-x}Fe_xO_3$ with (x = 0.10, 0.15, and 0.20) samples are shown in Figure 6-14. An applied magnetic field suppresses the resistivity of all samples over the entire temperature range. For $x \leq 0.10$, conducting behavior is observed that decreases with increased temperatures. All samples show a similar peak in resistivity, characteristic of a metal-insulation transition, and the samples are metallic at lower temperatures. A metal-to-insulator transition occurs $0.15<x<0.20$ and the system is a strong insulator at x=0.20.

Table 6-2 Refined parameters for $La_{0.7}Sr_{0.3}Mn_{1-x}Cu_xO_3$, $R\bar{3}c$ space-group, at room temperature and 10K from Kim et al. [11]. Numbers in parentheses are statistical error. A and c are the unit cell parameters, V is the volume, M is the magnetic moment, χ^2 is $[R_{wp}/R_{exp}]^2$ where R_{wp} is the residual error of the weighted profile. The magnetic moments of the $x \geq 0.15$ samples at RT are not refined.

Composition (x)	0.00	0.05	0.10	0.15	0.20
T = 300K					
a ($\AA$)	5.5038(2)	5.5003(2)	5.4987(2)	5.4982(2)	5.4941(2)
c ($\AA$)	13.3552(5)	13.3387(4)	13.3341(5)	13.3304(6)	13.3180(6)
V ($\AA^3$)	350.351(18)	349.473(17)	349.153(18)	348.990(22)	348.152(24)
μ_B	2.512(28)	1.975(30)	1.411(101)	-	-
χ^2 (%)	2.81	2.69	2.91	4.89	5.36
T = 10K					
a ($\AA$)	5.4812(1)	5.4845(1)	5.4823(1)	5.4858(1)	5.4855(2)
c ($\AA$)	13.2759(3)	13.2797(4)	13.2737(4)	13.2718(4)	13.2637(4)
V ($\AA^3$)	345.415(13)	345.931(16)	345.504(17)	345.897(17)	345.642(17)
μ_B	3.445(24)	3.327(27)	3.160	2.272(50)	0.727(93)
χ^2 (%)	3.18	2.76	3.30	2.67	2.82

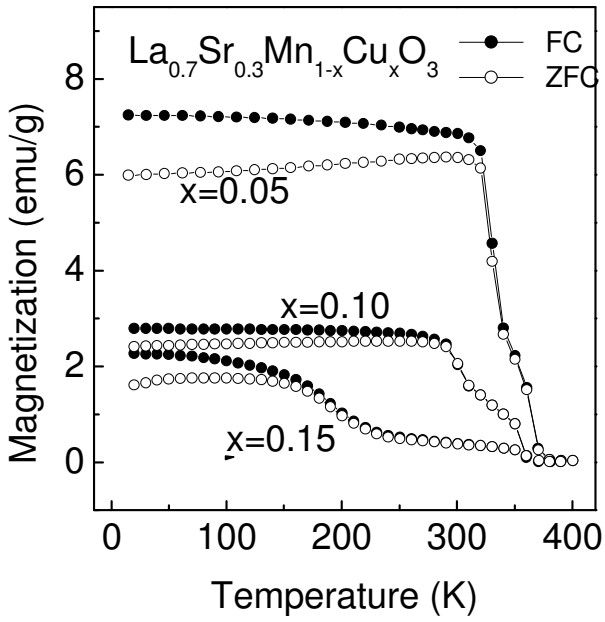

Figure 6-13 Zero field-cooled (M_{ZFC}) and 50 Oe field-cooled (M_{FC}) measurements of magnetization vs temperature for all Cu concentrations for $La_{0.7}Sr_{0.3}Mn_{1-x}Cu_xO_3$ (x = 0.05, 0.10, 0.15) from Kim et al. [11].

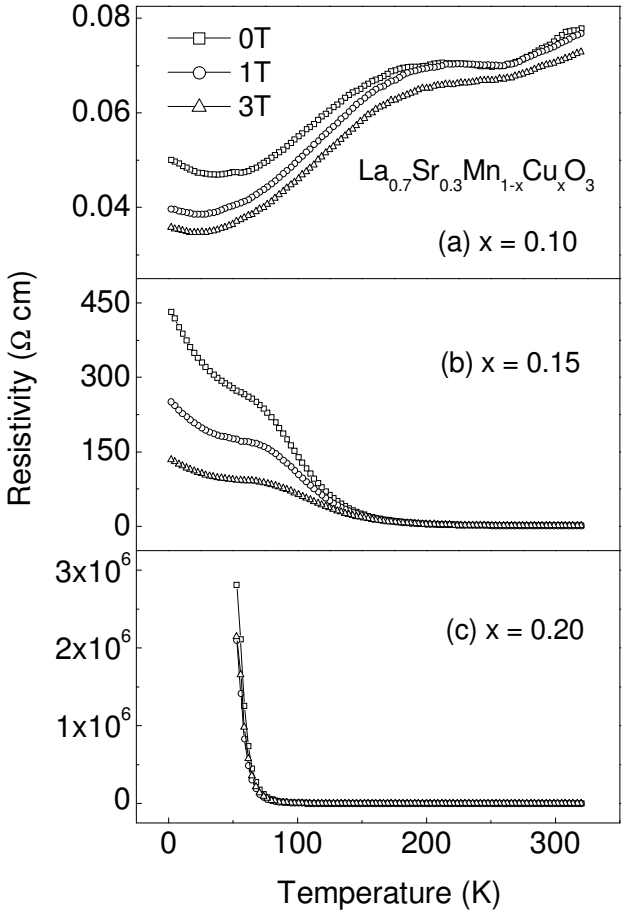

Figure 6-14 Electric resistivity versus temperature for $La_{0.7}Sr_{0.3}Mn_{1-x}Cu_xO_3$ (x = 0.10(a), 0.15(b), 0.20(c)) in applied magnetic field H = 0, 1, 3, 5T from Kim et al. [11].

6.7 SUMMARY AND CONCLUSIONS

Of the six transition metal-substituted systems, the Cr-based system presented some of the most interesting magnetic properties, followed by the Ni-based system and, finally, the Cu-based system. All systems exhibit layered magnetic behavior, a reduction in ferromagnetism with increasing transition metal content, complex magnetic interactions well below T_C, and a metal to insulator transition around x~0.2 (a value also

near the percolation threshold described in many works of around x~0.16). Looking across the unpaired valence electrons of the eight different transition metal ions, Cr^{3+} $(Ar)3d^3 4s^0$, Mn^{3+} $(Ar)3d^4 4s^0$, Mn^{4+} $(Ar)3d^3 4s^0$, Fe^{3+} $(Ar)3d^5 4s^0$, Co^{3+} $(Ar)3d^6 4s^0$, Ni^{3+} $(Ar)3d^7 4s^0$, Cu^{3+} $(Ar)3d^8 4s^0$, all of the 3d transition metal-substituted systems indicate the metal ions replace Mn^{3+} in a like-ionic state except for the Cu-substituted system where Cu^{2+} and Cu^{3+} (dominant species) were both observed. Copper has the highest atomic number with nearly full s and d-shells, and therefore, is more likely to not give up electrons to participate in magnetic interactions. On the other hand, Cr has the lowest atomic number and prefers to exist in the high spin state ($(Ar)3d^5 4s^1$), with Cr^{3+} having three unpaired electrons to participate in magnetic interactions. As noted above, the Cr^{3+}, Mn^{3+}, Mn^{4+}, Fe^{3+}, Co^{3+} Ni^{3+} and Cu^{3+} transition metal ions have 3, 4, 3, 5, 6, 7 and 8 d-electrons respectively. The five-fold d-orbital degeneracy is split by the cubic environment into two terms, t_g^2 and e_g^2. The t_g^2-level contains three electrons that form the so-called "t-core". The last two d-electrons (e_g^2-electron) are well separated in energy and form a loosely bound state (see Fig. 1.2). The double degenerate e_g^2 electrons play a key role in magnetization, conducting and other properties of manganites. The Hund's rule requires that the three d-electrons forming the t_g^2 -level have the same spin-orientation, and due to strong Coulombic forces, results in the localization of the t_g^2electrons that have a total spin of S = 3/2. The e_g^2 electrons are also affected by the same strong Hund's interaction. Therefore, their spin must be polarized along the same direction as for the t_g^2 electrons. The Mn^{4+} ion can lose its e_g^2 electron, thereby creating a hole that is spread over the unit cell and shared by six near neighbor transition metal ions. In low concentrations, localization of this hole provides the formation of local polarons

and an insulating state. With the addition of more holes from the substituted transition metal ions, conducting and ferromagnetic states appear. As the temperature is increased, T_C is reached and the respective systems make the transition to the paramagnetic state, accompanied by a much higher resistivity. There appears then, to be a correlation between the electronic properties and magnetization.

As discussed in Chapter 1, Zener presented the double exchange mechanism as a means to describe the movement of electrons in these systems. The double exchange mechanism is one whereby the oxygen ion mediates a transfer of an electron between the Mn^{3+} ion and the Mn4+ ion as described by Mn^{3+} -O- Mn^{4+}. Thus, another e_g^2-electron, initially localized, can become mobile and promote conduction. However, as was noted above, the e_g^2-electron is spin-polarized because of the Hund's rule with its respective t_g^2 electrons. The total spin of a complete t_g^2 core is equal to S=3/2, but their mutual orientations may be different for differerent sites. Relative orientation of spins of the e_g^2-electrons and any "vacant" t_g^2 electrons are important, as the hopping is forbidden if the spin directions are the same. This hopping provides an increase in the ground state kinetic energy of the ferromagnetically ordered system (all spins are polarized along one direction) but lies below the paramagnetic state (witnessed by the temperature dependency of T_C). As a result, the t_g^2 electrons become ferromagnetically coupled, favoring the hopping of the e_g^2-electrons (spin polarized conduction) and linking the electronic and magnetic behavior of these systems. The behavior of each of these systems is then governed mainly by the quantity, or lack thereof, of mobile, unpaired electrons in the doubly dengenerate e_g^2 band with orientation constrained by the t_g^2 electrons.

The Cr and Ni systems (from this dissertation) at low temperature suggest transitions with increased transition metal content from ferromagnetic to unequal but aligned magnetic moments within a doubled c-axis unit cell. The Cr-substituted system follows with another transition to unequal and anti-aligned magnetic moments within the same c-axis doubled unit cell, forming a ferrimagnet. However, the Ni system transitions from unequal but aligned magnetic moments within the c-axis doubled unit cell to to an antiferromagnet while the Cr system never fully achieves this transition. The Cr^{3+} moment aligns parallel to the Mn^{3+} and Mn^{4+} moments, replacing Mn^{3+} in the oxygen octahedron but ordering antiferromagnetically to Mn^{4+} while ordering feromagnetically to Mn^{3+}. This ordering appears to be unique to the Cr-based system. This level of analysis was not performed on the Fe, Co and Cu systems, but is recommended. Near the metal to insulator transition for the Ni and Cr systems, the magnetic data exhibited transition points with antiferromagnetic character well below T_C. Charge ordering is well known in these manganites, with the clearest evidence when the amounts of disparate charges are equal (e.g. Mn^{3+}=Mn^{4+}). Other studies have confirmed that charge ordering exists outside these equivalent quantities and have suggested there may be "nodal" compositions such as x=1/4 or x=1/8. Our data for the Ni and Cr systems strongly suggest the onset of charge ordering occurs coincident with the metal to insulator transition, and not only at specific nodal quantities. We suggest this type of ordering is highly likely in the remaining transition metal-substituted systems, but that additional analysis with neutron data is needed. Further, the ionic species that has consistently been replaced by the 3d transition metal ions within these systems are the Mn^{3+} ions. The Mn^{3+} ion is a Jahn-Teller distorted ion with an unpaired outer e_g electron that provides for

conductivity. It is this e_g ion coupled with the ionic size constraints of the system that governs the magnetic and electronic properties of these systems.

APPENDIX A: PROPERTIES OF NEUTRONS AND X-RAYS

X-rays and neutrons are both routinely used to study nuclear structure of materials. Some properties of x-rays, neutrons and electrons are provided in Table 1. X-rays are electromagnetic radiation with wavelengths on the order of 1Å (10^{-10}m) and wavelengths between 0.5 and 2.5Å are typically used in crystallography. The x-ray wavelength used in this thesis is that of the K-shell of copper, Kα = 1.54 Å. X-rays interact with the electronic charge, and hence heavy atoms with many electrons (such as mercury) scatter x-rays much more efficiently than light atoms such as oxygen or hydrogen with just a few electrons. Therefore, x-rays cannot be used to determine the position of these atoms.

	Neutron	X-rays	Electron
Mass	Mn = 1.675×10^{-27}kg	0 (rest mass)	Me = 9.109 x 10^{-31} kg (rest mass)
Charge	0	0	e
Spin	S = ½	1	S = ½
Magnetic Dipole Moment	$* \mu_n = (-e\hbar)/(2m_n)g_n s_n = -1.913\mu_n$	0	$* \mu_e = (-e\hbar)/(2m_e)g_e s_e$
Energy	E =	$E=mc^2=hf=h$	E =

	$(\hbar^2k^2)/(2m_n)$	$c/\lambda=pc$	$(\hbar^2k^2)/2m_e)$
Energy	~5meV to 100meV for thermal neutrons	~1KeV to 10KeV	~ 511KeV (using the rest mass)
Coulomb Interaction	No	Yes	Yes
Mag. Dipole-Dipole Interaction	Yes	Yes	Yes
Strong-force (nuclear) interaction	Yes	No	No

Table 1: Properties of neutrons, x-rays and electrons where $k=2\pi/\lambda$, $g_n = 3.826$, $g_e = 2.0$.

Neutrons have no charge and do not experience the coulomb interaction, but do have a magnetic moment and penetrate deep into the atom, scattering off the nucleus and, for magnetic materials, off unpaired electrons. Thus, neutrons are considered a bulk probe, well suited for low-energy excitations such as lattice vibrations and spin waves with energies in the meV range.

Neutrons from a nuclear reactor operating at temperature T will come into thermal equilibrium with the reactor cooling pool before being allowed to escape with a root-mean-square velocity *v* given by

$(1/2)mv^2=(3/2)kT$,

where *k* is boltzmann's constant. They will also have a Maxwellian flux distribution (Figure 2) of

$$\varphi(v) \propto v^2 e^{\left(-\frac{\frac{1}{2}mv^2}{k_B T}\right)},$$

where φ(v) is the number of neutrons through a unit area per second.

Figure (2)

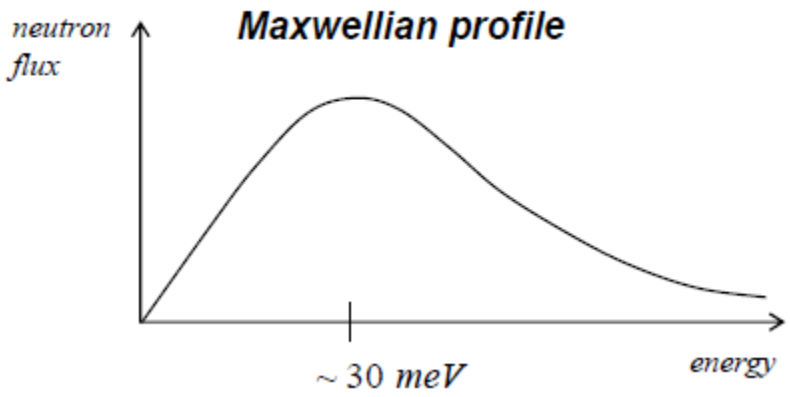

Therefore, it follows that

$\lambda^2=h^2/(3mkT)$.

Using this formula, neutrons at equilibrium temperatures of 0˚C and 100˚C have wavelengths of 1.55 Å and 1.33 Å respectively.

Wave Nature of Neutrons

The scattering cross-section ($\frac{d\sigma}{d\Omega}$) of the nucleus is equivalent to the effective area presented by the nucleus to the passing neutron or,

$\sigma = \frac{Outgoing\ current\ of\ scattered\ neutrons}{incident\ neutron\ flux}$, so that

$\frac{d\sigma}{d\Omega}$ = # of neutrons scattered into a solid angle element dΩ per unit time

For a single nucleus, the size is very small compared to the wavelength of the neutron and it can be considered as a point scatterer such that

$\frac{d\sigma}{d\Omega} = \left| b \right|^2$,

and the total cross section will be

$\sigma = \int \frac{d\sigma}{d\Omega} d\Omega = 4\pi b^2$.

Thus, the cross section, σ, is an area while b is the scattering length as if the scattering length were half the radius of the nucleus as seen by the neutron.

A plane wave of neutrons can be described by a wave function

$$\Psi(\mathbf{r})=(1/\sqrt{Y})e^{(i\mathbf{k}_i\cdot\mathbf{x})},$$

where Y is the normalization constant, $\bar{\mathbf{k}}$ is the neutron wave vector with wave-number $k=2\pi/\lambda$, the magnitude of the wave vector**.** When the wave of neutrons hits the nucleus of the atom, the scattering will be spherically symmetric such that the scattered wave function can be written as

$$\Psi=(-b/\mathbf{r})e^{(i\mathbf{k}_i\cdot\mathbf{x})},$$

where b is defined as the scattering length and has both an imaginary and real component.

$$b \equiv \alpha+i\beta.$$

However, the imaginary component is only important for materials that have a high neutron absorption coefficient such as boron or cadmium. Therefore, the necessary component for this thesis will be the real component, leading to

$$\Psi= e^{(ikz)} - (-b/r)e^{(ikr)}.$$

The spherical wavefronts of the scattered neutron are represented in Figure 2 as circles spreading out from the nucleus while the incoming wavefronts are depicted as the vertical lines and represent the nodes of the wave (the points at which the phase $\overline{\overline{k}} \cdot \overline{r}$.

Figure 2 – A neutron in the form of a plane wave is scattered by a single fixed nucleus. The scattered wave

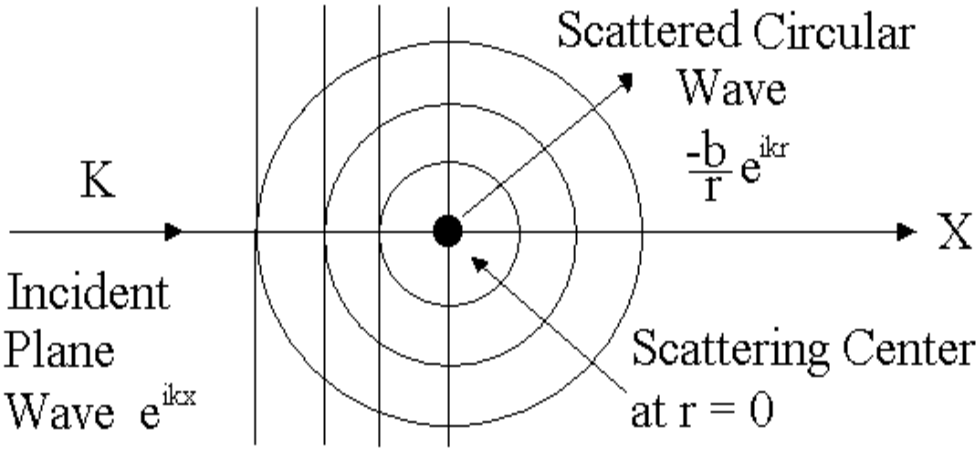

APPENDIX B: NEUTRON SCATTERING COLLECTION FACILITIES

University of Missouri Research Reactor (MURR)

All neutron-diffraction data were collected at the MURR facility (Figure 2) using a position sensitive detector diffractometer with a neutron wavelength of λ = 1.479Å. MURR houses a tank-type nuclear research reactor, servicing the University of Missouri's Nuclear Science and Engineering Institute (NSEI) in Columbia. As of March 2012, the MURR is the highest power university research reactor in the U.S., providing 10 megawatts of thermal output. The first small angle neutron scattering (SANS) spectrometer in the U.S. was installed in 1980. The power of neutron scattering comes from the unique neutron properties, such as charge neutrality (allowing relatively deep penetration of materials), a magnetic moment (allowing investigation of magnetic properties at the microscopic level), and a high probability for interacting with light elements such as hydrogen that can't be observed with x-ray scattering techniques (allowing investigation of organic materials). The powder diffractometer is located within the MURR facility at beam port D. The design of this diffractometer is different from other conventional constant wavelength diffractometers. In conventional diffractometers, the neutrons are ran through Söller collimators to align the directions of the neutrons (scattering vector $Q=2k\sin\theta$ is constant since k and θ are fixed) and then ran through a crystal monochromator to select the wavelengths of neutrons. One such diffractometer is the ECHIDNA powder diffractometer at the Open-pool (OPAL) Australian lightwater reactor. At OPAL, directions of the incoming and outgoing wave vector, $Q=2d\mathrm{Sin}(\theta)$, are chosen by two Söller Collimators. The monochromator is comprised of slabs of

germanium crystals inclined towards each other in order to focus down the Bragg reflected beam. A secondary collimator can optionally be placed in the monochromated beam between the monochromator and the sample, increasing the resolution of the instrument.

In contrast, the MURR diffractometer incoming monochromatic beam is chosen by a double focusing bent perfect silicon crystal monochromator. Compared with the conventional diffractometer, the intensity of the neutrons reflected by the monochromator at MURR is higher and, due to the low scattering power of the silicon monochromator for fast neutrons and its low incoherent scattering, have reduced background intensity. Also, conventional diffractometers use multi-detectors whereas the MURR diffractometer uses five linear, position sensitive detectors, located 160 cm away from the sample position, measuring the intensity in 20° (2θ) segments. The detectors can be incrementally moved, usually in 0.5˚ steps, to cover the entire scattering angle, often 5°-105° (2θ). Each detector consists of linear positive sensitive proportional chamber(outer wall is the cathode) made of stainless steel tubing one inch in diameter and 24 inches long, located in a moveable neutron shield assembly. A spring-tensioned, 8kΩ resistance wire is connected between the two ends of the tube, forming the anode. Each detector, in tube-form, contains a 2:1 ratio of helium and argon gas, with about 5% carbon-dioxide gas.

Figure 2 – University of Missouri Research Reactor (MURR) Beam Port Floor Layout of Instrument Facilities. Beam port D provides the neutrons for the High Resolution Powder Diffractometer.

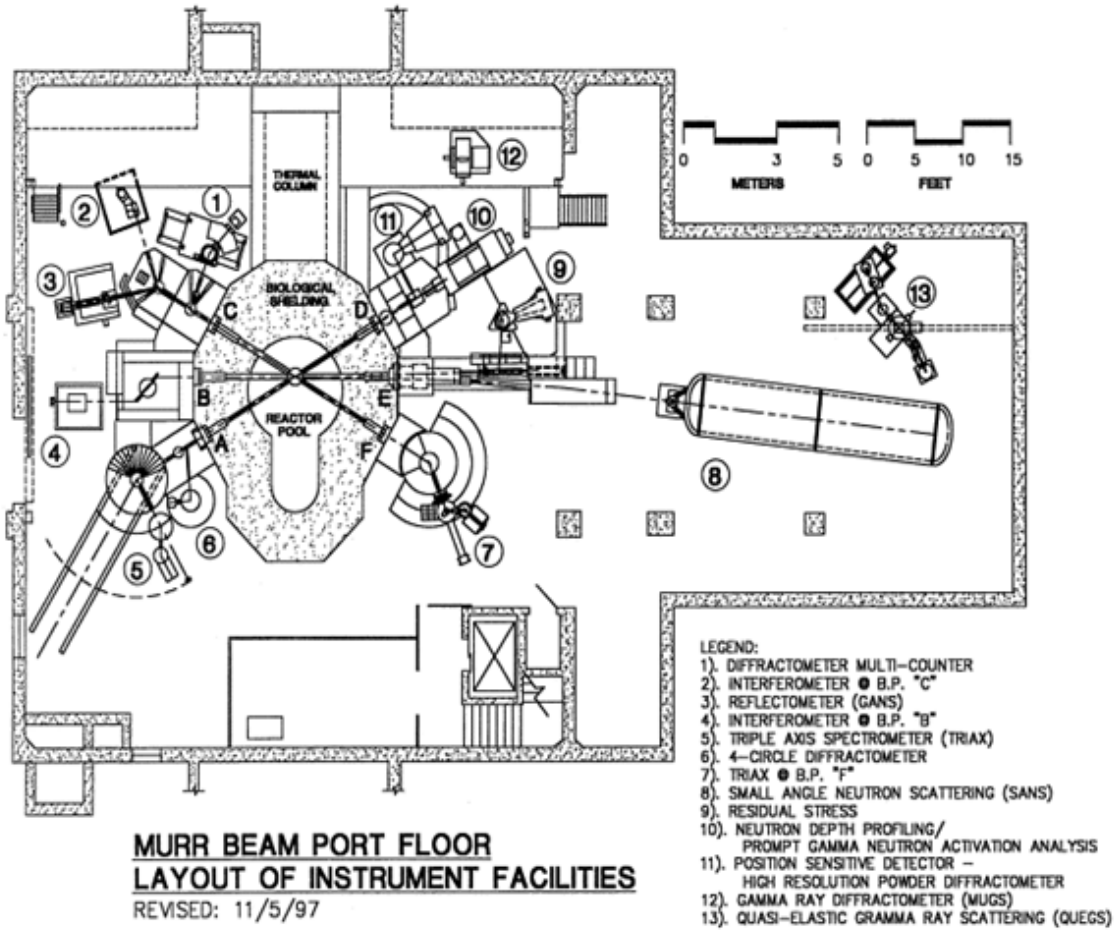

At the MURR diffractometer, the background intensity of neutrons is reduced by the oscillating collimator placed in front of the detectors and behind the sample. This collimator allows only the neutrons scattered from the sample to reach the detectors, greatly reducing the amount of neutrons scattered from atoms in the background. The amount of sample required for the neutron diffraction measurement is about one gram and is held in a small Vanadium sample holder, a tube about 3 inches long and 3

millimeters in diameter. The tube is loaded in the sample exchanger and rotates about the long axis to average out any preferred orientations. The neutron diffraction measurement can be performed in the temperature range from 10K to 450K (300K without the furnace room). The low temperature is achieved using a cryogenic closed cycle refrigerator.

APPENDIX C: IONIC CONFIGURATION OF Cr-SUBSTITUTED $La_{0.7}Sr_{0.3}MnO_3$

To find the ionic configuration of Cr doped $La_{0.7}Sr_{0.3}MnO_3$, let α be the amount of oxidized Cr^{3+} and subsequently, the amount of reduced Mn^{3+} on the same site. The ionic formulation is then,

$$La_{0.7}^{3+}Sr_{0.3}^{2+}(Mn_{0.7-\alpha}^{3+}Mn_{0.3}^{4+})(Cr_{\alpha}^{3+})O_3^{2-}$$

Applying charge balance on this expression we find;

$$3(0.7)+2(0.3)+3(0.7-\alpha)+4(0.3)+3\alpha-6=0,$$

$$2.1+0.6+2.1-3\alpha+1.2+3\alpha=0,$$

The complication that is often incurred is that oxygen stoichiometry is often hard to maintain in these compounds, leaving instead, $O_{3+/-\delta}^{2-}$ in lieu of O_3^{2-}. The excess or reduced amount of oxygen then will modify the amount of oxidized 3d transition element. Although the ionic radius of the different transition elements can be considered when trying to determine which ion of which element is present, more often it is required to determine which ions are present through experimentation.

BIBLIOGRAPHY

1. N. Kallel, J. Dhahri, S. Zemni, E. Dhahri, M. Oumezzine, M. Ghedira, and H. Vincent, Phys. Stat. Sol., (a) **184**, 2, 319 (2001)
2. O.Z. Yanchevskii, O. I. V'yunov, and A. G. Belous, Low Temperature Physics, **32**, 2, 134 (2006)
3. T. Hernandez, F. Plazaola, T. Rojo J.M. Barandiaran, J. All. Comp., **323-324**, 440 (2001)
4. J. M. Barandiaran, J. M. Greneche, T. Hernandez, F. Plazaola and T. Rojo, J. Cond. Mat. Phys, 14, 12563 (2002)
5. A. Tiwari and K. P. Rajeev, J. of App. Physl, 86, 9 5175 (1999)
6. J. S. Srikiran, A. Das, P.L. Paulose, S.K. Paranjpe, Appl. Phys., A **74**(suppl.) S814 (2002).
7. B.C. Zhao, W.H. Song, Y.Q. Ma, R.L. Zhang, J. Yang, Z.G. Sheng, W.J. Lu, j.M. Dai, and Y.P. Sun Phys. Stat. Sol. (b) **242**, 8 1719 (2005).
8. Z. H. Wang, J.W. Cai, B.G. Shen, X. Chen, W.S. Zhan, J. Phys.:Condens. Matter **12**, 601 (2000).
9. A. Wold, R. J. Arnott, and J. B. Goodenough, J. Appl. Phys, **29**, 387 (1958).
10. Ji-Wen Feng, Lian-Pin Hwang, Applied Phys Ltrs, **75**, 11,1592 (1999)
11. M. S. Kim, J.B. Yang, and P.E. Parris, J. of App. Phys., **97**, 10H714 (2005).

VITA

Thomas Creel was born in Kansas City, Missouri. He received a Bachelors degree in Science (B.S.) in physics from Central Missouri State University in Warrensburg, Missouri. He received a Masters degree in Aerospace Engineering (M.S. A.S.E.) from the University of Texas at Austin in 1993 under the supervision of Professor Robert E. Schutz. He received a Masters degree (B.S.) in physics from the Missouri Science and Technology at Rolla Missouri. He enrolled as a graduate student in the Department of Physics at the Missouri University of Science and Technology (previously University of Missouri-Rolla) in August 2006 and carried out his doctoral research under the supervision of Professor William J. James, and Professor Oran A. Pringle. He received a Doctor of Philosophy (PhD) in physics from the Missouri University of Science and Technology in May 2013.